nature portfolio

Peer Review File

Hydroxyl chemistry regulation of cellulose biopolymers for aqueous zinc battery binders

Corresponding Author: Professor Zhaohui Wang

Parts of this Peer Review File have been redacted as indicated to remove third-party material.

This file contains all reviewer reports in order by version, followed by all author rebuttals in order by version.

Version 0:

Reviewer comments:

Reviewer #1

(Remarks to the Author)
In this manuscript, the authors present a strategy for cellulose biopolymer binders that are regulated by hydroxyl chemistry. Through selective ring-opening modification, they enhance the polymer's polarity, chain flexibility, and hydrogen bond network density, significantly improving its ability to anchor polyiodides and maintain electrode structural integrity in aqueous zinc-iodine batteries. The work demonstrates strong innovation with systematic experimental design, integrating multiple in situ/ex situ characterizations and theoretical calculations to showcase outstanding electrochemical performance and practical application potential. I think it can be considered after the following revisions for publication in Nature Communications.
1. The manuscript confirms the ring-opening of the AGU ring by FTIR and NMR but does not quantitatively evaluate the extent of ring-opening. It is recommended to establish a correlation between the degree of ring-opening and electrochemical performance.
2. The authors mention that GITT indicates that ONF enhances the diffusion coefficient of Zn2+. Please explain how improved diffusion of zinc ions on the iodine cathode side effects the redox reaction of iodine species.
3. The chemical stability of ONF in oxidizing polyiodide environments and during prolonged cycling has not been fully evaluated, nor has it been determined whether oxidation or chain scission occurs. Post-cycling ONF should undergo relevant characterization to verify its structural integrity.
4. It seems that the author has overlooked the influence of ONF's complex spatial conformation, which is analogous to that of cellulose chains, on iodine species and bonding properties. Please elaborate on how conformational changes in ONF, compared to CNF, affect the performance of iodine species and bonding.
5. The authors should clarify whether the empirical formulae used in the manuscript are applicable to the cellulose nanofiber system. It is recommended to supplement the study with variable-temperature FTIR or molecular dynamics simulations to validate hydrogen bond energies and distributions.
6. Does ONF simply absorb polyiodides, or does it actually catalyse their conversion? Conducting relevant experiments or theoretical calculations is recommended to evaluate the number of electron transfers in the reaction.
7. Does the hydroxyl group in ONF form a coordination bond with the zinc ion? How does the ONF-Zn complex interact with iodine species? Is there competition between zinc and polyiodide ions for the hydroxyl group in the chemical environment?
8. The current DFT calculations do not incorporate water molecules or an electrolyte environment. Please supplement the calculations to include the solution layer to more accurately reflect the adsorption energy.
9. Does the mechanical performance of ONF change with voltage variations as it undergoes adsorption and coordination with water molecules and various ions in actual batteries?
10. The surface capacity and volumetric energy density of the electrode require supplementation for comparison with other high-loading electrode systems.
11. The author's assertion that ONF's large capacitance gain is due to increased active site density is not substantiated. Relevant characterization data must be provided to support this assertion. Furthermore, the specific surface area and porosity parameters of the electrodes must be clarified when different binders are used.
12. Although the manuscript title emphasizes 'hydrogen bond chemistry', it fails to establish a structure-property relationship between hydrogen bonding and enhanced battery performance, such as iodine species conversion and vanadium species dissolution suppression. Further refinement of the manuscript 's logical flow is required.

Reviewer #2

(Remarks to the Author)
The use of naturally abundant biopolymers in sustainable battery technology is rising, as they offer chemical tunability to improve ion regulation and enhance electrochemical performance. This study serves as an excellent example by demonstrating that modifying the hydroxyl groups of cellulose provides an effective means to this end. The authors conclusively prove, through both theoretical and experimental evidence, that selectively cleaving the C2-C3 bonds of its glucose units transforms cellulose into a powerful functional binder. This binder exhibits strong affinity and compatibility with cathode active materials, enabling uniform electrode coverage and robust interactions with dissolution-prone species, which collectively promote stable/fast ion diffusion and redox kinetics. The effectiveness and broad applicability of this strategy are demonstrated across various cathode systems, including iodine, V_2O_5, and $LiMn_2O_4$ in aqueous batteries. Overall, this work significantly advances the fundamental understanding of cellulose hydroxyl chemistry, offering valuable insights for the rational design of bio-based binders in high-performance battery systems. Therefore, this interesting work is recommended for publication in Nature Communications after the following minor comments are addressed:

1. The density of hydrogen bonding network is enhanced after cellulose modification. Could this lead to more severe electrode swelling behavior? Authors are encouraged to provide more discussions on this point.
2. Error bars are missing from the cathode conductivity plot (Fig. 3g), revisions are suggested to address this.
3. Why does the CNF-based cathode exhibit larger polarization in the CV tests and higher high-frequency impedance in the DRT analysis compared to the PVDF-based electrode?
4. The degree of substitution or the percentage of C2-C3 bonds cleaved is important for establishing a clear structure-property relationship. This information should be provided.
5. The design procedure for the shuttle current measurement should be described in the experimental section.

Reviewer #3

(Remarks to the Author)
In this manuscript, Xu and Chen et al. designed a hydroxyl-chemistry regulation strategy for cellulose biopolymers to overcome the chemical and interfacial limitations of state-of-the-art binders in aqueous zinc batteries. Successfully, the Zn-I_2 battery fabricated with ONF binder achieves a high-rate capability of 150.9 mAh g^{-1} at 20 A g^{-1}, and exceptional capacity retention of 98.07% over 3000 h in a practical pouch cell. In general, this paper is very interesting. In my opinion, this paper can perhaps become publishable if following concerns can be well addressed.
1. a) On page 3, in paragraphs 38-39, the energy density is not only limited by the positive electrode, but also by the utilization rate of the negative electrode. b) Figure S24 and its related descriptions seem rather unclear. Where did the lost iodine go? This part of the content needs further revision. c) The statement "a fully encapsulated surface" is somewhat misleading. In fact, the ONF network itself is porous. d) It seems that the definite Zn^{2+} diffusion coefficients value has not been calculated in this article.
2. Whether any residual iodine sources (e.g., iodate or iodide ions) might remain in the ONF samples following the periodate-borohydride treatment of CNF? It would be valuable to briefly discuss the potential influence of such residues on the electrochemical properties.
3. In Figure 3d, more images of various resolutions are needed to illustrate the overall and detailed morphology. Was the cracks in Fig. 6a formed during the cyclic test, or did it appear before assembling battery? The SEM images of fresh PVDF electrode sheets need to be tested.
4. The cycling stability in Figure 4 is currently evaluated at high current densities. To provide a more comprehensive assessment of the battery's performance, we suggest including long-term cycling data at a lower current density, such as 0.2 A g^{-1}.
5. Self-discharge performance is one of the key performance indicators restricting the development of zinc-iodine batteries, and it is necessary to test the self-discharge performance of the battery during longer self-discharge cycles. BTW, in V_2O_5 batteries, does ONF bonding have the effect of suppressing self-discharge?
6. Why is it necessary to prepare high iodine loading electrodes through lamination? Can high loading self-supporting electrodes be prepared in one step? (10.1039 / D5EE01170A; 10.1016 / j.j cis. 2025.138936)?
7. To firmly establish the cycling stability advantage of the ONF electrode, providing the corresponding cycling data for the PVDF-based control electrode would be very helpful for direct comparison.
8. Please standardize the legend in Fig. 5a to clearly identify which sample each curve corresponds to, ensuring the graph's readability and data clarity.
9. To provide deeper mechanistic insight into the advantageous performance of the ONF electrode, we believe that including in situ Raman spectroscopy data for the CNF-based battery (for comparison with ONF) would be highly informative in revealing the structural evolution differences during operation.
10. The logic of the figure presentation in the main text should be reorganized for consistency. Currently, Fig. 5a-b primarily compare CNF and ONF electrodes, while Fig. 5c-g only compare PVDF and ONF. Furthermore, the PVDF control is absent in the long-term cycling figure. This inconsistency creates confusion for readers when interpreting the performance advantages. It is suggested to unify the baseline for comparison, for instance, including CNF, ONF, and PVDF data in all key performance figures (e.g., rate capability, cycling) or to provide a clear explanation in the text for the specific purpose of each comparison set.

Reviewer #4

(Remarks to the Author)

This manuscript, entitled “Hydroxyl Chemistry Regulation of Cellulose Biopolymers for Aqueous Battery Binders”, reports a hydroxyl-chemistry regulation strategy for cellulose biopolymers aimed at overcoming the chemical and interfacial limitations of current binder systems in aqueous zinc batteries. Specifically, the authors employ a periodate–borohydride selective disruption of the cyclic conformation of AGUs in the cellulose backbone to redistribute the electron cloud, enhance the dipole moment, and increase the reactivity of hydroxyl groups. This modification is proposed to unlock their capacity to regulate interfacial reactions and stabilise electrode architectures. As a result, the ONF binder, when applied in Zn–I_2 batteries, is reported to deliver a high-rate capability of 150.9 mAh g-1 at 20 A g-1 and an exceptional capacity retention of 98.07% over 3000 h in a practical pouch cell. Similarly, the incorporation of ONF into Zn–V2O5 batteries is claimed to significantly enhance electrochemical performance. However, despite these promising outcomes, the manuscript still exhibits substantial shortcomings in terms of scientific originality, data robustness, and mechanistic justification. It does not yet meet the publication standards of Nature Communications. My specific comments are as follows:
1. The authors apply the ONF binder to both Zn–I_2 and Zn–V_2O_5 battery systems. The failure mechanisms of these two cathodes are, however, fundamentally different. The authors are requested to clearly explain how the degradation pathways differ between the two systems.

2. The authors should provide a complete and detailed description of the calculation method used for the activation energy barriers shown in Figure 4c. It is currently unclear how these values were obtained.

3. The manuscript states: “Tafel slope analysis (Supplementary Fig. S18) further supported this conclusion…”. However, Supplementary Fig. S18 does not present Tafel plots but rather CV-derived rate data. The authors should correct this description and carefully check the entire manuscript for similar inconsistencies.

4. The interpretation of the GITT curves in Figure 4d is problematic. The data clearly correspond to a Zn–I_2 full cell, yet Zn^{2+} does not participate in the cathodic redox processes. The cathode involves only iodine species, and thus GITT cannot be used to infer Zn^{2+} diffusion. Moreover, iodine undergoes conversion reactions, and the associated kinetics are not governed by the diffusion properties of the binder. The authors should clarify what specific information the GITT analysis is intended to convey.

5. The binding energy calculations in Figure 5d inherently involve interactions between anionic species. In such systems, the basis functions of molecules A and B overlap within the AB complex, artificially lowering the computed E(AB). Have the authors applied Basis Set Superposition Error (BSSE) corrections in their calculations?

6. In Figure 5e, the Gibbs free-energy profiles for the CNF system are missing. The authors should clarify why CNF was not included in this comparison.

7. In the DRT analysis shown in Figure 5g, peaks P3 and P5 are attributed to Zn^{2+} transport resistance. Given the aqueous environment, why would Zn^{2+} transport dominate over H^+ movement? Furthermore, are these resistive features related to the conversion of polyiodide species? The authors should provide a more robust justification.

8. The manuscript lacks validation using ampere-hour–level pouch cells, which would be essential for demonstrating the practical applicability of the proposed binder system. The authors are encouraged to include large-format cell data.

9. A substantial body of literature has already reported the use of cellulose and cellulose derivatives as binders for aqueous zinc-ion batteries. Consequently, the novelty of the present work is questionable. Relevant examples include: Advanced Materials (2025, 37, 2412908), Nano Energy (2024, 120, 109094), and Nano Energy (2025, 133, 110519). The authors should clearly articulate how their approach differs from, and advances beyond, these prior reports.

Version 1:

Reviewer comments:

Reviewer #1

(Remarks to the Author)
Authors have well revised the manuscript that becomes acceptable now.

Reviewer #3

(Remarks to the Author)
The author has adequately addressed the reviewers' concerns. Recommend to publish this paper as current form.

Reviewer #4

(Remarks to the Author)
Happy with the revision, the paper can be accepted as it is.

Point-by-Point Response to Referees' Comments

(*Blue italic: Reviewer's remarks*; Black type: Our response)

Reviewer #1:

"In this manuscript, the authors present a strategy for cellulose biopolymer binders that are regulated by hydroxyl chemistry. Through selective ring-opening modification, they enhance the polymer's polarity, chain flexibility, and hydrogen bond network density, significantly improving its ability to anchor polyiodides and maintain electrode structural integrity in aqueous zinc-iodine batteries. The work demonstrates strong innovation with systematic experimental design, integrating multiple in situ/ex situ characterizations and theoretical calculations to showcase outstanding electrochemical performance and practical application potential. I think it can be considered after the following revisions for publication in Nature Communications."

Reply to the Reviewer:

We sincerely thank you for your careful review and valuable positive feedback. We have thoroughly considered and deliberated upon each of the highly insightful comments you provided, and we present our revisions and responses below.

Q1. *"The manuscript confirms the ring-opening of the AGU ring by FTIR and NMR but does not quantitatively evaluate the extent of ring-opening. It is recommended to establish a correlation between the degree of ring-opening and electrochemical performance."*

Reply to the Reviewer:

We sincerely thank you for this valuable suggestion, which has helped us to more systematically clarify the relationship between the degree of cellulose ring opening and electrochemical performance. In response, we have added a quantitative analysis in which the extracyclic hydroxyl content is used as an indicator of the AGU ring-opening degree. As sodium periodate ($NaIO_4$) selectively cleaves the C2-C3 bond of the anhydroglucose unit to generate aldehyde groups, followed by sodium borohydride ($NaBH_4$) reduction to form extracyclic hydroxyl groups, the resulting extracyclic hydroxyl content directly reflects the extent of ring opening.

By tuning the molar ratio of $NaIO_4$ to AGU, we prepared a series of cellulose samples with different degrees of ring opening. The extracyclic hydroxyl content, product yields, and corresponding electrochemical performance when used as binders for iodine cathodes were systematically evaluated. The corresponding results are presented in Supplementary Fig. 2 and Supplementary Table 1.

As the $NaIO_4$/AGU molar ratio increases, the extracyclic hydroxyl content gradually rises (Supplementary Fig. 2d), increasing from 1.7 mmol g^{-1} ($NaIO_4$/AGU=0.25) to 6.7 mmol g^{-1} ($NaIO_4$/AGU=4). Meanwhile, the yields of individual steps (periodate oxidation and borohydride reduction), as well as the overall yield, show a decreasing trend (Supplementary Fig. 2a-c), with the total yield dropping from 81.44% to 0.26%. Electrochemical testing reveals that the specific capacity of iodine cathodes initially increases significantly with increasing ring-opening degree (Supplementary Fig. 2e, f). For example, at a $NaIO_4$/AGU ratio of 1, the extracyclic hydroxyl content reaches approximately 4 mmol g^{-1}, and the specific capacity increases to 150.01 mAh g^{-1} (an

enhancement of ~18.3% compared with pristine cellulose), while the total yield remains relatively high (62.81%). However, further increasing the $NaIO_4$/AGU ratio to 2 results in a sharp reduction in total yield (42.14%), while the gain in specific capacity becomes marginal (~3.5%).

Revised:

(Page 5, lines 95-96)

We employed a periodate-borohydride treatment to open the cyclic conformation of the AGUs in pristine cellulose (CNF), producing an oxidized cellulose binder (ONF) with a disrupted ring structure under an optimized $NaIO_4$/AGU molar ratio of 1:1 (Supplementary Note 1, Supplementary Figs. 1, 2 and Supplementary Table 1).

(Supplementary Page 8)

Supplementary Note 1

As the $NaIO_4$/AGU molar ratio increases, the content of extracyclic hydroxyl (reflecting the degree of ring opening) rises gradually (Supplementary Fig. 2d, from 1.7 mmol g^{-1} at a ratio of 0.25 to 6.7 mmol g^{-1} at a ratio of 4). Concurrently, the yields from periodate oxidation, borohydride reduction, and the overall yield all exhibit a decreasing trend (Supplementary Fig. 2a-c; the total yield declines from 81.44% at a ratio of 0.25 to 0.26% at a ratio of 4).

The specific capacity of the iodine cathode increases with the initial rise in ring opening (Supplementary Fig. 2e, f). For instance, at a molar ratio of 1, the extracyclic hydroxyl content reaches 4 mmol g^{-1}, and the specific capacity rises to 150.01 mAh g^{-1} (an increase of approximately 18.3% compared with the unmodified sample), while the total yield remains relatively high at 62.81%. When the molar ratio is further increased to 2, the degree of ring opening continues to rise, but the total yield drops sharply to 42.14%, and the gain in specific capacity is only about 3.5%.

In summary, while increasing the ring-opening degree of cellulose can improve electrochemical performance, an excessively high degree of ring opening results in a dramatic reduction in yield. Therefore, a $NaIO_4$/AGU molar ratio of 1:1 was selected, as it achieves an optimal balance among ring-opening degree, yield, and electrochemical performance.

(Supplementary Page 9)

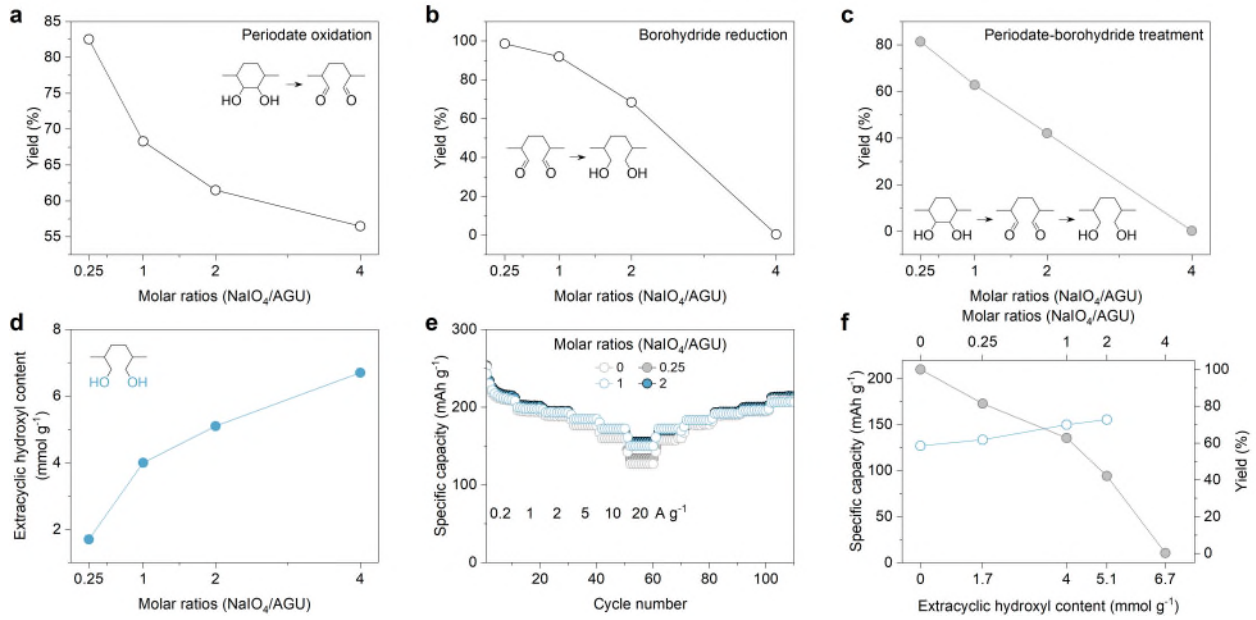

Supplementary Fig. 2. Synthesis parameters, properties, and corresponding cathode performance for ONF. **a-c,** Reaction yields at different $NaIO_4$/AGU molar ratios: **a,** periodate oxidation; **b,** borohydride reduction; **c,** total yield. **d,** Quantified content of extracyclic hydroxyl groups versus $NaIO_4$/AGU ratios. **e,** Rate performance of iodine cathodes prepared from ONFs with varying degrees of ring opening. **f,** Correlation between the degree of ring opening (extracyclic hydroxyl content) and the resulting specific capacity and total synthesis yield.

(**Supplementary Page 40**)

Supplementary Table 1. Synthesis parameters, key properties (yield, extracyclic hydroxyl content), and cathode performance (discharge capacity at 20 A g^{-1}) for ONFs prepared from CNF under varying conditions.

Molar ratios ($NaIO_4$/AGU)	Periodate oxidation yield	Borohydride reduction yield	Total yield	Extracyclic hydroxyl content (mmol g^{-1})	Specific capacity at 20 A g^{-1} (mAh g^{-1})
0	-	-	-	-	126.95
0.25	82.54%	98.66%	81.44%	1.7	133.64
1	68.31%	91.94%	62.81%	4	150.01
2	61.50%	68.51%	42.14%	5.1	155.20
4	56.48%	0.46%	0.26%	6.7	-

Q2. *"The authors mention that GITT indicates that ONF enhances the diffusion coefficient of Zn^{2+}. Please explain how improved diffusion of zinc ions on the iodine cathode side effects the redox reaction of iodine species."*

Reply to the Reviewer:

In zinc-iodine batteries, the cathodic redox process involves the reversible interconversion of iodine species (such as I_2, I^-, I_3^-), which proceeds through coupled electron transfer and ionic charge compensation. During discharge, I_2 reacts with I^- to form I_3^-, followed by further reduction to I^-, whereas the reverse reactions occur during charging to regenerate I_2. Although iodine species are

the redox-active components, efficient progression of these reactions requires timely Zn^{2+} migration from the electrolyte to maintain local electroneutrality and sustain interfacial charge balance. Importantly, Zn^{2+} ions are known to form charged complexes with polyiodide species (such as $[Zn{\cdot}I{\cdot}5H_2O]^+$, *Energy Environ. Sci.*, 2025, 18, 3160-3168; $[Zn{\cdot}I_3{\cdot}5H_2O]^+$, *Nat. Commun.*, 2015, 6, 6303), which directly couples Zn^{2+} transport to polyiodide migration and interfacial reaction kinetics. Consequently, sluggish Zn^{2+} diffusion on the cathode side leads to ion accumulation, concentration polarization, and delayed polyiodide conversion, thereby retarding iodine redox reactions.

Upon introduction of ONF, a continuous and highly hydrated hydrogen-bond network is established within the cathode, which markedly lowers Zn^{2+} transport resistance, as evidenced by the increased Zn^{2+} diffusion coefficients derived from GITT measurements. This enhanced Zn^{2+} mobility enables rapid replenishment of Zn^{2+} at the reaction interface, facilitating faster charge compensation during polyiodide redox reactions. As a result, electron-transfer processes associated with iodine species are accelerated, concentration polarization is suppressed, and the iodine conversion reactions proceed in a more uniform and continuous manner across the electrode.

Revised:
(Pages 11-12, lines 241-246)
Galvanostatic intermittent titration technique (GITT) measurements (Fig. 4d, Supplementary Fig. 26 and Supplementary Table 3) were used to evaluate the overall polarization behavior and apparent reaction kinetics of the iodine cathode. The reduced voltage relaxation and smaller polarization in the ONF-based system indicate faster redox equilibration and lower internal resistance, demonstrating that the ONF binder effectively mitigates concentration polarization and facilitates rapid iodine redox conversion [43-45].

Q3. *"The chemical stability of ONF in oxidizing polyiodide environments and during prolonged cycling has not been fully evaluated, nor has it been determined whether oxidation or chain scission occurs. Post-cycling ONF should undergo relevant characterization to verify its structural integrity."*

Reply to the Reviewer:
To address the concerns regarding the chemical and structural stability of ONF under the oxidizing polyiodide environment and prolonged electrochemical cycling, we performed post-cycling structural characterizations, including X-ray diffraction (XRD) and ATR-FTIR spectroscopy, on both CNF- and ONF-based cathodes before and after long-term cycling. The newly obtained results are provided in Supplementary Fig. 40.

The XRD patterns (Supplementary Fig. 40a, b) reveal that the cellulose crystalline framework of ONF remains intact after cycling, with no observable phase transformation or peak disappearance. In contrast, the CNF cathode exhibits a pronounced decrease in crystallinity after cycling, indicating disruption of the ordered cellulose domains. This is further supported by ATR-FTIR results (Supplementary Fig. 40c), which show a noticeable reduction in the characteristic absorption peak intensities for hydroxyl (-OH), alkyl (-CH), and glycosidic (C-O-C) bonds in CNF after cycling. This suggests that CNF underwent a certain degree of oxidative degradation and molecular chain scission, most likely due to the oxidative action of polyiodides.

By comparison, the ATR-FTIR spectra of ONF before and after cycling (Supplementary Fig. 40d) show negligible changes in peak position and intensity, demonstrating that the chemical functionalities and backbone structure of ONF are well preserved during electrochemical operation. These results confirm that ONF exhibits high resistance to oxidative attack, effectively suppressing molecular degradation and chain cleavage during prolonged cycling. Importantly, this enhanced chemical stability is consistent with the post-cycling morphological observations (Fig. 6c), where ONF-based cathodes maintain a continuous, intact nanofibrous encapsulation layer.

Revised:

(Page 16, lines 342-346)

In contrast, the cellulose-based electrodes retained overall electrode integrity with no visible fractures (Fig. 6b, c). However, the CNF-based cathode showed regions of exposed I_2@AC particles after cycling (Fig. 6b), while the ONF-based cathode (Fig. 6c) preserved high coverage surface with uniformly distributed nanofiber. Post-cycling XRD and ATR-FTIR analyses (Supplementary Note 5, Supplementary Fig. 40) further reveal that, unlike CNF which undergoes partial oxidative degradation and molecular chain cleavage [23,51], ONF remains chemically and structurally stable under prolonged cycling, confirming its resistance to electro-degradation even under dynamic electrochemical conditions, thus creating a polyiodide-shuttling-free barrier layer, which in turn protects the Zn anode.

(Supplementary Pages 26-27)

Supplementary Note 5

The XRD patterns (Supplementary Fig. 40a, b) show that the crystalline structure of both CNF and ONF remained unchanged before and after cycling, indicating that the fundamental cellulose framework was preserved. However, a significant decrease in crystallinity was observed for CNF after cycling. This is further supported by ATR-FTIR results (Supplementary Fig. 40c), which show a noticeable reduction in the characteristic absorption peak intensities for hydroxyl (-OH), alkyl (-CH), and glycosidic (C-O-C) bonds in CNF after cycling. This suggests that CNF underwent a certain degree of oxidative degradation and molecular chain scission due to the oxidative action of polyiodides and the mechanical stresses experienced during cycling. In sharp contrast, both the crystallinity and the intensities of the aforementioned characteristic functional group absorption peaks in ONF remained virtually unchanged after cycling (Supplementary Fig. 40d). This demonstrates that ONF possesses superior chemical stability against the oxidative environment in zinc-iodine batteries and maintains its structural integrity throughout long-term cycling. This enhanced stability is also the reason why ONF retains a more complete morphology after cycling, as shown in Fig. 6c.

(Supplementary Page 27)

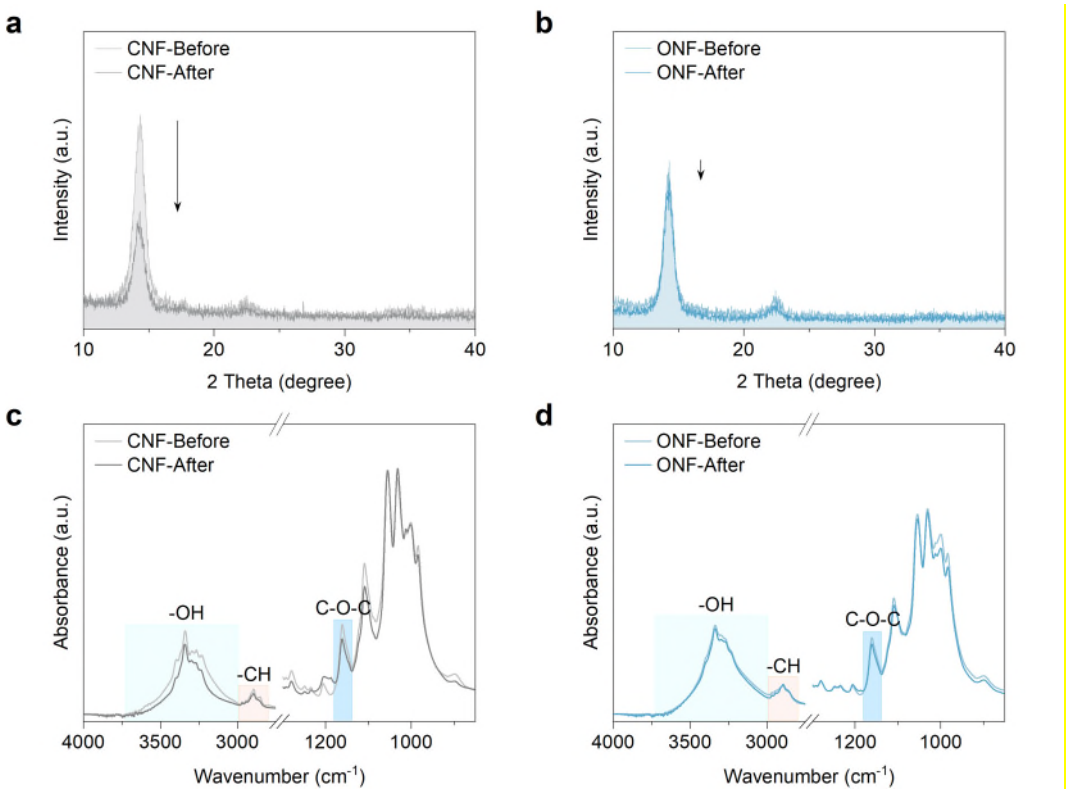

Supplementary Fig. 40. Characterization of Cycling Stability for CNF and ONF. **a, b,** XRD patterns. **c, d,** ATR-FTIR spectra.

Q4. *"It seems that the author has overlooked the influence of ONF's complex spatial conformation, which is analogous to that of cellulose chains, on iodine species and bonding properties. Please elaborate on how conformational changes in ONF, compared to CNF, affect the performance of iodine species and bonding."*

Reply to the Reviewer:

We thank you for this insightful comment and fully agree that the spatial conformation of cellulose chains can govern iodine accommodation and bonding behavior.

Beyond increasing hydroxyl density, C2-C3 bond cleavage induces a cooperative reorganization of cellulose chain conformation, characterized by enhanced chain flexibility, redistributed hydrogen-bonding motifs, and modified surface electrostatic potential. This conclusion is supported by combined spectroscopic, electrostatic, and simulation analyses (Fig. 2). Importantly, this conformational reorganization directly governs how iodine species are accommodated, bound, and converted at the cathode interface, as elucidated by electrochemical, spectroscopic, and theoretical results in Fig. 5.

To strengthen this structure-property connection, we further performed conformational analysis of CNF and ONF chains with identical degrees of polymerization, as shown in Supplementary Fig. 7. While both materials retain a helical backbone, ONF adopts a more compact and conformationally ordered helix, with hydroxyl groups preferentially oriented toward the exterior surface. This reorganization enhances spatial cooperativity among hydroxyl groups and enables the formation of

a dense, continuous hydrogen-bonding network, thereby strengthening both physical confinement and chemical interaction with polyiodides (*Nat. Commun.*, 2025, 16, 9301).

Revised:

(Pages 7-8, lines 139-143)

Moreover, C2-C3 bond cleavage induces a cooperative reorganization of the cellulose chain conformation, giving rise to a more compact helical structure with preferential outward orientation of hydroxyl groups and enhanced spatial cooperativity (Supplementary Fig. 7) [17]. This conformational reorganization is expected to facilitate more effective physical confinement and chemical interaction with polyiodide species (Supplementary Note 2) [34,35].

(Supplementary Page 11)

Supplementary Note 2

A CNF chain composed of 24 anhydroglucose units (AGUs) adopts a loosely packed helical conformation (Supplementary Fig. 7), characterized by an inner diameter (d_1) of ~9.5 Å, an outer diameter (d_2) of ~28.5 Å, and a helical pitch (d_3) of ~12 Å. In this configuration, hydroxyl groups are randomly distributed on both the inner and outer surfaces of the helix, leading to spatially dispersed interaction sites and inefficient cooperative binding toward iodine species. In contrast, ONF—constructed from the same number of AGUs but subjected to targeted ring opening—exhibits a conformationally optimized helical structure. Specifically, ONF shows a significantly reduced inner diameter ($d_1 \approx 4$ Å) and outer diameter ($d_2 \approx 20$ Å), along with an expanded pitch ($d_3 \approx 25.5$ Å). Importantly, the hydroxyl groups in ONF are preferentially oriented toward the outer surface of the helix, rather than being randomly distributed. This conformational reorganization endows ONF with a compact, size-matched nanocavity that accommodates linear I_3^- species (~2.2 Å), while the outward-oriented hydroxyl groups and extended helical pitch create a dense, cooperative hydrogen-bonding network capable of strong I···H-O interactions. Importantly, despite partial hydrogen-bond consumption during polyiodide adsorption, ONF retains a substantially higher fraction of intermolecular hydrogen bonding than CNF, enabling simultaneous iodine immobilization and preservation of structural integrity during prolonged cycling.

(Supplementary Page 12)

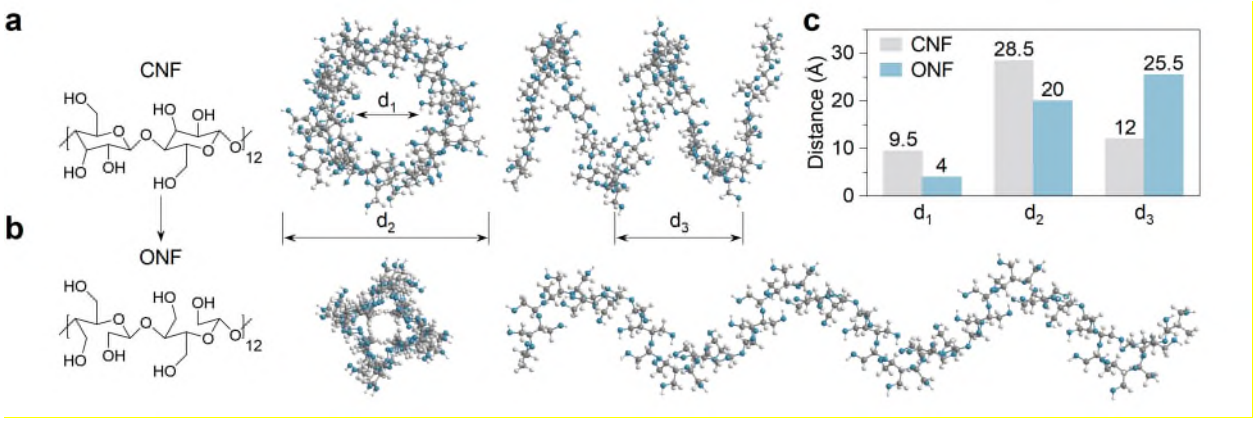

Supplementary Fig. 7. a, CNF and **b,** ONF cellulose conformations with corresponding **c,** structural parameters.

Q5. *"The authors should clarify whether the empirical formulae used in the manuscript are applicable to the cellulose nanofiber system. It is recommended to supplement the study with variable-temperature FTIR or molecular dynamics simulations to validate hydrogen bond energies and distributions."*

Reply to the Reviewer:

Thank you for this valuable suggestion. The intermolecular hydrogen bonding energies (E_H, kJ) were estimated quantitatively with Equation (R1)

$$E_H = \frac{1}{k} \times \frac{\nu_0 - \nu}{\nu_0} \quad \text{(R1)}$$

where ν_0 is the standard frequency of free OH groups (3600 cm^{-1}), ν is the frequency of bound -OH groups (cm^{-1}), and k is a constant (k^{-1}=262.5 kJ).

This model directly correlates hydrogen-bond strength with experimentally measurable FTIR parameters and has been successfully applied to cellulose nanofiber systems, including cellulose elementary fibrils used as battery binders (*Nano-Micro Lett.*, 2025, 17, 112). In our study, solid-state NMR spectra (Fig. 2b) and grazing-incidence XRD patterns (Fig. 2c) confirm that its structure of CNF is consistent with standard cellulose. Therefore, the empirical formula is applicable for calculating the interchain hydrogen bond strength of CNF.

ONF is obtained via controlled modification of CNF without altering the cellulose crystalline framework. XRD analysis shows that the crystalline structure of ONF remains unchanged relative to CNF, and ATR-FTIR spectra (Fig. 2a) display O-H stretching bands in the same 3000-3500 cm^{-1}, with comparable peak shapes. These observations indicate that the chemical nature of hydroxyl groups remains unchanged, justifying the use of the same empirical model for ONF. Importantly, the calculated hydrogen-bond energies for CNF (28.51 kJ mol^{-1}) and ONF (29.24 kJ mol^{-1}) fall well within the accepted range of hydrogen-bond strengths (4-120 kJ mol^{-1}, *Nat. Rev. Mater.*, 2025, 10, 728-749). Hence, we consider the adopted empirical formula suitable for estimating the interchain hydrogen bond strength in our cellulose system.

Following your suggestion, we have performed molecular dynamics (MD) simulations to directly evaluate hydrogen-bond number, distribution, and thermal stability. The results are presented in newly added Supplementary Fig. 5. At 25 ℃, ONF forms 229 intermolecular hydrogen bonds, significantly higher than CNF (166). Upon increasing the temperature to 40 ℃, ONF maintains 220 hydrogen bonds, whereas CNF decreases further to 150 (Supplementary Fig. 5c). Moreover, hydrogen-bond distance distributions (Supplementary Fig. 5d) show a unimodal profile centered at 0.30-0.33 nm for both systems; however, CNF exhibits a pronounced shift toward longer bond distances with increasing temperature, while ONF retains an essentially unchanged distribution. This demonstrates that ONF forms a denser and more thermally robust hydrogen-bond network.

Together, the empirical FTIR-based analysis and independent MD simulations consistently demonstrate that ONF possesses a stronger, denser, and more thermally stable intermolecular hydrogen-bonding network than CNF.

Revised:

(Page 6, lines 122-124)

Moreover, the -OH signal in ONF shifted to lower wavenumbers. Deconvolution analysis (Supplementary Fig. S4) revealed an increase in intermolecular hydrogen bonding (from 52.28% in CNF to 57.16% in ONF) and enlarged hydrogen bond energy (from 28.51 to 29.24 kJ mol^{-1}). Molecular dynamics simulations (Supplementary Fig. 5) further confirm that ONF forms a greater number of intermolecular hydrogen bonds and exhibits enhanced resistance to perturbation [31-33], evidencing a more robust hydrogen-bonding network.

(Page 24, lines 530-539)

All molecular dynamics simulations were performed using the GROMACS 2025.2 software package. All molecules were subjected to GAFF force fields. The initial configurations of the systems were constructed using the PACKMOL software package. The simulation boxes were cubic periodic cells with a side length of 5.0 nm. The simulation pipeline began with an energy minimization step to relax the initial structure. Subsequently, the system was run for 500 ps in an NVT (isothermal and isochoric) ensemble to reach temperature equilibrium, with a time step of 1.0 fs. The temperature was controlled by a Nosé-Hoover thermostat. A subsequent 5 ns NPT simulation with a step size of 1 fs was performed to bring the system pressure to equilibrium at 1 bar. After equilibrium was reached, a 10.0 ns production run was performed with a time step of 1.0 fs. Trajectories were saved every 1000 steps for subsequent analysis.

(Supplementary Page 10)

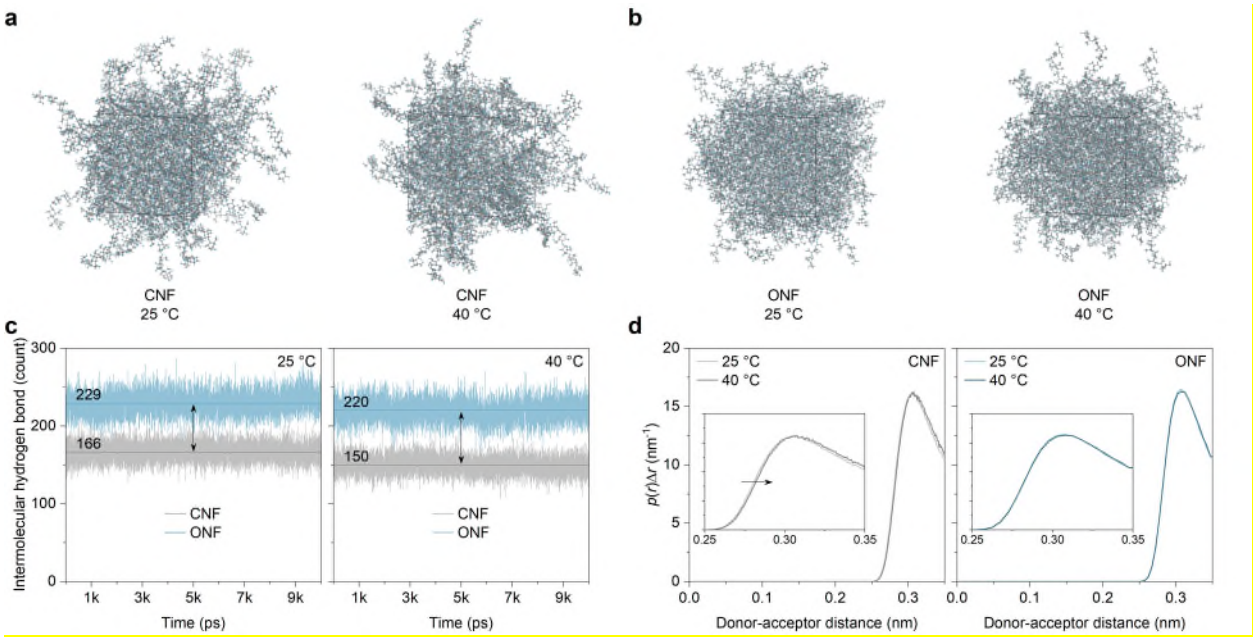

Supplementary Fig. 5. Molecular dynamics simulation of cellulose hydrogen bond energy changes at 25 °C and 40 °C. **a,** CNF cluster model. **b,** ONF cluster model. **c,** Variation in the number of intermolecular hydrogen bonds. **d,** Variation in the length of intermolecular hydrogen bonds.

Q6. *"Does ONF simply absorb polyiodides, or does it actually catalyse their conversion? Conducting relevant experiments or theoretical calculations is recommended to evaluate the number of electron transfers in the reaction."*

Reply to the Reviewer:

Thank you for your highly valuable comment, which precisely identifies the key to elucidating the mechanism of ONF (whether it functions via adsorption or catalysis). Based on combined electrochemical, spectroscopic, and theoretical evidence, we demonstrate that ONF not only immobilizes polyiodides through strong adsorption but also actively promotes their electrochemical conversion, fulfilling a catalytic role in the iodine redox process. First, the visual adsorption experiments (Fig. 5a, b) and corresponding DFT calculations (Fig. 5g) demonstrate that ONF exhibits effective adsorption toward polyiodides. Second, variable scan rate CV curves (Fig. 4a and Supplementary Fig. 23) show that only a single dominant peak appears during the oxidation/reduction processes for cathodes using PVDF, CNF, or ONF as binders. This indicates that the reversible conversion between I_2 and I^-, involving a two-electron transfer, occurs in all three binder systems. Furthermore, the reaction energy barrier diagrams (Fig. 4c) reveal that the redox reaction barrier between I_2 and I^- is significantly reduced in the ONF system compared to the PVDF and CNF systems. Gibbs free energy calculations (Fig. 5h) also show that the tendency for I_2 conversion to I^- is enhanced (-3.08 eV) in the presence of ONF. Finally, in situ UV vis spectroscopy (Fig. 5c-e) and in situ Raman spectroscopy (Fig. 5f) provide direct evidence that the concentration of polyiodides (I_3^- and I_5^-) remains consistently low during the reaction in the ONF system. This indicates that ONF accelerates the redox reaction between I_2 and I^-, serving as a key criterion for its catalytic role.

Revised:

(Page 11, line 227)

The cyclic voltammetry (CV) profiles (Fig. 4a and Supplementary Fig. 23) revealed the characteristic redox peaks corresponding to the reversible two-electron conversion reaction ($I_2 \leftrightarrow 2I^-$) [40].

(Page 11, lines 239-240)

These reductions confirm that ONF catalytically promotes iodine conversion, rather than simply enabling physical adsorption.

(Page 14, lines 304-306)

In contrast, cellulose-based cathodes exhibited low I_3^-/I_5^- signal intensities across the entire potential window. Notably, such signals were nearly undetectable for the ONF-based cathode, demonstrating more effective immobilization and accelerated catalytic conversion of iodine intermediates.

Q7. *"Does the hydroxyl group in ONF form a coordination bond with the zinc ion? How does the ONF-Zn complex interact with iodine species? Is there competition between zinc and polyiodide ions for the hydroxyl group in the chemical environment?"*

Reply to the Reviewer:

Yes, the hydroxyl groups in ONF can coordinate with Zn^{2+}. In aqueous electrolytes, Zn^{2+} primarily exists as a hexaaqua complex, $[Zn(H_2O)_6]^{2+}$ (Fig. R1a), which is an electron deficient cation. Therefore, the two can form coordination bonds through Lewis acid-base interactions. Second, the interaction between the ONF-Zn complex and iodine species is site-specific. Polyiodides are anions and tend to interact with the electropositive hydrogen atoms of hydroxyl groups via hydrogen bonding. DFT calculation results (Fig. R1b, c) show that the binding energies of $[Zn(H_2O)_6]^{2+}$ toward I_3^- (-2.76 eV) and I_5^- (-2.09 eV) are significantly higher than those of ONF alone (-0.45 eV and -0.36 eV). This indicates that after ONF coordinates with Zn^{2+}, the positive charge of Zn^{2+} enhances the electropositivity of the hydroxyl hydrogen atoms, thereby strengthening the binding capability toward polyiodides.

We do not expect strong direct competition because Zn^{2+} primarily interacts with the hydroxyl oxygen (coordination), whereas polyiodides interact mainly with electropositive sites via hydrogen bonding/electrostatic interactions. Thus, these interactions can coexist. Importantly, the central focus of our current study is the regulation of polyiodide generation/shuttling and iodine redox kinetics through hydroxyl-chemistry engineering of the binder, rather than detailed Zn^{2+} coordination chemistry. The Zn^{2+}-hydroxyl interaction is therefore discussed here only as a plausible secondary interaction at the interface. A systematic quantification of ONF-Zn^{2+} coordination (and its coupled effect on iodine speciation) would require dedicated operando coordination/spectroscopic studies and/or extended simulations, which we consider highly interesting and plan to pursue in a separate, future study.

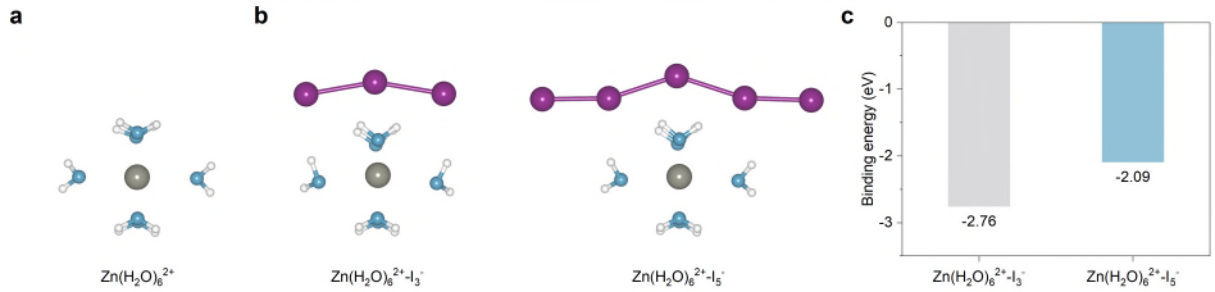

Fig. R1. a, Form of Zn^{2+} in aqueous environments. **b,** Interaction between $[Zn(H_2O)_6]^{2+}$ and polyiodides and corresponding **c,** binding energy.

Q8. *"The current DFT calculations do not incorporate water molecules or an electrolyte environment. Please supplement the calculations to include the solution layer to more accurately reflect the adsorption energy."*

Reply to the Reviewer:

Thank you for this important comment regarding the role of the solvation environment in adsorption energy calculations. In the present system, however, explicit solvent-layer modeling for polyiodide adsorption presents fundamental challenges. Unlike Zn^{2+}, which has a small ionic radius and highly localized charge and therefore forms a well-defined and relatively stable hydration shell, polyiodide species are large, flexible, and exhibit significant charge delocalization along the iodine chain. Their interaction with water molecules occurs mainly through weak and transient hydrogen bonding, resulting in a highly dynamic solvation environment without a fixed coordination number or stable geometry. Consequently, defining a representative explicit solvation shell for polyiodides would require extensive configurational sampling and introduce substantial uncertainty into adsorption energy calculations, potentially compromising reproducibility and interpretability.

For this reason, adsorption energies of polyiodides in zinc-iodine battery studies are commonly evaluated using vacuum DFT calculations, focusing on relative binding trends rather than absolute values. This approach has been widely adopted in recent high-impact literature (e.g., *J. Am. Chem. Soc.*, 2025, 147(1), 669-677; *J. Am. Chem. Soc.*, 2024, 146(10), 6628-6637; *Adv. Mater.*, 2024, 36, 2403097; *Energy Environ. Sci.*, 2025,18, 4800-4810), particularly when the goal is to compare interfacial affinity across different materials. Importantly, the relative adsorption trends obtained from our DFT calculations are fully consistent with experimental observations, including UV-vis adsorption tests, XPS analysis, in situ spectroscopy, and electrochemical performance. These combined results reliably demonstrate the enhanced affinity of the engineered cellulose binder toward polyiodides and its role in suppressing shuttling and accelerating iodine redox kinetics.

We therefore consider the current DFT framework appropriate for elucidating the interaction mechanism and comparative binding behavior. Nevertheless, we fully acknowledge that more advanced solvation models-such as ab initio molecular dynamics or enhanced sampling methods—could provide further insight into dynamic solvent effects. Such investigations are highly interesting but fall beyond the scope of the present study and will be pursued in future work as solvation modeling strategies for polyiodide systems continue to develop.

Q9. *"Does the mechanical performance of ONF change with voltage variations as it undergoes adsorption and coordination with water molecules and various ions in actual batteries?"*

Reply to the Reviewer:

Thank you for this insightful question regarding the mechanical stability of ONF under realistic battery operating conditions. To address this point, we performed wet-state mechanical testing and post-cycling structural analyses, with the results presented in Supplementary Fig. 20 and Supplementary Fig. 38, respectively.

First, to decouple the effects of water molecules and electrolyte ions, iodine cathodes were immersed in either deionized water or 2 M $ZnSO_4$ electrolyte, allowing cellulose binders to interact predominantly with water molecules or with hydrated ions. Tensile tests conducted under these wet

conditions show that ONF consistently exhibits higher tensile strength and elongation than CNF in both environments, in agreement with their dry-state mechanical behavior (Fig. 2h).

When coordinated solely with water molecules, cellulose cathodes show increased elongation but reduced tensile strength. This behavior arises from partial disruption of interchain hydrogen bonds by water, which lowers resistance to interchain sliding. Importantly, this softening effect is significantly mitigated in the presence of electrolyte ions. In $ZnSO_4$ solution, metal ions reduce free-water activity and can coordinate with hydroxyl groups on cellulose chains, reinforcing interchain interactions and increasing resistance to sliding—an effect consistent with prior reports on ion-mediated reinforcement of cellulose networks (*Adv. Funct. Mater*., 2023, 33, 2304280; *Nature*, 2021, 598, 590-596). More critically, post-cycling electrodes recovered from fully assembled Zn-iodine cells retain structural integrity when ONF is used as the binder (Supplementary Fig. 38). These results demonstrate that ONF maintains sufficient mechanical robustness under electrochemical cycling, even as it dynamically interacts with water molecules, ions, and iodine species.

Revised:

(Pages 10-11, lines 214-217)

Enhanced wet-state mechanical robustness (Supplementary Fig. 20) together with suppressed thickness variation after electrolyte soaking (Supplementary Fig. 21) indicates that the densified and cohesive ONF binder network enables mechanical integrity even in aqueous electrolyte environment [38,39].

(Page 16, line 339)

After prolonged cycling, the PVDF-based cathode exhibited severe structural degradation, including extensive cracking across both the electrode matrix and individual I_2@AC particles (Fig. 6a and Supplementary Figs. 38, 39).

(Supplementary Page 17)

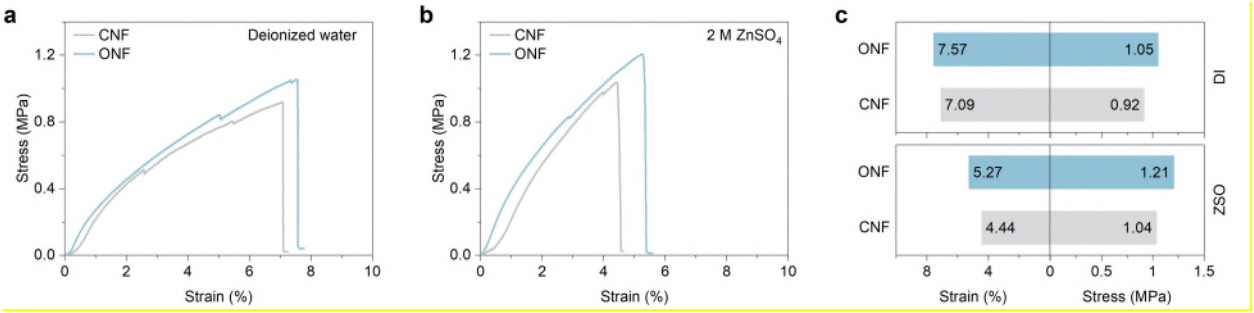

Supplementary Fig. 20. Wet-state mechanical properties of CNF and ONF cathodes. **a,** Stress-strain curves of cathodes immersed in deionized water. **b,** Stress-strain curves of cathodes immersed in 2 M $ZnSO_4$ solution. **c,** Tensile strength and elongation of cathodes after immersion in different liquids.

(Supplementary Page 26)

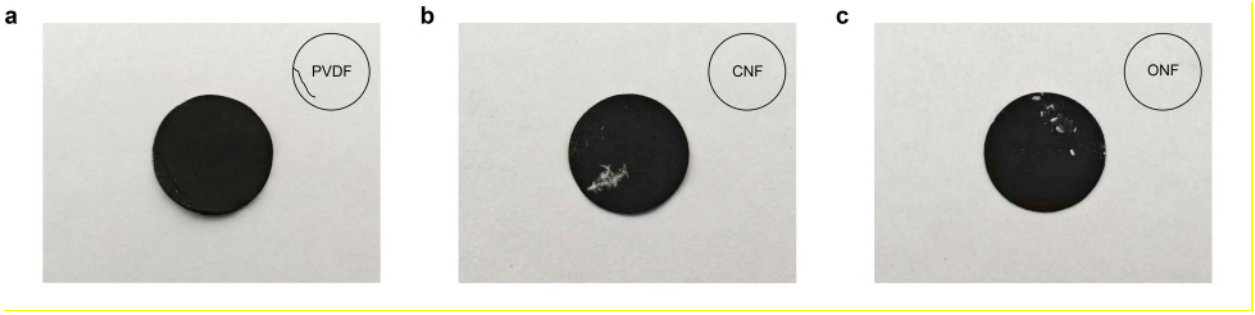

Supplementary Fig. 38. Optical photographs of iodine cathodes disassembled after battery cycling. **a,** PVDF-based. **b,** CNF-based. **c,** ONF-based.

Q10. *"The surface capacity and volumetric energy density of the electrode require supplementation for comparison with other high-loading electrode systems."*

Reply to the Reviewer:

We have updated the performance comparison table to explicitly include areal iodine loading and areal capacity for both our work and representative iodine cathodes reported in the literature (Supplementary Table 4). This enables a direct and meaningful comparison of surface-level performance across different electrode designs. With respect to volumetric energy density, we note that most previously reported zinc-iodine studies do not disclose the full electrode thickness or packing density required for reliable volumetric calculations. To avoid speculative estimations, we therefore provide experimentally determined volumetric energy density values for our electrodes, calculated using the measured electrode thickness and mass loading. These values demonstrate that our ONF-based cathodes deliver competitive volumetric performance alongside high areal capacity.

Revised:

(Page 12, line 269)

The synergistically achieved high-rate capacity (150.9 mAh g^{-1} at 20 A g^{-1}) and exceptional longevity (10,000 cycles at 10 A g^{-1} with minimal degradation) are rarely achieved (Fig. 4j, Supplementary Fig. 32, and Supplementary Table 4), either independently or concurrently in Zn-iodine batteries, including those employing advanced iodine hosts, electrolyte modifications, ion-selective separators, or functional binder chemistries.

(Supplementary Page 41)

Supplementary Table 4. Comparative of electrochemical performance in aqueous Zn-I_2 battery.

Samples		Iodine loading	Rate performance	Cycling stability
Binder	Ref. 1	1-2 mg cm^{-2}	179.8 mAh g^{-1} (0.2697 mAh cm^{-2}) at 0.2 A g^{-1} 123.2 mAh g^{-1} (0.1848 mAh cm^{-2}) at 2 A g^{-1}	142.5 mAh g^{-1} (0.2138 mAh cm^{-2}) at 0.2 A g^{-1} after 1500 cycles

	Ref. 2	2.69 mg cm^{-2}	213.8 mAh g^{-1} (0.5751 mAh cm^{-2}) at 0.2 A g^{-1} 83.0 mAh g^{-1} (0.2233 mAh cm^{-2}) at 5 A g^{-1}	129.4 mAh g^{-1} (0.3750 mAh cm^{-2}) at 2 A g^{-1} after 2700 cycles
	Ref. 3	4.7 mg cm^{-2}	207.2 mAh g^{-1} (0.9738 mAh cm^{-2}) at 0.2 A g^{-1} 156.6 mAh g^{-1} (0.7360 mAh cm^{-2}) at 3 A g^{-1}	151.1 mAh g^{-1} (0.7102 mAh cm^{-2}) at 3 A g^{-1} after 9000 cycles
	Ref. 4	2.3 mg cm^{-2}	219.0 mAh g^{-1} (0.5037 mAh cm^{-2}) at 0.1 A g^{-1} 141.5 mAh g^{-1} (0.3254 mAh cm^{-2}) at 2 A g^{-1}	157.7 mAh g^{-1} (0.3627 mAh cm^{-2}) at 2 A g^{-1} after 48000 cycles
	Ref.5	-	185.5 mAh g^{-1} at 0.1 A g^{-1} 121.8 mAh g^{-1} at 2 A g^{-1}	88.2 mAh g^{-1} at 4 A g^{-1} after 15000 cycles
Iodine host	Ref. 6	3 mg cm^{-2}	176.5 mAh g^{-1} (0.5295 mAh cm^{-2}) at 0.2 A g^{-1} 66.3 mAh g^{-1} (0.1989 mAh cm^{-2}) at 10 A g^{-1}	88.2 mAh g^{-1} (0.0246 mAh cm^{-2}) at 10 A g^{-1} after 10000 cycles
	Ref. 7	1.7 mg cm^{-2}	164.8 mAh g^{-1} (0.2802 mAh cm^{-2}) at 0.1 A g^{-1} 72.3 mAh g^{-1} (0.1229 mAh cm^{-2}) at 1 A g^{-1}	116.6 mAh g^{-1} (0.1982 mAh cm^{-2}) at 0.8 A g^{-1} after 1000 cycles
	Ref. 8	0.8-1.2 mg cm^{-2}	195.1 mAh g^{-1} (0.1951 mAh cm^{-2}) at 0.1 A g^{-1} 93.5 mAh g^{-1} (0.0935 mAh cm^{-2}) at 10 A g^{-1}	113.1 mAh g^{-1} (0.1131 mAh cm^{-2}) at 1 A g^{-1} after 1000 cycles
	Ref. 9	2-2.5 mg cm^{-2}	255.4 mAh g^{-1} (0.5746 mAh cm^{-2}) at 0.1 A g^{-1} 152.3 mAh g^{-1} (0.3427 mAh cm^{-2}) at 3 A g^{-1}	124.0 mAh g^{-1} (0.2790 mAh cm^{-2}) at 3 A g^{-1} after 5900 cycles
	Ref. 10	2 mg cm^{-2}	212 mAh g^{-1} (0.4240 mAh cm^{-2}) at 0.2 A g^{-1} 92 mAh g^{-1} (0.184 mAh cm^{-2}) at 8 A g^{-1}	111.9 mAh g^{-1} (0.2238 mAh cm^{-2}) at 5 A g^{-1} after 5000 cycles

	Ref. 11	0.8-1.2 mg cm^{-2}	241.5 mAh g^{-1} (0.2415 mAh cm^{-2}) at 0.2 A g^{-1} 161.8 mAh g^{-1} (0.1618 mAh cm^{-2}) at 2 A g^{-1}	92.6 mAh g^{-1} (0.0926 mAh cm^{-2}) at 5 A g^{-1} after 20000 cycles
	Ref. 12	3.3 mg cm^{-2}	162.4 mAh g^{-1} (0.5359 mAh cm^{-2}) at 0.2 A g^{-1} 100.8 mAh g^{-1} (0.3326 mAh cm^{-2}) at 2 A g^{-1}	83.6 mAh g^{-1} (0.0119 mAh cm^{-2}) at 2 A g^{-1} after 1000 cycles
Separator	Ref. 13	2 mg cm^{-2}	236.7 mAh g^{-1} (0.4734 mAh cm^{-2}) at 0.2 A g^{-1} 144.9 mAh g^{-1} (0.2898 mAh cm^{-2}) at 5 A g^{-1}	158.3 mAh g^{-1} (0.3166 mAh cm^{-2}) at 2 A g^{-1} after 20000 cycles
	Ref. 14	1.5 mg cm^{-2}	208 mAh g^{-1} (0.3120 mAh cm^{-2}) at 0.1 A g^{-1} 114 mAh g^{-1} (0.1710 mAh cm^{-2}) at 2 A g^{-1}	146.1 mAh g^{-1} (0.2374 mAh cm^{-2}) at 0.2 A g^{-1} after 3600 cycles
	Ref. 15	-	176.8 mAh g^{-1} (0.1 A g^{-1}) 151.6 m mAh g^{-1} (2 A g^{-1})	166.7 mAh g^{-1} at 2 A g^{-1} after 15000 cycles
	Ref. 16	1 mg cm^{-2}	212.3 mAh g^{-1} (0.2123 mAh cm^{-2}) at 0.2 A g^{-1} 192.3 mAh g^{-1} (0.1923 mAh cm^{-2}) at 4 A g^{-1}	185.2 mAh g^{-1} (0.1852 mAh cm^{-2}) at 1 A g^{-1} after 2000 cycles
Electrolyte	Ref. 17	5 mg cm^{-2}	134.4 mAh g^{-1} (0.6720 mAh cm^{-2}) at 0.5 A g^{-1} 79.2 mAh g^{-1} (0.3960 mAh cm^{-2}) at 10 A g^{-1}	99.6 mAh g^{-1} (0.4980 mAh cm^{-2}) at 2 A g^{-1} after 50000 cycles
	Ref. 18	0.8-1.0 mg cm^{-2}	138.4 mAh g^{-1} (0.1246 mAh cm^{-2}) at 0.5 A g^{-1} 81.6 mAh g^{-1} (0.0734 mAh cm^{-2}) at 10 A g^{-1}	98.1 mAh g^{-1} (0.0882 mAh cm^{-2}) at 1 A g^{-1} after 8000 cycles
Zinc anode	Ref. 19	5.4 mg cm^{-2}	168.8 mAh g^{-1} (0.9115 mAh cm^{-2}) at 0.1 A g^{-1} 118.8 mAh g^{-1} (0.6415 mAh cm^{-2}) at 6 A g^{-1}	105.8 mAh g^{-1} (0.5713 mAh cm^{-2}) at 2 A g^{-1} after 65000 cycles

	Ref. 20	6 mg cm^{-2}	214.0 mAh g^{-1} (1.2840 mAh cm^{-2}) at 0.1 A g^{-1} 130.6 mAh g^{-1} (0.7836 mAh cm^{-2}) at 2 A g^{-1}	124.0 mAh g^{-1} (0.7440 mAh cm^{-2}) at 1 A g^{-1} after 2400 cycles
	Ref. 21	1.3 mg cm^{-2}	169.3 mAh g^{-1} (0.2201 mAh cm^{-2}) at 0.2 A g^{-1} 98.8 mAh g^{-1} (0.1284 mAh cm^{-2}) at 5 A g^{-1}	97.0 mAh g^{-1} (0.1261 mAh cm^{-2}) at 2 A g^{-1} after 20000 cycles
	Ref. 22	1-1.5 mg cm^{-2}	174.0 mAh g^{-1} (0.2175 mAh cm^{-2}) at 0.2 A g^{-1} 125.0 mAh g^{-1} (0.1562 mAh cm^{-2}) at 10 A g^{-1}	124.2 mAh g^{-1} (0.1552 mAh cm^{-2}) at 5 A g^{-1} after 60000 cycles
	Ref. 23	-	195.9 mAh g^{-1} (0.1 A g^{-1}) 124.5 mAh g^{-1} (5 A g^{-1})	141.8 mAh g^{-1} at 2 A g^{-1} after 5600 cycles
This work	ONF binder	4 mg cm^{-2}	212.7 mAh g^{-1} (0.8508 mAh cm^{-2}, 2.5611 mWh cm^{-3}) at 0.2 A g^{-1} 173.1 mAh g^{-1} (0.6924 mAh cm^{-2}, 1.9888 mWh cm^{-3}) at 10 A g^{-1} 150.9 mAh g^{-1} (0.6036 mAh cm^{-2}, 1.6121 mWh cm^{-3}) at 20 A g^{-1}	163.9 mAh g^{-1} (0.6556 mAh cm^{-2}, 1.5528 mWh cm^{-3}) at 10A g^{-1} after 10000 cycles

Note: Areal capacity (mAh cm^{-2}) = Specific capacity (mAh g^{-1}) × Iodine loading (g cm^{-2}), Volumetric energy density (mWh cm^{-3}) = (Areal capacity (mAh cm^{-2}) × Average voltage (V)) / Cathode thickness (cm).

1 Yang, J.-L. *et al.* Janus binder chemistry for synchronous enhancement of iodine species adsorption and redox kinetics toward sustainable aqueous Zn-I_2 batteries. *J. Am. Chem. Soc.* **146**, 6628-6637 (2024).

2 Wang, K. *et al.* An iodine-chemisorption binder for high-loading and shuttle-free Zn-iodine batteries. *Adv. Energy Mater.* **14**, 2304110 (2024).

3 Li, Z. *et al.* Deploying cationic cellulose nanofiber confinement to enable high iodine loadings towards high energy and high-temperature Zn-I_2 battery. *Angew. Chem., Int. Ed.* **63**, e202317652 (2023).

4 Yu, Z.-T. *et al.* Gelatinized starch as a low-cost and bifunctional binder enables shuttle-free aqueous zinc-iodine batteries. *Rare Metals* **43**, 6351-6361 (2024).

5 Liang, X. *et al.* Customized design of R-SO_3H-containing binders for durable iodine-loading cathode of zinc-iodine batteries. *Adv. Energy Mater.* **15**, 2500673 (2025).

6 Zhang, S. J. *et al.* Polyiodide confinement by starch enables shuttle-free Zn-iodine batteries. *Adv. Mater.* **34**, 2201716 (2022).

7 Xu, J. *et al.* ZIF-8 derived porous carbon to mitigate shuttle effect for high performance aqueous zinc-iodine batteries. *J. Colloid Interface Sci.* **610**, 98-105 (2022).

8 Zhu, L. *et al.* Integrated trap-adsorption-catalysis nanoreactor for shuttle-free aqueous zinc-iodide batteries. *Adv. Funct. Mater.* **34**, 2409099 (2024).
9 Qu, W. *et al.* Ni Single-atom bual catalytic electrodes for long life and high energy efficiency zinc-iodine batteries. *Small* **20**, 2310475 (2024).
10 Yang, F. *et al.* Single atom catalysts for triiodide adsorption and fast conversion to boost the performance of aqueous zinc-iodine batteries. *Energy Environ. Sci.* **16**, 4630-4640 (2023).
11 Wei, F. *et al.* Mesoporous poly(3,4-ethylenedioxythiophene): poly(styrenesulfonate) as efficient iodine host for high-performance zinc–iodine batteries. *ACS Nano* **17**, 20643-20653 (2023).
12 Zhao, S. *et al.* Robust I···H-O intramolecular halogen bond boosts reversible I_3^-/I^- redox behavior for sustainable potassium-iodine batteries. *J. Am. Chem. Soc.* **147**, 669-677 (2025).
13 Bi, H. *et al.* Multifunctional janus separator engineering for modulating zinc oriented aspectant growth and iodine conversion kinetics toward advanced zinc-iodine batteries. *Adv. Funct. Mater.* **35**, 2423115 (2025).
14 Yang, P. *et al.* Ionic selective separator design enables long-life zinc-iodine batteries via synergistic anode stabilization and polyiodide shuttle suppression. *Adv. Funct. Mater.* **34**, 2410712 (2024).
15 Wu, H. *et al.* Aqueous zinc-iodine pouch cells with long cycling life and low self-discharge. *J. Am. Chem. Soc.* **146**, 16601-16608 (2024).
16 Hao, J. *et al.* Low-cost and non-flammable eutectic electrolytes for advanced Zn-I_2 batteries. *Angew. Chem., Int. Ed.* **62**, e202310284 (2023).
17 Yang, X. *et al.* Lewis acid-base effect and protonation in electrolyte engineering enable shuttle-free, dendrite-free, and HER-free aqueous Zn-I_2 batteries. *Energy Stor. Mater.* **78**, 104268 (2025).
18 Wang, K. *et al.* A bioimmune mechanism-inspired targeted elimination mechanism on the anode interface for zinc-iodine batteries. *Chem. Sci.* **16**, 7227-7238 (2025).
19 Wen, Z. *et al.* Weakening the space charge layer effect through tethered anion electrolyte and piezoelectric effect toward ultra-stable zinc anode. *Adv. Mater.* **36**, 2407390 (2024).
20 Liu, J., Chen, S., Shang, W., Ma, J. & Zhang, J. In situ formation of 3D ZIF-8/MXene composite coating for high-performance zinc-iodine batteries. *Adv. Funct. Mater.* **35**, 2422081 (2025).
21 Wang, G. *et al.* In situ construction of multifunctional surface coatings on zinc metal for advanced aqueous zinc-iodine batteries. *Adv. Energy Mater.* **14**, 2303221 (2023).
22 Chen, H. *et al.* Bio-inspired biomass hydrogel interface with ion-selective responsive sieving mechanism for corrosion-resistant and dendrite-free zinc-iodine batteries. *Energy Stor. Mater.* **76**, 104113 (2025).
23 Shang, W. *et al.* Boosting Zn||I_2 battery's performance by coating a zeolite-based cation-exchange protecting layer. *Nano-Micro Lett.* **14**, 82 (2022).

Q11. *"The author's assertion that ONF's large capacitance gain is due to increased active site density is not substantiated. Relevant characterization data must be provided to support this assertion. Furthermore, the specific surface area and porosity parameters of the electrodes must be clarified when different binders are used."*

Reply to the Reviewer:

Thank you for your highly valuable feedback. In the revised manuscript, we have carefully modified the related descriptions. Following your insightful suggestion, we conducted BET tests on the iodine hosts to obtain specific surface area and pore size distribution data for hosts prepared with different binders. The results are presented in Supplementary Fig. 18.

The nitrogen adsorption-desorption isotherms of cellulose-based iodine hosts exhibit significantly larger hysteresis loops compared to PVDF-based host, indicating that iodine hosts prepared using cellulose as a binder possess a more developed porous structure. The calculated BET specific surface areas for PVDF-, CNF-, and ONF-based iodine hosts are 963.52, 1070.60, and 1025.23 m^2 g^{-1}, respectively. These values demonstrate that the ONF-based host does not possess the highest specific surface area, confirming that the enhanced electrochemical performance cannot be simply attributed to surface-area enlargement.

Pore size distribution analysis further reveals that, unlike the PVDF-based host (with pore sizes mainly centered at ~23.8 nm), cellulose-based hosts exhibit broad mesoporous distributions (2-50 nm). Importantly, compared with the CNF-based host, the ONF-based host shows a shift toward smaller mesopores, indicating higher packing density and stronger interchain entanglement of the binder network. This structural feature supports the formation of a thin yet dense conformal coating on AC@I_2 particles, which shortens electron-transport pathways and suppresses polyiodide leakage without blocking ion access. These effects are consistent with the observed increase in electronic conductivity (0.50 S cm^{-1} for ONF *vs.* 0.33 S cm^{-1} for CNF) and the higher pseudocapacitive contribution of the ONF-based cathode.

Taken together, the BET and conductivity results indicate that the improved capacitive behavior of ONF-based cathodes arises not from higher surface area or porosity, but from optimized binder packing, enhanced interfacial contact, and improved charge-transfer kinetics, enabled by hydroxyl-chemistry regulation.

Revised:

(Page 10, lines 208-210)

BET measurements (Supplementary Fig. 18) show that, compared to CNF, the ONF-based host exhibits a pore-size distribution shifted toward smaller mesopores, indicating higher packing density and stronger interchain entanglement.

(Page 11, lines 235-236)

Notably, the ONF-based cathode achieved a remarkable pseudocapacitive contribution of 90.42% (Fig. 4b), exceeding those of the CNF (78.66%) and PVDF (79.04%) electrodes. This enhanced pseudocapacitive behavior reflects faster iodine redox kinetics for ONF-based cathodes [41-43].

(Supplementary Page 16)

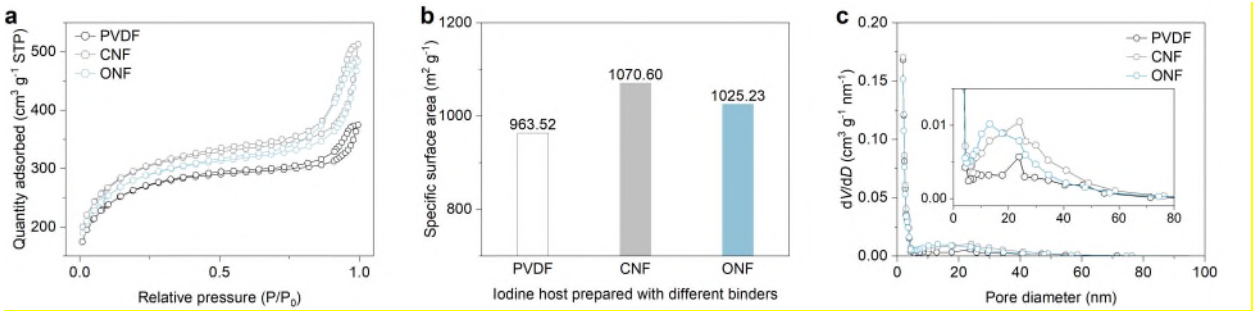

Supplementary Fig. 18. Characterization of porous structures in iodine hosts (without iodine) fabricated using different binders. **a,** Nitrogen adsorption-desorption isotherms. **b,** Specific surface area. **c,** Pore size distribution curves.

Q12. *"Although the manuscript title emphasizes 'hydrogen bond chemistry', it fails to establish a structure-property relationship between hydrogen bonding and enhanced battery performance, such as iodine species conversion and vanadium species dissolution suppression. Further refinement of the manuscript 's logical flow is required."*

Reply to the Reviewer:

Thank you for this important comment. We would like to clarify that the structure-property relationship between hydrogen-bond chemistry and electrochemical performance has been systematically strengthened throughout the revised manuscript, largely in response to you and other reviewer comments, and these improvements collectively address the concern raised here.

Specifically, the revised manuscript now explicitly links hydrogen-bond regulation to performance through multiple, mutually reinforcing analyses:

(i) quantitative evaluation of hydrogen-bond density and energy (FTIR deconvolution, MD simulations),

(ii) conformational and structural consequences of hydrogen-bond reorganization (molecular modeling, packing density, swelling resistance, mechanical integrity), and

(iii) direct electrochemical manifestations, including suppressed polyiodide accumulation, accelerated iodine redox conversion (in situ UV-vis, in situ Raman), reduced polarization (GITT/DRT), and mitigated vanadium dissolution and self-discharge in Zn-V_2O_5 systems.

In addition, the logical flow of the manuscript has been refined to more clearly follow a hydrogen-bond chemistry-electrode architecture-interfacial stabilization-electrochemical behavior sequence, with explicit cross-referencing between structural descriptors and performance metrics. These revisions were implemented across the Results and Discussion sections and are summarized in the revised figure organization and mechanistic schematics.

Therefore, while hydrogen-bond chemistry is highlighted in the title, it is now directly supported by quantitative, structural, and electrochemical evidence, establishing a clear and causal structure–property relationship rather than a correlative description. We hope these revisions satisfactorily address your concern.

To explicitly address this concern, we added a dedicated Supplementary Note 8 that systematically integrates hydrogen-bond chemistry, structural evolution, and electrochemical performance into a single, coherent structure-property-performance framework.

Revised:

(Page 19, lines 408-409)

In this work, we have demonstrated a hydroxyl chemistry regulation strategy that transforms natural cellulose into a high-performance binder for aqueous zinc ion batteries (Supplementary Note 9).

(Supplementary Pages 37-39)

Supplementary Note 9

Hydroxyl chemistry-driven structural optimization and performance enhancement mechanism

To clarify the intrinsic connection between material design, structural evolution, and electrochemical performance enhancement in this work, this section systematically elaborates the complete structure-property-performance relationship triggered by C2-C3 bond cleavage and governed by hydroxyl chemistry regulation.

Through periodate-borohydride treatment (Supplementary Figs. 1-2), selective cleavage of the C2-C3 bonds within anhydroglucose unit (AGU) rings was achieved, yielding oxidized nanofibrillated cellulose (ONF) (Fig. 2a-c). This molecular “ring-opening” process disrupts the intrinsic rigidity of AGU rings and enhances the rotational freedom and accessibility of hydroxyl groups (Supplementary Fig. 3), thereby reducing steric constraints on chain packing. Concurrently, charge redistribution induced by bond cleavage drives a moderate contraction of the cellulose helical conformation and promotes the formation of a denser and more stable intermolecular hydrogen-bonding network.

Quantitative Raman analysis (Supplementary Fig. 4) confirms a significant increase in intermolecular hydrogen-bond fraction in ONF, while molecular dynamics simulations (Supplementary Fig. 5) reveal both an increased hydrogen-bond population and enhanced resistance to thermal perturbation. DFT calculations (Fig. 2e and Supplementary Fig. 6) further demonstrate that additional energetically favorable hydrogen-bond configurations are accessible between ONF chains. Molecular electrostatic potential analysis (Fig. 2f) indicates that hydroxyl hydrogen atoms on the ONF surface exhibit increased positive potential, strengthening their role as hydrogen-bond donors. Together, these molecular- and electronic-level modifications establish the structural foundation for performance enhancement.

These molecular-scale changes directly dictate the macroscopic assembly behavior and interfacial properties of ONF. Enhanced bond rotation and optimized surface potential (Fig. 2g) increase chain flexibility and promote outward orientation of active hydroxyl groups (Fig. 2d and Supplementary Fig. 7). As a result, ONF assembles into densely packed, continuous films during electrode fabrication (Fig. 3a and Supplementary Fig. 12), forming thin yet compact coating layers on active material particles (Fig. 3f and Supplementary Figs. 16-18). This architecture imparts superior mechanical robustness in both dry and wet states and significantly suppresses electrode swelling (Fig. 3h and Supplementary Figs. 19-21), directly reflecting the stability of the underlying hydrogen-bonding network.

During electrochemical operation, this hydrogen-bond-reinforced coating enables multiple synergistic enhancement mechanisms. In Zn-I_2 batteries, it functions as a robust physical barrier that restricts polyiodide dissolution and macroscopic diffusion (Fig. 5c-f), while exposed, highly polar hydroxyl groups provide strong chemical anchoring sites. Visual adsorption experiments (Fig. 5a), XPS analysis (Fig. 5b and Supplementary Figs. 33, 34), and DFT adsorption energies (Fig. 5g) collectively confirm the superior polyiodide binding capability of ONF. The synergy between *physical confinement* and *chemical anchoring* is essential for suppressing the shuttle effect.

Simultaneously, the dense and integrated coating shortens electron-transport pathways (Fig. 3g) while maintaining efficient Zn^{2+} permeability (Supplementary Fig. 22), creating an optimized charge-transport microenvironment. This combination lowers iodine redox energy barriers and accelerates reaction kinetics (Fig. 5h, i), consistent with reduced polarization, increased pseudocapacitive contribution, and faster kinetics observed experimentally (Fig. 4a-c). After prolonged cycling, ONF-based cathodes retain structural integrity, whereas CNF-based electrodes exhibit fiber degradation (Fig. 6a-c and Supplementary Figs. 38-40), directly demonstrating the importance of hydrogen-bond-mediated mechanical stability.

For Zn-V_2O_5 batteries, performance enhancement (Fig. 6h, i) likewise originates from the durable ONF coating, which suppresses vanadium dissolution (Supplementary Figs. 49-51) and reduces vanadium migration to the Zn anode (Fig. 6j and Supplementary Fig. 55), demonstrating the universality of this hydrogen-bond engineering strategy.

In summary, precise molecular “surgery” via C2-C3 bond cleavage initiates a cascade of optimizations spanning electronic structure, intermolecular interactions, and macroscopic assembly. The resulting reinforced hydrogen-bond network manifests as a unique coating architecture combining dense packing, high mechanical stability, and high interfacial activity. Through synergistic physical-chemical regulation, this structure enables effective active-species confinement, accelerated redox conversion, optimized charge transport, and long-term electrode stabilization. This explicit structure-property-performance relationship not only explains the superior functionality of ONF as a binder, but also establishes hydroxyl chemistry regulation as a general design principle for next-generation aqueous battery interface materials.

Reviewer #2:

"The use of naturally abundant biopolymers in sustainable battery technology is rising, as they offer chemical tunability to improve ion regulation and enhance electrochemical performance. This study serves as an excellent example by demonstrating that modifying the hydroxyl groups of cellulose provides an effective means to this end. The authors conclusively prove, through both theoretical and experimental evidence, that selectively cleaving the C2-C3 bonds of its glucose units transforms cellulose into a powerful functional binder. This binder exhibits strong affinity and compatibility with cathode active materials, enabling uniform electrode coverage and robust interactions with dissolution-prone species, which collectively promote stable/fast ion diffusion and redox kinetics. The effectiveness and broad applicability of this strategy are demonstrated across various cathode systems, including iodine, V_2O_5, and $LiMn_2O_4$ in aqueous batteries. Overall, this work significantly advances the fundamental understanding of cellulose hydroxyl chemistry, offering valuable insights for the rational design of bio-based binders in high-performance battery systems. Therefore, this interesting work is recommended for publication in Nature Communications after the following minor comments are addressed:"

Reply to the Reviewer:

We sincerely appreciate your positive feedback and highly valuable comments. Our point-by-point responses to your remarks are provided below.

Q1. *"The density of hydrogen bonding network is enhanced after cellulose modification. Could this lead to more severe electrode swelling behavior? Authors are encouraged to provide more discussions on this point."*

Reply to the Reviewer:

Thank you for this important comment regarding the possible impact of an enhanced hydrogen-bonding network on electrode swelling. To address this point, we performed electrolyte immersion experiments to quantitatively assess the swelling behavior of cellulose-based cathodes by comparing their thickness before and after soaking in 2 M $ZnSO_4$ electrolyte. The results are provided in the newly added Supplementary Fig. 21. After immersion for 5 days, the swelling ratios of the CNF and ONF cathodes were 4.03% and 3.28%, respectively. Notably, despite possessing a higher density of hydrogen bonding, the ONF cathode exhibits lower swelling than the CNF counterpart.

This behavior can be attributed to the synergistic effect of densified packing and enhanced physical entanglement in ONF. Previous studies have shown that tightly packed and physically entangled fibrous networks effectively restrict polymer chain mobility and suppress solvent-induced expansion (*Adv. Funct. Mater.*, 2025, e15830). In ONF, hydroxyl-chemistry regulation not only strengthens intermolecular hydrogen bonding but also promotes closer chain packing and network cohesion, which limits free volume and reduces water uptake.

Therefore, the increased hydrogen-bonding density in ONF does not lead to aggravated swelling. Instead, it contributes to a more compact and mechanically reinforced binder network that is less susceptible to electrolyte-induced swelling, which is beneficial for long-term electrode stability.

Revised:

(Pages 10-11, lines 214-217)

Enhanced wet-state mechanical robustness (Supplementary Fig. 20) together with suppressed thickness variation after electrolyte soaking (Supplementary Fig. 21) indicates that the densified and cohesive ONF binder network enables mechanical integrity even in aqueous electrolyte environment [38,39].

(Supplementary Page 18)

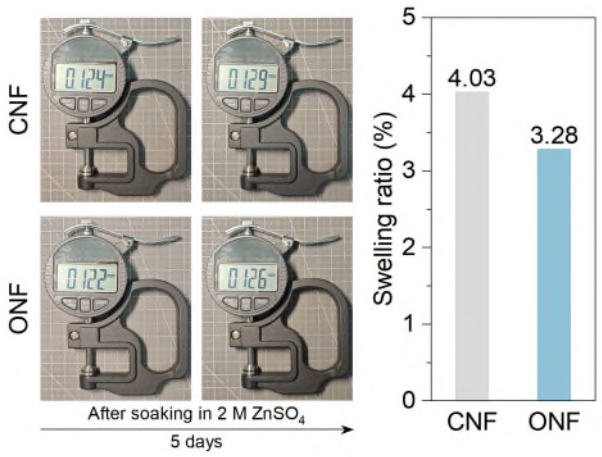

Supplementary Fig. 21. Thickness variation and swelling ratio of CNF and ONF cathodes before and after electrolyte immersion.

Q2. *"Error bars are missing from the cathode conductivity plot (Fig. 3g), revisions are suggested to address this."*

Reply to the Reviewer:

Thank you for your valuable suggestion. In the revised version, we have supplemented the four-probe test data (Supplementary Table 2). The iodine cathodes we prepared exhibit excellent uniformity. Consequently, although slight differences in forward and reverse voltages were observed during multi-point testing, the calculated conductivity values were identical, resulting in a standard deviation of zero. Therefore, error bars cannot be meaningfully displayed in the corresponding figure.

Revised:

(Page 10, line 211)

Electrical conductivity measurements (Fig. 3g and Supplementary. Table 2) showed that the ONF-based cathode achieved a conductivity of 0.50 S cm^{-1}, which is approximately 50% higher than that of the CNF-based counterpart (0.33 S cm^{-1}).

(Supplementary Page 40)

Supplementary Table 2. Four-probe measurement data for CNF-based and ONF-based electrodes.

Number	Forward voltage (mV)	Reverse voltage (mV)	Electrical resistance (kΩ·cm)	Electrical conductivity (S cm^{-1})
CNF-1	0.03	0.03	0.003	0.3333
CNF-2	0.03	0.03	0.003	0.3333
CNF-3	0.03	0.03	0.003	0.3333
CNF-4	0.04	0.02	0.003	0.3333
CNF-5	0.02	0.04	0.003	0.3333
ONF-1	0.01	0.03	0.002	0.5
ONF-2	0.01	0.02	0.002	0.5
ONF-3	0.01	0.03	0.002	0.5
ONF-4	0.02	0.02	0.002	0.5
ONF-5	0.02	0.02	0.002	0.5

Q3. *"Why does the CNF-based cathode exhibit larger polarization in the CV tests and higher high-frequency impedance in the DRT analysis compared to the PVDF-based electrode?"*

Reply to the Reviewer:

Thank you for your careful review. During the preparation process, the solvents used for the PVDF-based iodine cathode and the cellulose-based (CNF and ONF) iodine cathodes are NMP and water, respectively. Consequently, the PVDF cathode requires a higher temperature (60 °C) to remove NMP, resulting in a significantly lower iodine loading (1.3 mg cm^{-2}) compared to the cellulose-based cathodes (4.0 mg cm^{-2}). Given that the electronic conductivity of iodine is only 7.6×10^{-8} S cm^{-1} (*Energy Environ. Sci.*, 2025, 18, 6799-6808), a higher iodine loading tends to degrade the electrode's conductivity. Thus, the CNF cathode exhibits higher impedance in the high-frequency region of the DRT spectrum, which represents charge transfer, leading to more pronounced polarization in CV tests. In contrast, ONF achieves denser packing through the construction of a compact hydrogen-bonding network, effectively improving the cathode's conductivity and thereby delivering superior electrochemical performance.

Q4. *"The degree of substitution or the percentage of C2-C3 bonds cleaved is important for establishing a clear structure-property relationship. This information should be provided."*

Reply to the Reviewer:

Thank you for this important comment. This point closely relates to the issue raised in Reviewer 1's Comment Q1, and in response to that suggestion we have now quantitatively evaluated the degree of AGU ring opening and correlated it with electrochemical performance. By adjusting the $NaIO_4$/AGU molar ratio, cellulose samples with different degrees of ring opening were prepared and systematically characterized. The resulting extracyclic hydroxyl contents, reaction yields, and corresponding electrochemical performances (specific capacity) are summarized in Supplementary Fig. 2 and Supplementary Table 1, which together establish a clear structure-property relationship. We show that increasing the degree of C2-C3 bond cleavage enhances electrochemical performance

up to an optimal level, beyond which excessive ring opening leads to diminished yield and marginal performance gains. On this basis, a $NaIO_4$/AGU molar ratio of 1:1 was identified as the optimal condition, balancing ring-opening degree, material yield, and electrochemical performance.

Revised:

(Page 5, lines 95-96)

We employed a periodate-borohydride treatment to open the cyclic conformation of the AGUs in pristine cellulose (CNF), producing an oxidized cellulose binder (ONF) with a disrupted ring structure under an optimized $NaIO_4$/AGU molar ratio of 1:1 (Supplementary Note 1, Supplementary Figs. 1, 2 and Supplementary Table 1).

(Supplementary Page 8)

Supplementary Note 1

As the $NaIO_4$/AGU molar ratio increases, the content of extracyclic hydroxyl (reflecting the degree of ring opening) rises gradually (Supplementary Fig. 2d, from 1.7 mmol g^{-1} at a ratio of 0.25 to 6.7 mmol g^{-1} at a ratio of 4). Concurrently, the yields from periodate oxidation, borohydride reduction, and the overall yield all exhibit a decreasing trend (Supplementary Fig. 2a-c; the total yield declines from 81.44% at a ratio of 0.25 to 0.26% at a ratio of 4).

The specific capacity of the iodine cathode increases with the initial rise in ring opening (Supplementary Fig. 2e, f). For instance, at a molar ratio of 1, the extracyclic hydroxyl content reaches 4 mmol g^{-1}, and the specific capacity rises to 150.01 mAh g^{-1} (an increase of approximately 18.3% compared with the unmodified sample), while the total yield remains relatively high at 62.81%. When the molar ratio is further increased to 2, the degree of ring opening continues to rise, but the total yield drops sharply to 42.14%, and the gain in specific capacity is only about 3.5%.

In summary, while increasing the ring-opening degree of cellulose can improve electrochemical performance, an excessively high degree of ring opening results in a dramatic reduction in yield. Therefore, a $NaIO_4$/AGU molar ratio of 1:1 was selected, as it achieves an optimal balance among ring-opening degree, yield, and electrochemical performance.

(Supplementary Page 9)

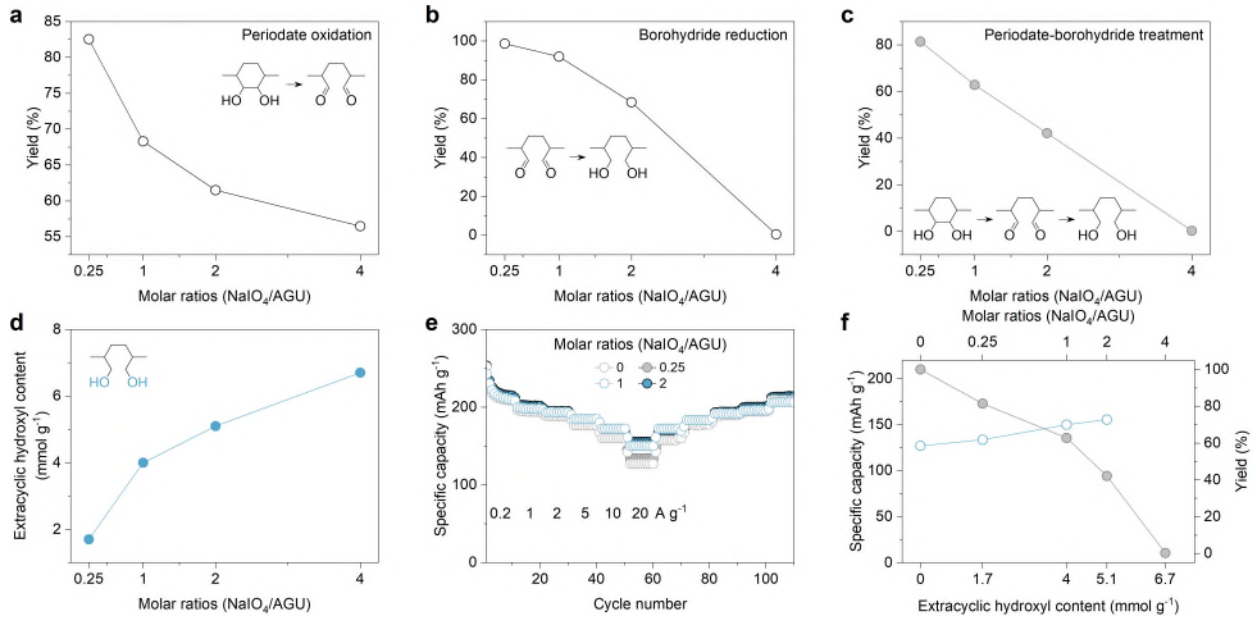

Supplementary Fig. 2. Synthesis parameters, properties, and corresponding cathode performance for ONF. **a-c,** Reaction yields at different $NaIO_4$/AGU molar ratios: **a,** periodate oxidation; **b,** borohydride reduction; **c,** total yield. **d,** Quantified content of extracyclic hydroxyl groups versus $NaIO_4$/AGU ratios. **e,** Rate performance of iodine cathodes prepared from ONFs with varying degrees of ring opening. **f,** Correlation between the degree of ring opening (extracyclic hydroxyl content) and the resulting specific capacity and total synthesis yield.

(**Supplementary Page 40**)

Supplementary Table 1. Synthesis parameters, key properties (yield, extracyclic hydroxyl content), and cathode performance (discharge capacity at 20 A g^{-1}) for ONFs prepared from CNF under varying conditions.

Molar ratios ($NaIO_4$/AGU)	Periodate oxidation yield	Borohydride reduction yield	Total yield	Extracyclic hydroxyl content (mmol g^{-1})	Specific capacity at 20 A g^{-1} (mAh g^{-1})
0	-	-	-	-	126.95
0.25	82.54%	98.66%	81.44%	1.7	133.64
1	68.31%	91.94%	62.81%	4	150.01
2	61.50%	68.51%	42.14%	5.1	155.20
4	56.48%	0.46%	0.26%	6.7	-

Q5. *"The design procedure for the shuttle current measurement should be described in the experimental section."*

Reply to the Reviewer:

The shuttle current test was conducted as follows: The assembled zinc-iodine battery was subjected to three cycles of galvanostatic charge-discharge at 0.2 A g^{-1}. Subsequently, it was discharged to 0.6 V (*vs.* Zn^{2+}/Zn) under constant current and then charged to 1.37 V (*vs.* Zn^{2+}/Zn). The mode was then

switched to potentiostatic polarization, maintaining the voltage at 1.37 V (*vs.* Zn^{2+}/Zn) for several hours. Due to the presence of polyiodide shuttle effects, a steady-state current is generated within the battery. The magnitude of this current reflects the severity of the shuttle effect; a smaller steady-state current indicates a weaker shuttle effect.

Revised:
(Pages 21-22, lines 468-471)
The shuttle current test was performed as follows: after five activation cycles at 0.2 A g^{-1} for the assembled zinc-iodine battery, the cells were discharged to 0.6 V and then charged to 1.37 V. The testing mode was then switched to potentiostatic polarization, maintaining the voltage at 1.37 V for several hours while recording the current–time response. All tests were conducted at room temperature.

Reviewer #3:

"In this manuscript, Xu and Chen et al. designed a hydroxyl-chemistry regulation strategy for cellulose biopolymers to overcome the chemical and interfacial limitations of state-of-the-art binders in aqueous zinc batteries. Successfully, the Zn-I_2 battery fabricated with ONF binder achieves a high-rate capability of 150.9 mAh g^{-1} at 20 A g^{-1}, and exceptional capacity retention of 98.07% over 3000 h in a practical pouch cell. In general, this paper is very interesting. In my opinion, this paper can perhaps become publishable if following concerns can be well addressed."

Reply to the Reviewer:

We sincerely appreciate your positive feedback and highly valuable comments. Our point-by-point responses to your remarks are provided below.

Q1-1. *"On page 3, in paragraphs 38-39, the energy density is not only limited by the positive electrode, but also by the utilization rate of the negative electrode."*

Reply to the Reviewer:

Thank you for this helpful clarification. We fully agree that the overall energy density of aqueous batteries is determined by both the positive and negative electrodes, including the utilization efficiency of the Zn anode. In the present manuscript, our discussion emphasizes the positive electrode because the instability and low utilization of high-capacity cathodes (e.g., iodine- and transition-metal–based cathodes) currently represent the dominant bottleneck preventing aqueous batteries from approaching their theoretical energy density.

Revised:

(Page 3, lines 36-37)

In these systems, the performance of the cathode is one of the key factors limiting the energy density, underscoring the importance of cathode materials and electrode design.

Q1-2. *"Figure S24 and its related descriptions seem rather unclear. Where did the lost iodine go? This part of the content needs further revision."*

Reply to the Reviewer:

We sincerely apologize for the lack of clarity in Supplementary Fig. 24 and its related description, which may have obscured the fate of the iodine species. In the revised manuscript, Supplementary Fig. 24 has been replaced by Supplementary Fig. 33, with clarified experimental design and data processing. Under high-temperature open-system condition, polyiodide species in aqueous solution are not chemically decomposed but are gradually lost through volatilization coupled with water evaporation, during which iodine-containing species diffuse into the atmosphere. This process results in a decrease in the polyiodide concentration remaining in solution and corresponding discoloration (Supplementary Fig. 33a). Therefore, the extent of iodine "loss" reflects the ability of the binder to confine polyiodide species in the condensed phase rather than irreversible iodine consumption.

Accordingly, the polyiodide-retention capability of different binders was evaluated by monitoring the residual polyiodide concentration in solution after thermal aging (Supplementary Fig. 33b). We further note that CNF and ONF exhibit different intrinsic background absorbance in the polyiodide spectral region due to their distinct chemical structures (Supplementary Fig. 33c). To eliminate this interference and ensure quantitative reliability, background subtraction was applied to extract the true polyiodide absorbance (Supplementary Fig. 33d). The corrected absorbance data are now used in Fig. 5a to directly compare the polyiodide-confinement capability of different binders.

Revised:

(Page 14, line 286)

The UV-Vis spectra reveals that the characteristic adsorption bands of I_3^- at 288 cm^{-1} and 354 cm^{-1} [46] in a blank polyiodide solution decreased to ~8% of the original intensity after heating at 60 °C for 2 h (Fig. 5a, Supplementary Note 4 and Supplementary Fig. 33).

(Supplementary Page 23)

Supplementary Note 4

Under high-temperature open-system conditions, polyiodide ions in aqueous solution gradually escape together with water evaporation, leading to a decrease in the residual polyiodide concentration and solution discoloration (Supplementary Fig. 33a). The ability of different binders to suppress polyiodide loss can therefore be evaluated by measuring the remaining polyiodide concentration in solution (Supplementary Fig. 33b). Because CNF and ONF exhibit different intrinsic background signals in the polyiodide absorption region (Supplementary Fig. 33c), background subtraction was performed to obtain the true polyiodide absorbance (Supplementary Fig. 33d). The corrected results are summarized in Fig. 5a.

(Supplementary Page 23)

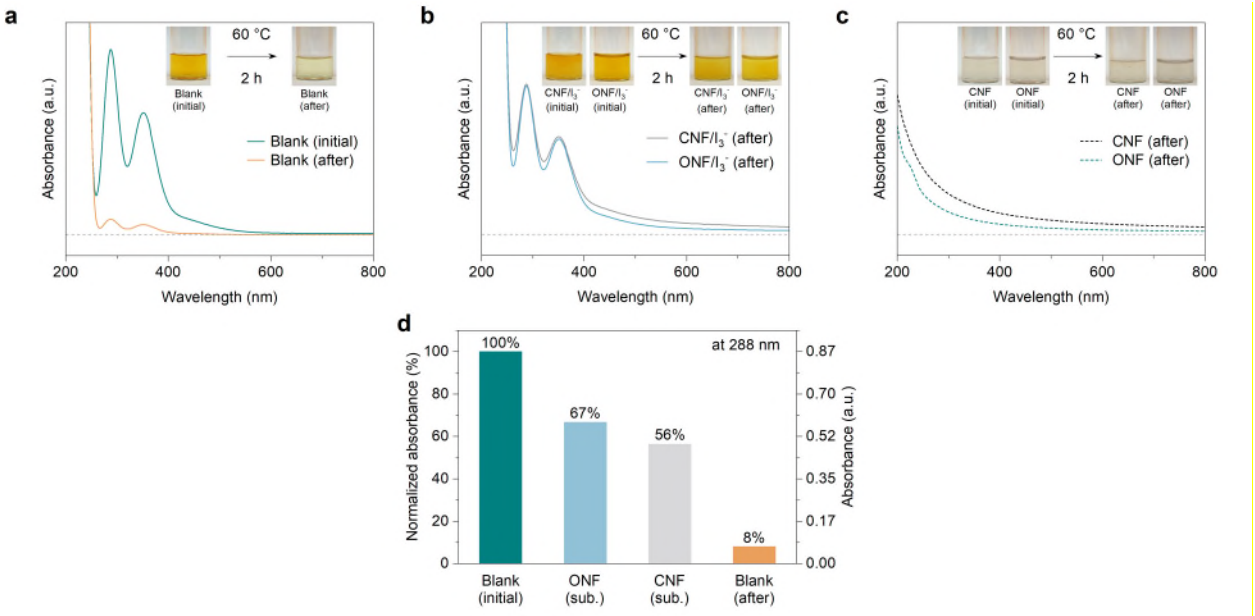

Supplementary Fig. 33. a, UV-Vis spectra of the blank sample before and after heat treatment at 60 °C for 2 h (inset: optical images before and after heating). **b,** UV-Vis absorption spectra of CNF/I_3^- and ONF/I_3^- dispersions after thermal treatment at 60 °C for 2 h (inset: optical images before and after heating). **c,** UV-Vis absorption spectra of CNF and ONF dispersions after thermal treatment at 60 °C for 2 h (inset: optical images before and after heating). **d,** The corrected results are summarized in **Fig. 5a**.

Q1-3. *"The statement 'a fully encapsulated surface' is somewhat misleading. In fact, the ONF network itself is porous."*

Reply to the Reviewer:
Thank you for this important clarification. We fully agree that the ONF network itself is intrinsically porous, and our previous wording could indeed be misleading. Our intention was not to imply a non-porous or impermeable layer, but rather to emphasize the high and continuous surface coverage of active materials achieved by the ONF binder.

In the revised manuscript, we have therefore replaced the phrase "fully encapsulated surface" with more precise descriptions such as "highly coverage" electrode surfaces, explicitly acknowledging the porous nature of the ONF network. These revisions have been applied consistently throughout the text to avoid ambiguity.

Revised:
(Page 9, line 185)
Upon unidirectional vacuum filtration, radial compression transforms the colloidal suspension into a lamellar architecture, yielding a freestanding, uniform coverage electrode in which ONF nanofibers tightly wrap around the active material.

(Page 9, line 191)
Surface morphology comparisons (Fig. 3d and Supplementary Figs. 15, 16) revealed that PVDF-based cathode exposed numerous AC@I_2 particles on the electrode surface, whereas both CNF- and ONF-based cathodes exhibited a continuous nanofibrous coverage layer that covered the active materials.

(Page 9, lines 196, 198)
Notably, the ONF binder yielded a denser and thinner coverage layer compared to the thicker and looser coating observed with CNF, consistent with the conformal lamellar coating architecture proposed in Supplementary Fig. 17.

(Page 16, line 342)
while the ONF-based cathode (Fig. 6c) preserved a highly coverage surface with uniformly distributed nanofiber coverage.

Q1-4. *"It seems that the definite Zn^{2+} diffusion coefficients value has not been calculated in this article."*

Reply to the Reviewer:
Thank you for your valuable feedback. The *D*-value ranges for the charge/discharge processes of the PVDF, CNF, and ONF systems, originally presented in Fig. 4d, have now been included in the supplementary material as Supplementary Table 3.

Revised:

(Pages 11, lines 242)

Galvanostatic intermittent titration technique (GITT) measurements (Fig. 4d, Supplementary Fig. 26 and Supplementary Table 3) were used to evaluate the overall polarization behavior and apparent reaction kinetics of the iodine cathode.

(Supplementary Page 41)

Supplementary Table 3. Range of R_{int}-values and D-values during charge/discharge processes in zinc-iodine batteries with different binder systems.

System	R_{int}-charge (k Ω)	D-charge ($\times 10^{-10}$ cm^2 s^{-1})	R_{int}-discharge (k Ω)	D-discharge ($\times 10^{-10}$ cm^2 s^{-1})
PVDF-based	0.2909-4.6654	0.6681-2.7518	0.0800-8.8254	2.0262-12.2051
CNF-based	0.1985-2.3474	0.8988-11.1279	0.0993-2.1762	7.6373-14.1112
ONF-based	0.1520-1.8413	1.1320-17.2617	0.0671-1.8058	7.8748-24.3069

Q2. *"Whether any residual iodine sources (e.g., iodate or iodide ions) might remain in the ONF samples following the periodate-borohydride treatment of CNF? It would be valuable to briefly discuss the potential influence of such residues on the electrochemical properties."*

Reply to the Reviewer:

Thank you for this important question regarding possible residual iodine species originating from the periodate-borohydride treatment. We carefully examined this possibility and can confirm that no residual iodine-containing species remain in the ONF samples. Specifically, iodine elemental analysis was performed on the as-prepared ONF membranes. As shown in Supplementary Fig. 58a, EDS spectra of ONF are identical to those of pristine CNF, with no detectable iodine signal observed. In addition, high-resolution XPS I 3*d* spectra (Supplementary Fig. 58b), which have a detection limit of approximately 1 at.%, also show no iodine-related peaks in ONF, further confirming the absence of residual iodine species. These results indicate that iodate intermediates generated during periodate oxidation were completely removed during subsequent borohydride reduction and washing steps. To further emphasize this point, we note that iodine signals only appear after intentional polyiodide adsorption, where ONF exhibits significantly stronger I 3*d* intensity than CNF (Supplementary Fig. 34), directly reflecting its enhanced polyiodide affinity rather than residual contamination.

Revised:

(Page 20, lines 428, 432-433)

After further purification and freeze-drying, the obtained ONF was reconstituted as aqueous dispersion. An appropriate mass of cellulose (CNF or ONF) dispersion was filtrated through a filter membrane by vacuum filtration, and the resulting filter cake was allowed to stand at room temperature overnight before being transferred to a 60 ℃ oven for 12 h of drying, then get ONF or CNF paper. No iodine-related signals were detected in the ONF paper (Supplementary Fig. 58).

(Supplementary Page 35)

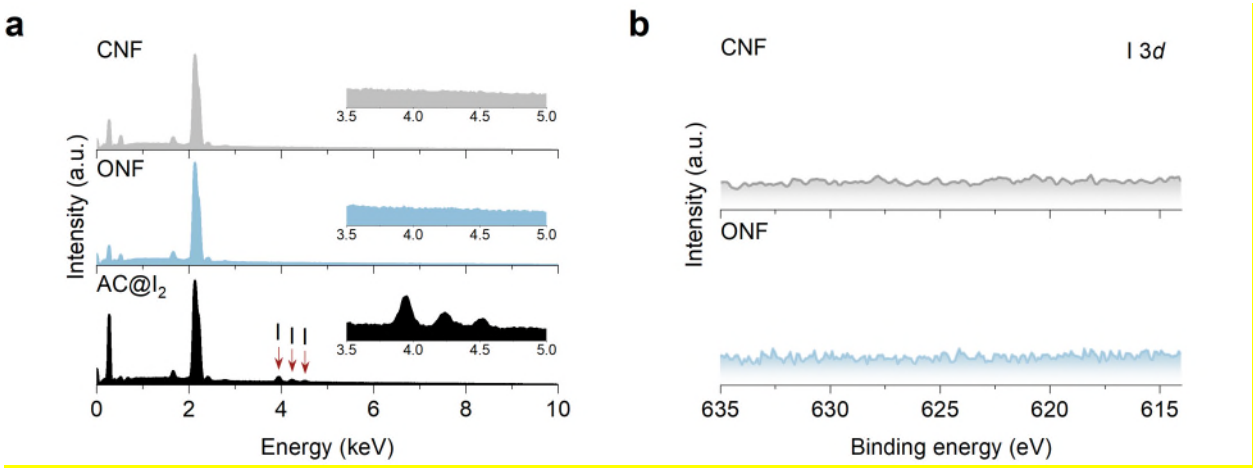

Supplementary Fig. 58. Iodine element detection in fresh cellulose papers. **a,** EDS spectra of CNF paper, ONF paper, and AC@I_2. **b,** XPS I 3*d* spectra of CNF paper and ONF paper.

Q3-1. *"In Figure 3d, more images of various resolutions are needed to illustrate the overall and detailed morphology."*

Reply to the Reviewer:

In the revised manuscript, we have added additional SEM images at multiple magnifications for CNF- and ONF-based cathodes. These images are now provided in Supplementary Fig. 15, to clearly reveal the surface continuity, fiber coverage, and local structural details.

Revised:

(Page 9, lines 189-190)

Surface morphology comparisons (Fig. 3d and Supplementary Figs. 15, 16) revealed that PVDF-based cathode exposed numerous AC@I_2 particles on the electrode surface, whereas both CNF- and ONF-based cathodes exhibited a continuous nanofibrous coverage layer.

(Supplementary Page 16)

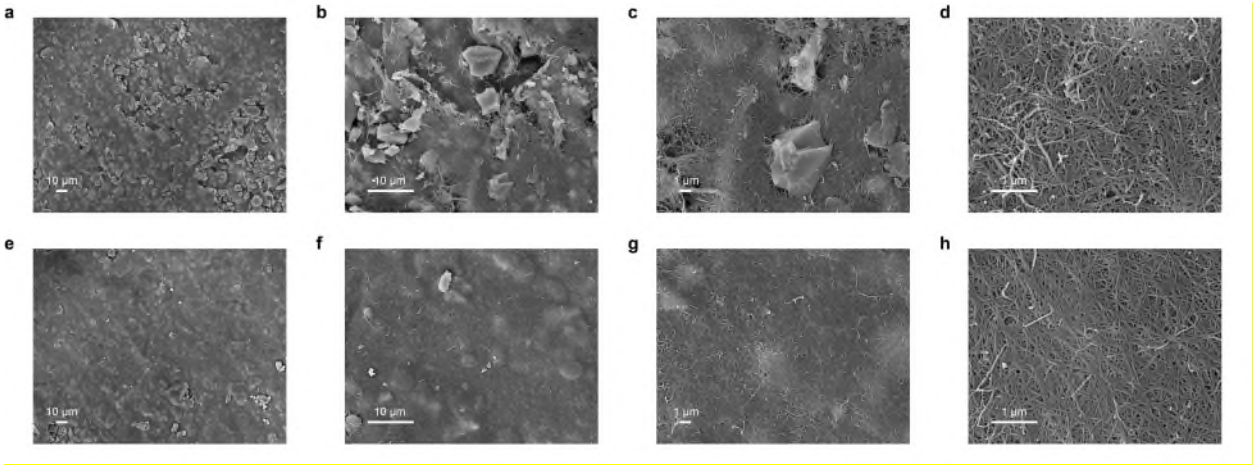

Supplementary Fig. 16. a-d, Surface morphology of the CNF cathode at different magnifications. **e–h,** Surface morphology of the ONF cathode at different magnifications.

Q3-2. *"Was the cracks in Fig. 6a formed during the cyclic test, or did it appear before assembling battery? The SEM images of fresh PVDF electrode sheets need to be tested."*

Reply to the Reviewer:

The SEM images of the PVDF-based cathode at multiple resolutions, both before and after cycling, are provided in Supplementary Figs. 15 and 39, respectively. It can be clearly observed that the freshly prepared PVDF cathode exhibits a smooth and crack-free surface prior to cell assembly, whereas pronounced cracks emerge after prolonged electrochemical cycling. These observations confirm that the cracks shown in Fig. 6a were generated during the cycling process, rather than being present before battery assembly.

Revised:

(Page 9, lines 189-190)

Surface morphology comparisons (Fig. 3d and Supplementary Figs. 15, 16) revealed that PVDF-based cathode exposed numerous AC@I_2 particles on the electrode surface

(Page 16, line 339)

After prolonged cycling, the PVDF-based cathode exhibited severe structural degradation, including extensive cracking across both the electrode matrix and individual I_2@AC particles (Fig. 6a and Supplementary Figs. 38, 39).

(Supplementary Page 15)

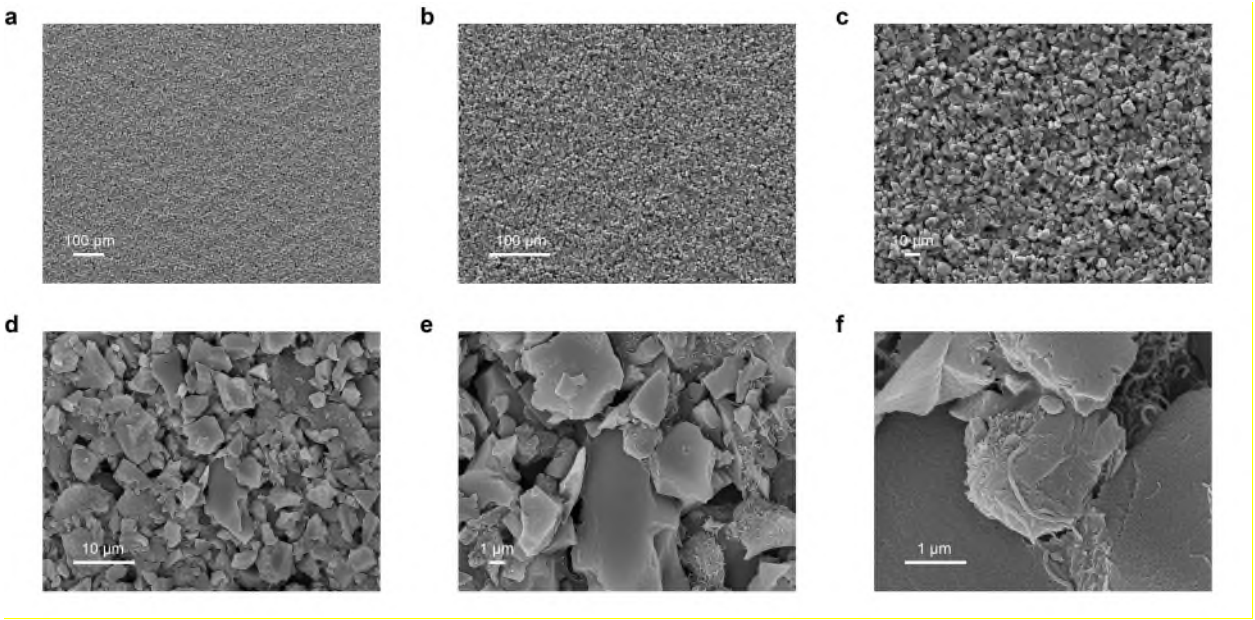

Supplementary Fig. 15. Surface microstructures of PVDF-based cathode at different magnifications.

(Supplementary Page 26)

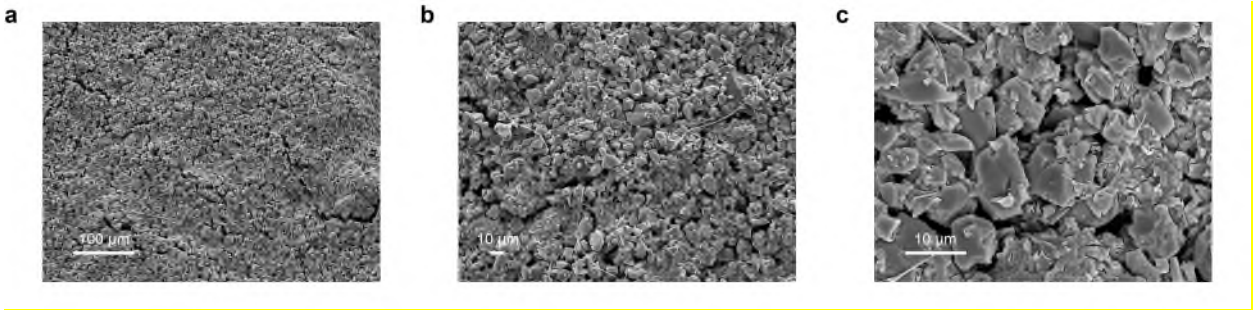

Supplementary Fig. 39. Morphological characterization of the separator-facing surface of cycled PVDF-based cathode.

Q4. *The cycling stability in Figure 4 is currently evaluated at high current densities. To provide a more comprehensive assessment of the battery's performance, we suggest including long-term cycling data at a lower current density, such as 0.2 A* g^{-1}.

Reply to the Reviewer:

We have added long-term cycling data for iodine cathodes with different binders at a low current density of 0.2 A g^{-1}, as shown in Supplementary Fig. 31. At this low rate, the PVDF-based cathode failed after 71 cycles, and the CNF-based cathode failed after 152 cycles, both due to severe polyiodide shuttling and electrode degradation. In contrast, the ONF-based cathode remained stable for over 300 cycles, maintaining a capacity retention of 99.00%, demonstrating its superior ability to stabilize high-capacity iodine cathodes even under low-current, shuttle-prone conditions.

Revised:

(Page 12, lines 265-266)

Shuttle current measurements (Supplementary Fig. 30) further confirmed the ONF binder's suppression of polyiodide migration, with the ONF-based cathode exhibiting the lowest shuttle current (0.49 μA g^{-1}), nearly one-third lower than those of the other cathodes, confirming its effective suppression of polyiodide shuttling during dynamic cycling. Therefore, the ONF-based cathode can operate steadily even at a low current rate of 0.2 A g^{-1}, unlike other electrodes which undergo rapid failure (Supplementary Fig. 31).

(Supplementary Page 22)

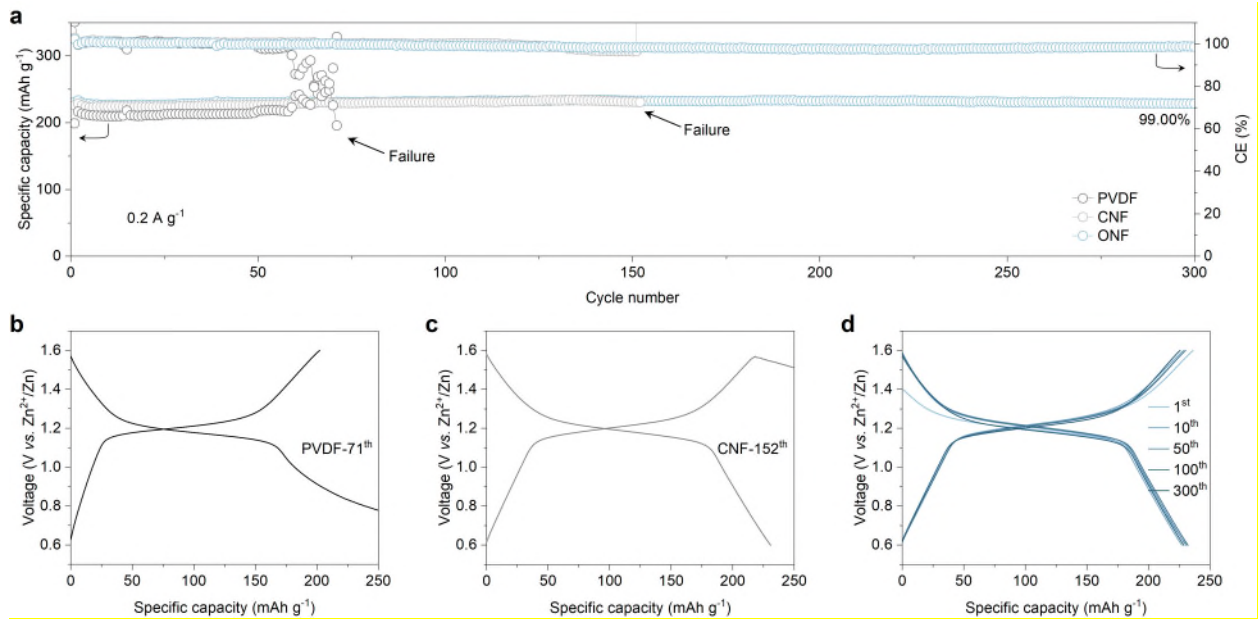

Supplementary Fig. 31. a, Long-term cycling performance of iodine cathodes with different binders at 0.2 A g^{-1}. Galvanostatic charge-discharge curves of failed **b,** PVDF-based and **c,** CNF-based cathodes. **d,** Galvanostatic charge-discharge curves of the ONF-based cathode at different cycle numbers.

Q5-1. *"Self-discharge performance is one of the key performance indicators restricting the development of zinc-iodine batteries, and it is necessary to test the self-discharge performance of the battery during longer self-discharge cycles."*

Reply to the Reviewer:

Based on your valuable suggestion, in addition to the standard 24 h self-discharge test, we have extended the resting duration to 48 h and 96 h to more rigorously assess self-discharge behavior. As shown in Supplementary Fig. 28 and Fig. 4h, the ONF-based cathode consistently exhibited superior self-discharge suppression over prolonged rest periods. Specifically, after resting for 24 h, 48 h, and 96 h, the ONF-based cathode retained 96.45%, 94.08%, and 93.26% of its initial capacity, respectively. These values are markedly higher than those of the CNF-based cathode (95.78%, 92.95%, and 91.43%) and the PVDF-based cathode (94.92%, 91.80%, and 91.23%).

Revised:

(Page 12, lines 256-258)

The ONF-based cathode also demonstrated low self-discharge during rest periods (Fig. 4h and Supplementary Fig. 28), maintaining 96.45%, 94.08%, and 93.26% of its initial capacity after resting for 24 h, 48 h, and 96 h, respectively.

(Page 13, line 274)

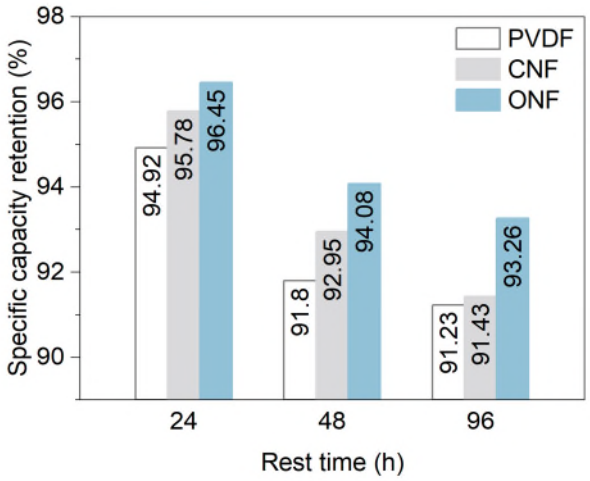

Fig. 4 | h, Capacity retention after different rest periods.

(Supplementary Page 20)

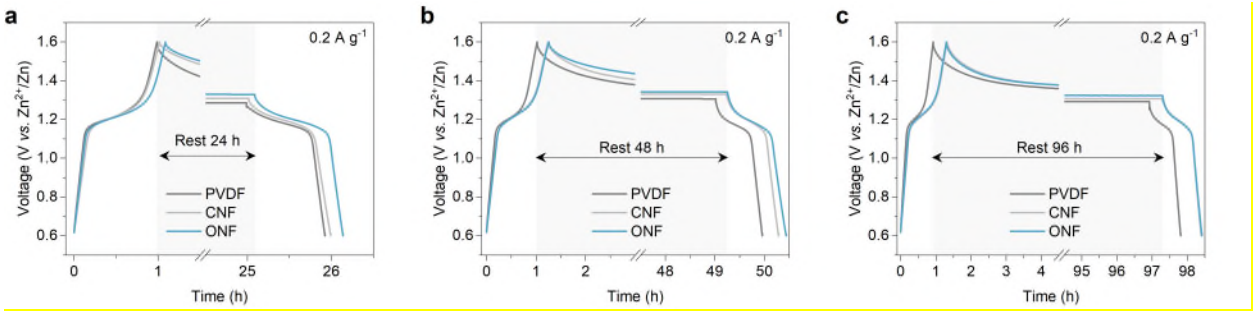

Supplementary Fig. 28. The rest time-voltage curves of zinc-iodine batteries with different cathode binder systems. Rest durations: **a,** 24 h. **b,** 48 h. **c,** 96 h.

Q5-2. *"BTW, in V_2O_5 batteries, does ONF bonding have the effect of suppressing self-discharge?"*

Reply to the Reviewer:

Thank you for this valuable question. Following your suggestion, we extended our investigation to evaluate whether the ONF binder can suppress self-discharge in Zn-V_2O_5 batteries, which involve a distinct redox chemistry from iodine-based systems. As shown in Supplementary Fig. 54. Compared with the PVDF-based system, which exhibited rapid capacity decay (capacity retention of 81.79%

after 24 h and 65.75% after 48 h), both cellulose-based binders significantly improved self-discharge behavior. Notably, the ONF-based system achieved the highest capacity retention, maintaining 87.10% after 24 h and 79.07% after 48 h. These results demonstrate that the beneficial effect of ONF in suppressing self-discharge is not limited to iodine cathodes, but also extends to dissolution-prone transition-metal oxide systems such as V_2O_5.

Revised:

(Page 19, lines 394-396)

Notably, ONF outperformed CNF under high-rate conditions, delivering 220.6 mAh g^{-1} at 5 A g^{-1} versus 179.8 mAh g^{-1}, and maintained superior cycling stability at 2 A g^{-1} (Fig. 6i and Supplementary Fig. 53). ONF also effectively suppresses self-discharge in Zn-V_2O_5 batteries, as evidenced by the higher retention of initial capacity during self-discharge tests (Supplementary Fig. 54).

(Supplementary Page 32)

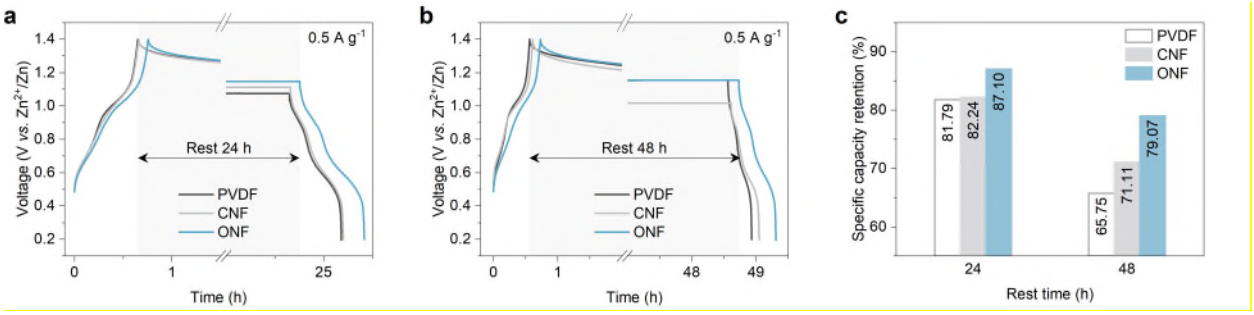

Supplementary Fig. 54. a, Time-voltage curve of Zn-V_2O_5 cell during the 24h resting test. **b,** Time-voltage curve of Zn-V_2O_5 cell during the 48h resting test. **c,** Corresponding capacity retention.

Q6. *"Why is it necessary to prepare high iodine loading electrodes through lamination? Can high loading self-supporting electrodes be prepared in one step? (10.1039 / D5EE01170A; 10.1016 / j.j cis. 2025.138936)?"*

Reply to the Reviewer:

Thank you for recommending these two insightful studies on one-step fabrication of high-loading self-supporting electrodes. We have carefully studied these works and cited them in the revised manuscript (Refs. 49 and 52). We would like to clarify that lamination is not a mandatory requirement for achieving high iodine loading in our system. In this study, lamination of thin paper electrodes was intentionally employed to demonstrate the modularity and assembly flexibility of cellulose-based paper electrodes, rather than to suggest it as the only viable route for fabricating thick electrodes.

In this revised version, we have also prepared an iodine cathode with a thickness of 400 μm and an iodine loading of 9 mg cm^{-2} using a one-step vacuum filtration method (Supplementary Fig. 47). Furthermore, to emphasize the engineering relevance and scalability of our approach, we integrated multiple uniformly sized high-loading iodine cathodes onto a single current collector to assemble a larger-format pouch cell, achieving ampere-hour-level capacity output (Supplementary Fig. 48).

Together, these results demonstrate that the ONF-based binder system supports both one-step high-loading electrode fabrication and modular thick-electrode assembly, offering complementary pathways toward large-format aqueous battery devices.

Revised:

(Page 17, lines 370-373)

Furthermore, a self-supporting iodine cathode (400 μm) was also fabricated via a one-step vacuum filtration process (Supplementary Fig. 47) [49,52]. By integrating multiple uniformly sized high loading iodine cathodes onto a single current collector, a larger-format pouch cell was fabricated, enabling capacity delivery at the ampere-hour level (Supplementary Fig. 48). These results demonstrate the scalability and practical utility of the ONF binder in constructing thick electrodes with high mechanical integrity and continuous ion/electron transport pathways across the thickness direction.

(Supplementary Page 30)

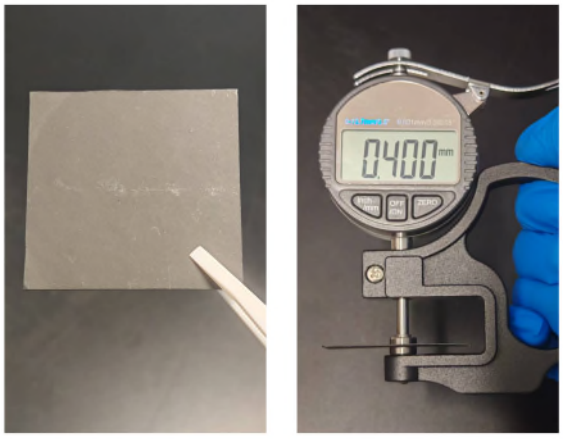

Supplementary Fig. 47. Optical photograph (left) and thickness (right) of ONF-based high-loading iodine cathodes prepared by the one-step method.

(Supplementary Page 30)

Supplementary Fig. 48. a, Schematic diagram, optical photograph, and corresponding **b,** electrochemical performance of the pouch cell with ONF-based high-loading iodine cathodes.

Q7. *"To firmly establish the cycling stability advantage of the ONF electrode, providing the corresponding cycling data for the PVDF-based control electrode would be very helpful for direct comparison."*

Reply to the Reviewer:

The corresponding the long-term cycling performance (at 10 A g^{-1}) of PVDF cathodes was included in Fig. 4i and Supplementary Fig. 29. Both PVDF-based and CNF-based cathodes failed after approximately 5,000 cycles, with the PVDF system experiencing short-circuiting (failure to reach charging voltage) and the CNF system exhibiting capacity decay and low Coulombic efficiency.

Revised:

(Page 12, lines 258, 260)

Meanwhile, the ONF-based cathode exhibited the best cycling stability, retaining 95.16% of its initial capacity after 10,000 cycles at 10 A g^{-1}, corresponding to an ultralow per-cycle capacity decay of just 0.00048% (Fig. 4i and Supplementary Fig. 29).

(Page 13, line 274)

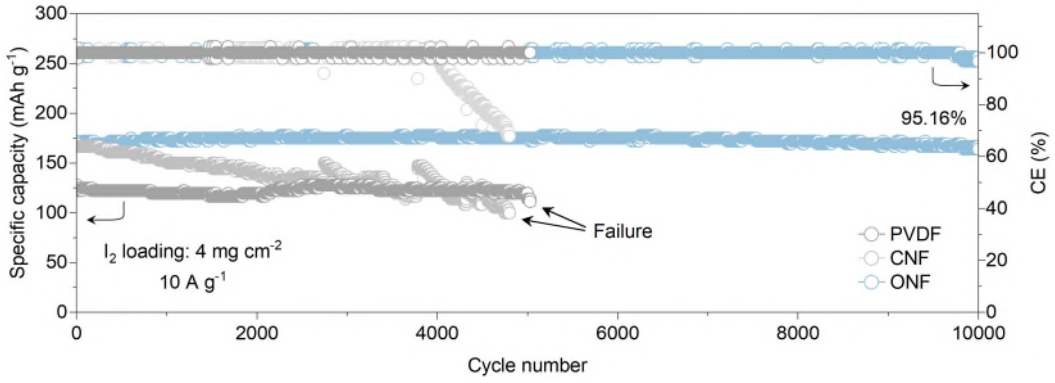

Fig. 4 | i, Long-term cycling stability at 10 A g^{-1} for PVDF-, CNF- and ONF-based cathodes.

(Supplementary Page 21)

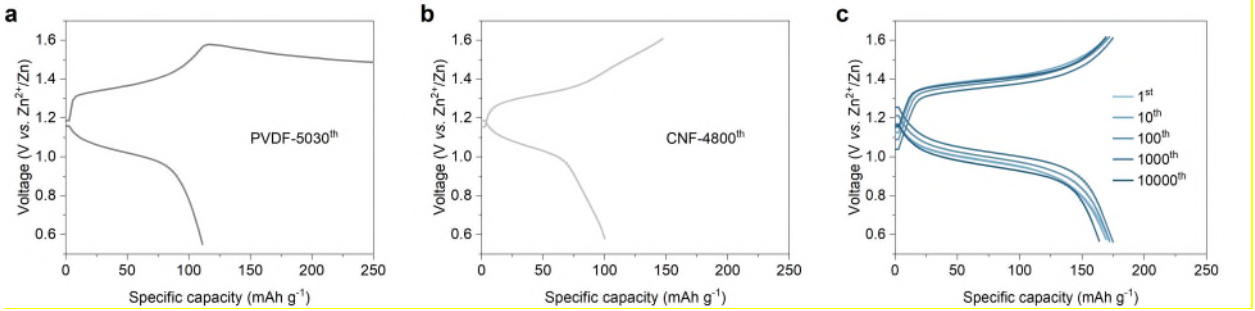

Supplementary Fig. 29. Galvanostatic charge-discharge curves of failed **a,** PVDF-based and **b,** CNF-based cathodes. **c,** Galvanostatic charge-discharge curves of the ONF-based cathode at different cycle numbers.

Q8. *"Please standardize the legend in Fig. 5a to clearly identify which sample each curve corresponds to, ensuring the graph's readability and data clarity."*

Reply to the Reviewer:
We have updated Fig. 5a to make the presentation more standard and clear.

Revised:
(Page 14, line 286)
The UV-Vis spectra reveals that the characteristic adsorption bands of I_3^- at 288 cm^{-1} and 354 cm^{-1} [44] in a blank polyiodide solution decreased to ~8% of the original intensity after heating at 60 °C for 2 h (Fig. 5a, Supplementary Note 4 and Supplementary Fig. 33).

(Page 15, line 307)

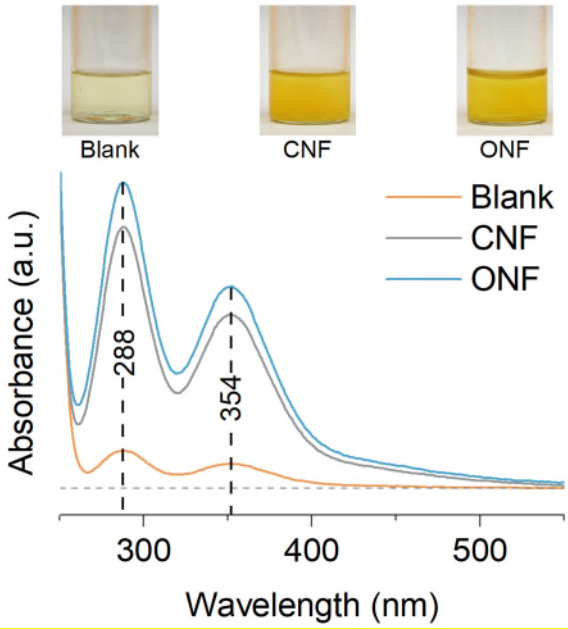

Fig. 5 | a, UV-Vis absorption spectra of cellulose/polyiodide mixed solutions after high-temperature aging (inset: optical photographs showing color differences).

Q9. *"To provide deeper mechanistic insight into the advantageous performance of the ONF electrode, we believe that including in situ Raman spectroscopy data for the CNF-based battery (for comparison with ONF) would be highly informative in revealing the structural evolution differences during operation."*

Reply to the Reviewer:
We have now included in situ Raman spectroscopy data for the CNF-based battery, and the results are presented together with those of the PVDF- and ONF-based systems in the updated Fig. 5f. It is found that the iodine cathode using CNF as the binder exhibits significantly weaker polyiodide

signals during charge/discharge compared to the cathode with PVDF binder. However, due to the less structural integrity of the fibrous network on the CNF-based cathode surface (compared to ONF), its polyiodide signals remain stronger than those in the ONF-based system.

Revised:

(Page 14, lines 304-306)

As shown in Fig.5f, the PVDF-based cathode displayed growing I_5^- signal at 160 cm^{-1} [48] during charging beyond 1.3 V, these polyiodide signals persisted during subsequent discharge. In contrast, cellulose-based cathodes exhibited low I_3^-/I_5^- signal intensities across the entire potential window. Notably, such signals were nearly undetectable for the ONF-based cathode, demonstrating more effective immobilization and accelerated catalytic conversion of iodine intermediates.

(Page 15, line 307)

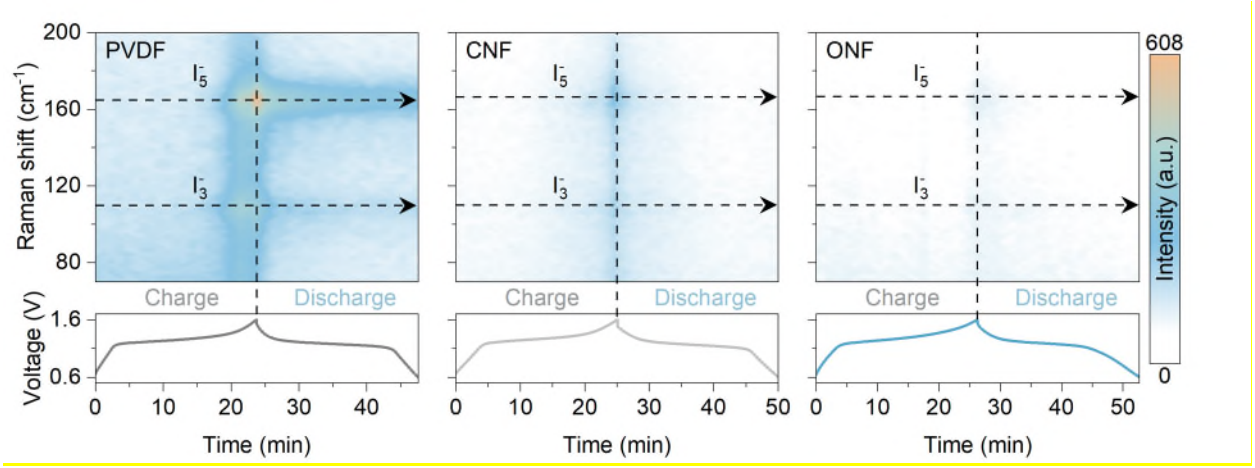

Fig. 5 | f, In situ Raman spectra and corresponding galvanostatic charge/discharge curves for PVDF-, CNF- and ONF-based cathodes.

Q10. *"The logic of the figure presentation in the main text should be reorganized for consistency. Currently, Fig. 5a-b primarily compare CNF and ONF electrodes, while Fig. 5c-g only compare PVDF and ONF. Furthermore, the PVDF control is absent in the long-term cycling figure. This inconsistency creates confusion for readers when interpreting the performance advantages. It is suggested to unify the baseline for comparison, for instance, including CNF, ONF, and PVDF data in all key performance figures (e.g., rate capability, cycling) or to provide a clear explanation in the text for the specific purpose of each comparison set."*

Reply to the Reviewer:

Following your valuable suggestion, we have restructured the figure organization and corresponding descriptions to ensure a unified and transparent comparison framework. Specifically, except for the visual polyiodide adsorption experiments (Fig. 5a, b), all key electrochemical and mechanistic characterizations now consistently include PVDF, CNF, and ONF as comparison baselines, with the revised data incorporated into Figs. 4 and 5 and supported by additional supplementary figures. This

unified presentation enables direct comparison across conventional, cellulose-based, and hydroxyl-regulated binders. We would like to clarify that PVDF was intentionally excluded from the visual polyiodide adsorption experiments (Fig. 5a, b) because it cannot be effectively dispersed in water. The purpose of this specific experiment was to evaluate the intrinsic polyiodide-confinement capability of the binder material itself, independent of electrode fabrication. Importantly, the influence of PVDF on polyiodide behavior is systematically examined and benchmarked in subsequent electrochemical and in situ analyses (Fig. 5c-h), where all three binders are included.

Revised:

(Pages 14-16, lines 296-322)

The in situ UV-Vis results (Fig. 5c, d and Supplementary Fig. 35) revealed that during open-circuit discharge to 0.6 V, the PVDF-based cathode exhibited rapid accumulation of I_3^-, and significant I_3^- concentration persisted even after charging, indicating severe shuttle effects and incomplete iodine redox conversion. In stark contrast, both CNF and ONF-based cathodes (Fig. 5e) displayed negligible I_3^- signals, with the ONF-based cathode showed an almost complete absence of I_3^- accumulation throughout the entire cycle. These trends were reinforced by in situ Raman spectroscopy. As shown in Fig. 5f, the PVDF-based cathode displayed growing I_5^- signal at 160 cm^{-1} [48] during charging beyond 1.3 V, these polyiodide signals persisted during subsequent discharge. In contrast, cellulose-based cathodes exhibited low I_3^-/I_5^- signal intensities across the entire potential window. Notably, such signals were nearly undetectable for the ONF-based cathode, demonstrating more effective immobilization and accelerated catalytic conversion of iodine intermediates.

Density functional theory (DFT) calculations (Fig. 5g) showed ONF exhibited significantly stronger binding energies toward both I_3^- (-0.45 eV) and I_5^- (-0.36 eV), in contrast to CNF with moderate interactions (I_3^-: -0.3 eV; I_5^-: -0.23 eV) and PVDF with much weaker interactions (I_3^-: -0.21 eV; I_5^-: -0.17 eV). Complementary Gibbs free energy calculations of the I_2 reduction pathway (Fig. 5h) demonstrated that while the conversion of I_2 to I^- ($\Delta G < 0$) is thermodynamically favorable in all three systems, ONF further reduced the overall reaction free energy, suggesting that it facilitates faster reaction kinetics by lowering the activation barriers associated with polyiodide redox transitions.

(Page 15, line 307)

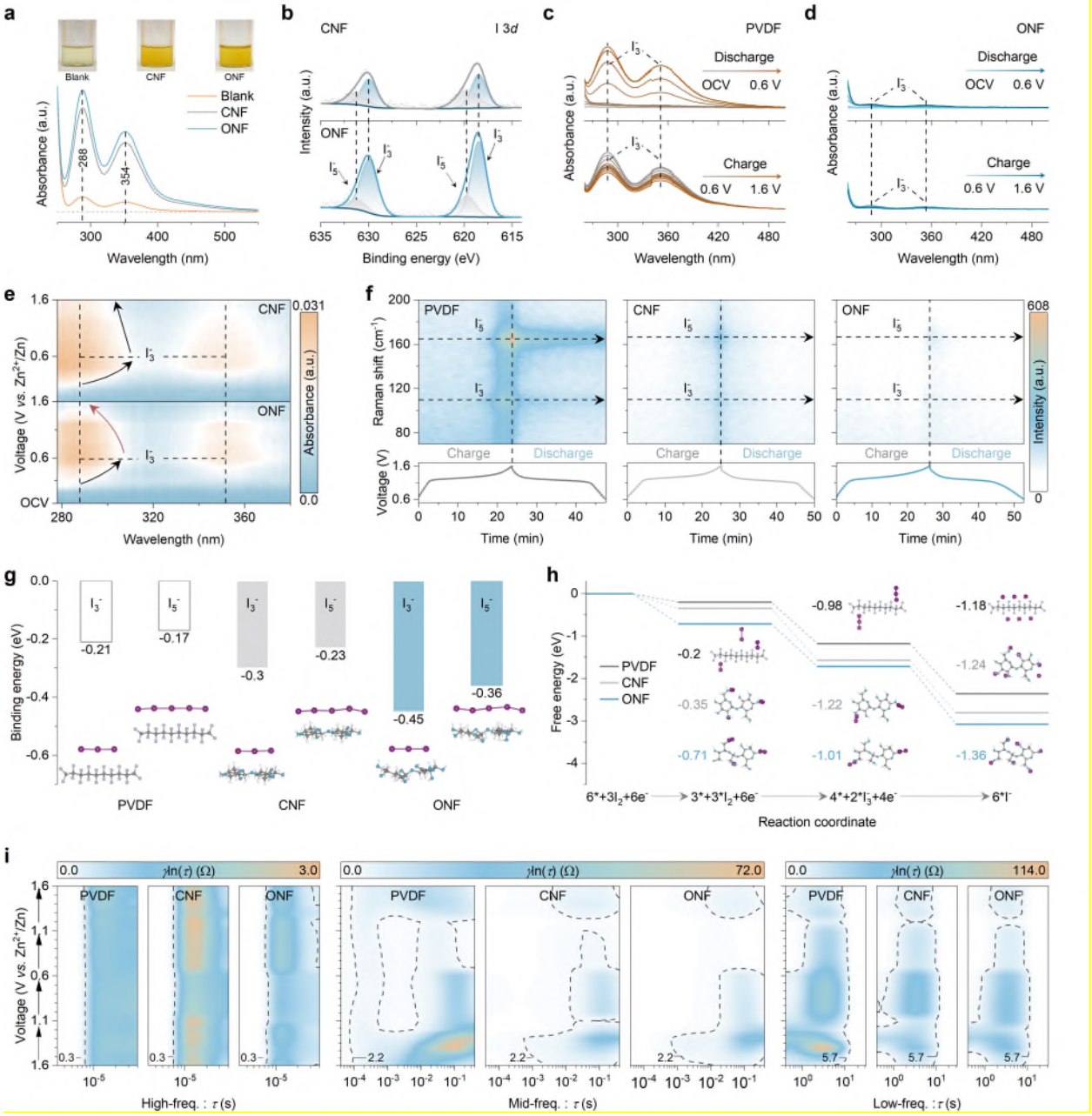

Fig. 5 | Mechanism of hydroxyl chemistry regulation for iodine cathode. a, UV-Vis absorption spectra of cellulose/polyiodide mixed solutions after high-temperature aging (inset: optical photographs showing color differences). **b,** O 1*s* XPS spectra of CNF and ONF cellulose papers before and after polyiodide adsorption. **c-e,** In situ UV-Vis spectra during charge/discharge for PVDF-, CNF- and ONF-based cathodes. **f,** In situ Raman spectra and corresponding galvanostatic charge/discharge curves for PVDF-, CNF- and ONF-based cathodes. **g,** Binding energies of PVDF, CNF and ONF with I_3^- and I_5^-. **h,** Gibbs free energy profiles for iodine species reactions under PVDF, CNF and ONF influence. **i,** DRT contour maps comparing PVDF-, CNF- and ONF-based cathodes.

Reviewer #4:

"This manuscript, entitled "Hydroxyl Chemistry Regulation of Cellulose Biopolymers for Aqueous Battery Binders", reports a hydroxyl-chemistry regulation strategy for cellulose biopolymers aimed at overcoming the chemical and interfacial limitations of current binder systems in aqueous zinc batteries. Specifically, the authors employ a periodate-borohydride selective disruption of the cyclic conformation of AGUs in the cellulose backbone to redistribute the electron cloud, enhance the dipole moment, and increase the reactivity of hydroxyl groups. This modification is proposed to unlock their capacity to regulate interfacial reactions and stabilise electrode architectures. As a result, the ONF binder, when applied in Zn-I_2 batteries, is reported to deliver a high-rate capability of 150.9 mAh g^{-1} at 20 A g^{-1} and an exceptional capacity retention of 98.07% over 3000 h in a practical pouch cell. Similarly, the incorporation of ONF into Zn-V_2O_5 batteries is claimed to significantly enhance electrochemical performance. However, despite these promising outcomes, the manuscript still exhibits substantial shortcomings in terms of scientific originality, data robustness, and mechanistic justification. It does not yet meet the publication standards of Nature Communications. My specific comments are as follows:"

Reply to the Reviewer:

Thank you very much for your recognition of the research value of this paper and for providing valuable and rigorous feedback. Based on your insightful suggestions, we have focused on enhancing and deepening the scientific originality, data robustness, and completeness of the mechanistic validation in this revised version.

Q1. *"The authors apply the ONF binder to both Zn-I_2 and Zn-V_2O_5 battery systems. The failure mechanisms of these two cathodes are, however, fundamentally different. The authors are requested to clearly explain how the degradation pathways differ between the two systems."*

Reply to the Reviewer:

We sincerely appreciate your insightful comments and agree that the failure mechanisms of cathodes in Zn-I_2 and Zn-V_2O_5 batteries are fundamentally different. Below, we clarify these distinctions and explain how the ONF binder mitigates degradation in both systems by regulating **electrode-level interfacial processes**, rather than altering the intrinsic cathode chemistry.

1. Distinct failure mechanisms in the two cathodes

a. **Capacity fading in iodine cathode** primarily stems from the dissolution and shuttle effect of polyiodides (e.g., I_3^-). During discharge, I^- generated from the reduction of I_2 combines with unreacted I_2 to form soluble I_3^-, which readily diffuses into the electrolyte and migrates across the separator to the zinc anode, causing irreversible loss of active iodine and chemical corrosion of the zinc metal. This leads to irreversible iodine loss, parasitic reactions at the Zn surface, and continuous capacity decay (*Energy Environ. Sci.*, 2023,16, 4872-4925). Consequently, effective **physical confinement of polyiodides**, **chemical anchoring at the cathode interface**, and **rapid redox conversion kinetics** are critical to suppress shuttling and stabilize iodine cathodes.

b. Capacity fading in V_2O_5 cathode is mainly attributed to the dissolution of vanadium species coupled with structural degradation of the active material. Hydronium ions in the electrolyte attack V-O bonds, promoting the dissolution of vanadium as VO^{2+} and other forms, which then migrate to the zinc anode and destabilize the interface. Simultaneously, repeated charge carriers insertion/extraction induces lattice strain, leading to progressive structural collapse of V_2O_5 (*Angew. Chem. Int. Ed.*, 2025, 64, e202510638). Hence, the failure of this system is essentially due to **elemental dissolution and structural decay of the active material**. Thus, suppressing **vanadium dissolution**, maintaining **structural integrity**, and preserving **efficient charge-transfer kinetics** are essential to mitigate capacity fading in this system.

Although the failure pathways differ between these two systems, both systems **share a common electrode-level challenge: loss of active material from the cathode and insufficient redox kinetics**. The ONF binder addresses this shared bottleneck through synergistic multifunctional effects (Fig. R2):

2. Mechanism by which ONF alleviates system failure

I. Formation of a high-coverage, electronically continuous electrode architecture

The dense hydrogen-bonding network of ONF enables the formation of a thin, continuous, and conformal coating on active materials, ensuring intimate contact among active particles and conductive additives. This architecture suppresses electrical discontinuities that commonly arise during cycling, thereby establishing continuous electronic and ionic migration pathways throughout the electrode thickness. As a result, charge carriers can be rapidly delivered to reaction sites, directly enhancing redox kinetics in both Zn-I_2 and Zn-V_2O_5 cathodes.

II. Suppression of active-material dissolution and shuttle processes

In Zn-I_2 system, the high density of polar hydroxyl groups on ONF forms strong hydrogen-bond and dipole interactions with polyiodides, reducing their desorption and diffusion into the electrolyte. In parallel, the dense coating prolongs diffusion pathways, increasing the probability that polyiodides undergo rapid electrochemical reconversion rather than shuttling. In Zn-V_2O_5 system, the ONF coating acts as a dynamically stable interfacial barrier that selectively allows Zn^{2+} transport while mitigating direct hydronium attack on V-O bonds, thereby slowing vanadium dissolution.

III. Enhancement of redox kinetics and mitigation of polarization

Beyond confinement and stabilization, ONF significantly improves redox kinetics by maintaining electrode-scale charge-transport continuity. The compact coating shortens electron-transport distances, while the hydrogen-bond-mediated ion-transport network reduces concentration polarization. Consequently, both systems exhibit lower polarization, faster reaction kinetics, and improved rate capability, as reflected in CV, GITT/DRT, and pseudocapacitive analyses.

IV. Preservation of electrode structural integrity

The reinforced hydrogen-bonding network of ONF imparts high flexibility and mechanical robustness to the electrode. During repeated iodine conversion or Zn^{2+} insertion/extraction, ONF

tightly binds active particles and conductive components, preventing contact loss and structural disintegration commonly observed with conventional binders.

Therefore, ONF does not rely on a cathode-specific chemical reaction. Instead, through the integrated functions of **dense electrode coverage, chemical anchoring, continuous charge-migration pathways, and mechanical reinforcement**, it targets the shared electrode-level origin of failure: active-material loss and sluggish reaction kinetic at the cathode interface. This multifunctional regulation enables ONF to deliver outstanding performance in both **shuttle-dominated Zn-I_2 batteries** and **dissolution/structure-decay-dominated Zn-V_2O_5 batteries**, demonstrating its universal value as a high-performance binder for aqueous zinc-based cathodes.

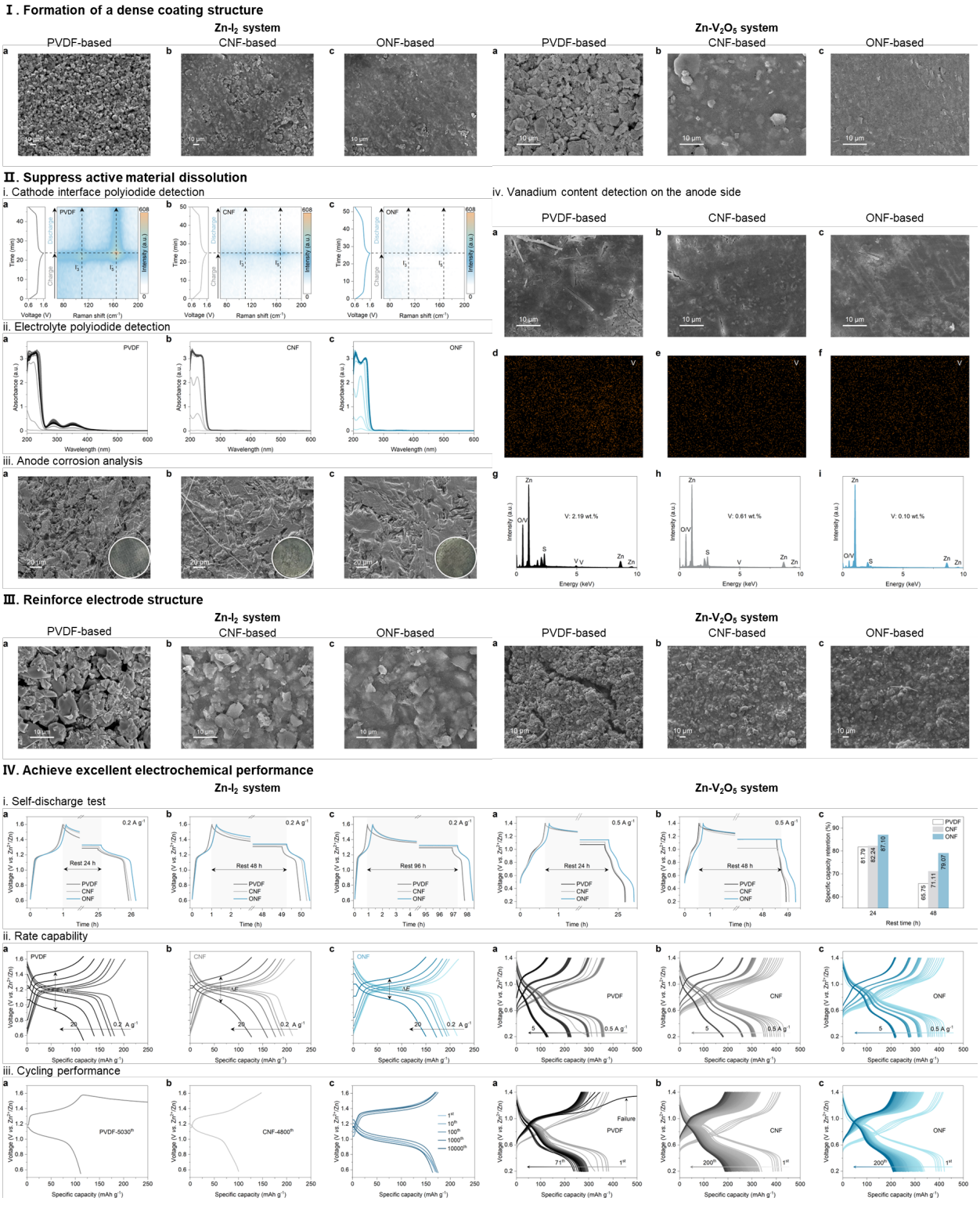

Fig. R2. Functions of the ONF binder and its outstanding electrochemical performance in both systems.

We have further clarified the above comparisons and explanations in the revised manuscript to present the logic of ONF's action under different failure mechanisms more clearly. We appreciate the reviewer's comments, which have helped deepen the mechanistic interpretation of our work.

Revised:

(Page 19, lines 403-405)

Taken together, the ONF binder consistently promotes uniform electrode morphology, ensures efficient ion/electron conduction, and effectively regulates soluble active species through confinement and conversion at the electrode level (Fig. 6k, Supporting Note 8), enabling aqueous batteries with improved cycling stability across different cathode chemistries.

(Supplementary Page 36-37)

Supplementary Note 8

The ONF binder developed in this work leverages its unique strong hydrogen-bonding network and dense encapsulation capability toward active particles to differentially address the distinct degradation pathways in the two systems (Zn-I_2, Zn-V_2O_5), thereby simultaneously enhancing the discharge specific capacity and cycling stability of both types of batteries while effectively reducing system polarization (Fig. 4 and Supplementary Figs. 52, 53), highlighting its universal applicability.

Specifically, the main failure mechanism of Zn-I_2 battery cathode stems from the shuttle effect of polyiodides and the gradual structural loosening of the electrode. The soluble polyiodide ions generated during charge-discharge cycles tend to diffuse into the electrolyte and migrate to the anode, forming a shuttle cycle (Supplementary Fig. 42, left) that leads to active material loss and Coulombic efficiency decay. ONF forms a dense coating layer around the iodine host (Fig. 3d-f), which not only maintains the structural integrity of the electrode but also serves as a physical barrier to suppress polyiodide dissolution. Meanwhile, the abundant surface hydroxyl groups can chemically adsorb and anchor polyiodides, confining them to the cathode side (Fig. 5a, b, g). Furthermore, ONF exhibits a certain catalytic effect on the redox reactions of iodine species (Fig. 4c, Fig. 5h), shortening the lifetime of highly soluble intermediates (Fig. 5c-f). Therefore, ONF can fundamentally suppress the shuttle effect through a “confinement-anchoring-conversion” strategy.

In the case of the Zn-V_2O_5 battery, cathode failure primarily originates from the inherent structural instability of V_2O_5, where repeated Zn^{2+} insertion/extraction can lead to crystal-structure collapse accompanied by vanadium dissolution. Dissolved vanadium species can migrate to the Zn anode and damage the anode interface. Here, ONF functions mainly as structural reinforcement and interfacial isolation (Supplementary Figs. 49-51). The dense coating layer alleviates volume-expansion stress during cycling and reduces direct contact between V_2O_5 and the electrolyte, thereby suppressing vanadium dissolution. In addition, the hydrogen-bonding network of ONF can partially capture migrating vanadium species, reducing their deposition on the Zn anode. As a result, the vanadium content on the Zn anode decreases to 0.10 wt.% when ONF is used as the binder (Supplementary Fig. 55). Consistently, ONF-based Zn-V_2O_5 batteries exhibit improved self-discharge behavior, retaining 87.10% and 79.07% of their initial capacity after 24 h and 48 h of rest, respectively (Supplementary Fig. 54).

While the degradation mechanisms of Zn-I_2 and Zn-V_2O_5 systems are fundamentally different, ONF does not rely on a single chemistry-specific reaction. Instead, as a multifunctional binder, ONF provides robust physical confinement, interfacial stabilization, and enhanced charge-transport continuity, which effectively mitigate the dominant degradation pathways in each system.

Q2. *"The authors should provide a complete and detailed description of the calculation method used for the activation energy barriers shown in Figure 4c. It is currently unclear how these values were obtained."*

Reply to the Reviewer:

We sincerely thank you for your valuable remark. Based on the literature (*Adv. Funct. Mater.*, 2024, 34, 2409099), the detailed procedure is as follows: the rising segment (from the equilibrium potential toward the peak potential) of the targeted oxidation/reduction peak in the CV curve is selected, and the corresponding potential-current density data are extracted. A linear fit is then performed between the potential and log (current density) to obtain the slope b, which is substituted into the equation:

$$E_{\text{Red/Ox}}=E^{0}_{\text{Red/Ox}}-\frac{\text{RT}}{b}\varphi_{\text{cathode}}(\text{Ox/Red})_{\text{IR}} \quad (1)$$

where $E_{\text{Red/Ox}}$ is the activation energy of the oxidation or reduction process, $E^{0}_{\text{Red/Ox}}$ is the intrinsic activation energy, R is the gas constant, φ_{cathode} is the irreversible potential during the oxidation or reduction process.

Revised:

(Page 11, lines 236-237)

The energy barriers analysis (Fig. 4c, Supplementary Note 3 and Supplementary Fig. 25) further supported this conclusion, showing that the ONF-based cathode exhibited the lowest kinetic barriers for both I_2 reduction and I^- oxidation, with activation energy reductions of 4.58 and 2.09 kJ mol^{-1}, respectively.

(Page 23, lines 512-516)

The variation in reaction energy barrier (kJ mol^{-1}) was calculated using Equation (4) [53].

$$E_{\text{Red/Ox}}=E^{0}_{\text{Red/Ox}}-\frac{\text{RT}}{b}\varphi_{\text{cathode}}(\text{Ox/Red})_{\text{IR}} \quad (4)$$

where $E_{\text{Red/Ox}}$ is the activation energy of the oxidation or reduction process, $E^{0}_{\text{Red/Ox}}$ is the intrinsic activation energy, R is the gas constant, φ_{cathode} is the irreversible potential during the oxidation or reduction process.

(Supplementary Page 19)

Supplementary Note 3

The rising segment (from the equilibrium potential toward the peak potential) of the targeted oxidation/reduction peak in the CV curve is selected, and the corresponding potential-current density data are extracted (Supplementary Fig. 25). A linear fit is then performed between the potential and log (current density) to obtain the slope b, which is substituted into the Equation (4) to calculate the variation in the reaction energy barrier.

(Supplementary Page 19)

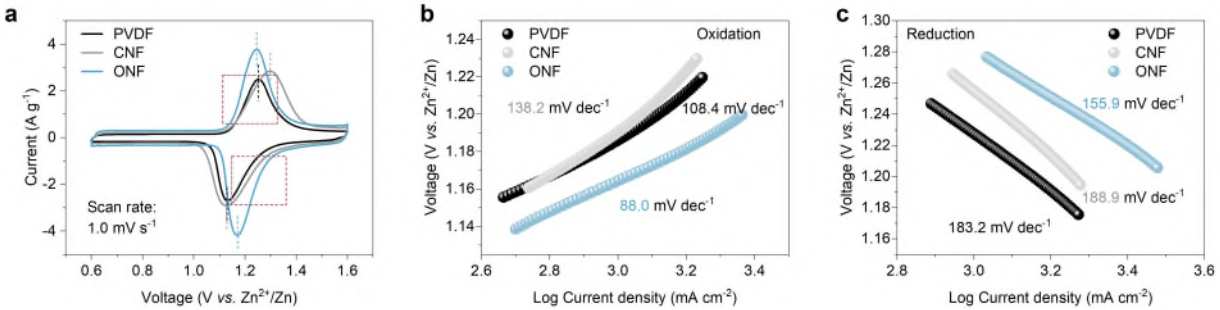

Supplementary Fig. 25. a, CV profiles of PVDF-, CNF-, and ONF-based cathodes at 1.0 mV s^{-1}, and comparative analysis of fitted slopes for **b,** oxidation and **c,** reduction peaks.

Q3. *"The manuscript states: "Tafel slope analysis (Supplementary Fig. S18) further supported this conclusion…". However, Supplementary Fig. S18 does not present Tafel plots but rather CV-derived rate data. The authors should correct this description and carefully check the entire manuscript for similar inconsistencies."*

Reply to the Reviewer:

Thank you very much for carefully pointing out the inaccuracy between the description and the content of the supplementary figure. We have corrected the relevant description accordingly. Following your suggestion, we have also thoroughly reviewed the entire manuscript (including the main text, figure captions, and supplementary materials) to ensure that no similar or other inconsistencies remain. We sincerely apologize for this oversight and greatly appreciate your rigorous review.

Revised:

(Page 11, lines 236-237)

The energy barriers analysis (Fig. 4c, Supplementary Note 3 and Supplementary Fig. 25) further supported this conclusion, showing that the ONF-based cathode exhibited the lowest kinetic barriers for both I_2 reduction and I^- oxidation, with activation energy reductions of 4.58 and 2.09 kJ mol^{-1}, respectively.

Q4. *"The interpretation of the GITT curves in Figure 4d is problematic. The data clearly correspond to a Zn-I_2 full cell, yet Zn^{2+} does not participate in the cathodic redox processes. The cathode involves only iodine species, and thus GITT cannot be used to infer Zn^{2+} diffusion. Moreover, iodine undergoes conversion reactions, and the associated kinetics are not governed by the diffusion properties of the binder. The authors should clarify what specific information the GITT analysis is intended to convey."*

Reply to the Reviewer:

We sincerely thank you for this careful and technically important comment. We fully agree that, in a Zn-I_2 full cell, Zn^{2+} do not participate directly in the cathodic Faradaic redox reactions, which are governed by iodine species. Accordingly, GITT cannot be used to extract a true Zn^{2+} diffusion coefficient in the iodine cathode, nor to describe intrinsic solid-state diffusion in the conventional sense. In this work, the purpose of the GITT analysis is not to deconvolute individual ionic diffusion processes or to quantify Zn^{2+} transport within the binder. Instead, GITT is employed as a diagnostic tool to evaluate the overall polarization behavior and apparent reaction kinetics of the full cathode system under near-equilibrium perturbations, which is a widely adopted practice for conversion-type and multi-step electrochemical systems where classical diffusion models are not applicable (*Angew. Chem. Int. Ed.*, 2025, 64, e202506822. *Energy Storage Mater.*, 2025, 75, 103993. *Nano-Micro Lett.*, 2023, 15, 126. *Adv. Mater.*, 2026, 38, e11680. *Adv. Mater.*, 2026, 38, e15000).

Although the main redox reaction at the cathode involves iodine species, the actual reaction rate and overpotential in a full cell are governed by several series steps, including: the charge-transfer process corresponding to the iodine redox reaction; mass transport of iodine species within the electrolyte/iodine host pores; and the migration of counter-ions (Zn^{2+}) at the electrode/electrolyte interface. While Zn^{2+} does not directly participate in the cathodic redox chemistry, its interfacial transport affects concentration polarization and thus indirectly impacts the effective kinetics of iodine conversion. By forming a continuous, hydrogen-bonded ion-conduction framework and a stable electrode/electrolyte interface, the ONF binder mitigates polarization buildup and facilitates more uniform reaction progression. This manifests experimentally as shorter relaxation times and reduced voltage hysteresis in GITT, consistent with the enhanced rate capability and cycling stability observed elsewhere in the manuscript.

Following the reviewer's suggestion, we have revised the manuscript to explicitly clarify the intent and limitation of the GITT analysis, avoiding any implication that it represents a Zn^{2+} diffusion coefficient or intrinsic binder-controlled diffusion process.

Revised:

(Pages 11-12, lines 241-249)

Galvanostatic intermittent titration technique (GITT) measurements (Fig. 4d, Supplementary Fig. 26 and Supplementary Table 3) were used to evaluate the overall polarization behavior and apparent reaction kinetics of the iodine cathode. The reduced voltage relaxation and smaller polarization in the ONF-based system indicate faster redox equilibration and lower internal resistance, demonstrating that the ONF binder effectively mitigates concentration polarization and facilitates rapid iodine redox conversion [43-45].

(Page 21, lines 467-468)

The galvanostatic intermittent titration technique (GITT) was utilized to evaluate the overall reaction kinetics and polarization behavior of the electrodes.

(Page 23, lines 517-520)

The polarization resistance (R_{int}, k Ω) was calculated using Equation (5) [35]:

$$R_{int}=\frac{|V_{QOCV}-V_{CCV}|}{I_a} \quad (5)$$

where $|V_{QOCV}-V_{CCV}|$ is the voltage gap between the quasi-open circuit voltage and closed-circuit voltage during each GITT step, and I_a is the applied current.

(Supplementary Page 41)

Supplementary Table 3. Range of R_{int}-values and D-values during charge/discharge processes in zinc-iodine batteries with different binder systems.

System	R_{int}-charge (k Ω)	D-charge ($\times10^{-10}$ cm^2 s^{-1})	R_{int}-discharge (k Ω)	D-discharge ($\times10^{-10}$ cm^2 s^{-1})
PVDF-based	0.2909-4.6654	0.6681-2.7518	0.0800-8.8254	2.0262-12.2051
CNF-based	0.1985-2.3474	0.8988-11.1279	0.0993-2.1762	7.6373-14.1112
ONF-based	0.1520-1.8413	1.1320-17.2617	0.0671-1.8058	7.8748-24.3069

Q5. *"The binding energy calculations in Figure 5d inherently involve interactions between anionic species. In such systems, the basis functions of molecules A and B overlap within the AB complex, artificially lowering the computed E(AB). Have the authors applied Basis Set Superposition Error (BSSE) corrections in their calculations?"*

Reply to the Reviewer:

We sincerely appreciate your insightful comments regarding the necessity of basis set superposition error (BSSE) correction in the calculation of adsorption energies, with which we fully agree. It should be noted, however, that BSSE arises primarily from the use of incomplete and non-orthogonal atom-centered basis sets, such as Gaussian-type orbitals commonly employed in Gaussian software. When the adsorbate and substrate approach each other, their basis functions overlap, leading to an underestimation of the total energy of the adsorbate-substrate complex due to the mutual "borrowing" of basis functions. In this work, all calculations were performed using the VASP package, which employs a plane-wave basis set. When the plane-wave cutoff energy is sufficiently high, the basis set becomes orthogonal and nearly complete, and the associated error stems mainly from the cutoff choice rather than from basis function overlap.

To minimize any basis-set-related errors, we adopted a high plane-wave cutoff energy of 450 eV, which exceeds the recommended cutoff values for all elements in the system and ensures adequate completeness of the basis set. In addition, a sufficiently thick vacuum layer was introduced in the periodic slab models to eliminate spurious interactions between periodic images, thereby avoiding additional artificial stabilization effects.. These settings-high cutoff energy and thick vacuum layer-

are consistent with standard practices in contemporary literature on surface adsorption within the aqueous zinc-iodine battery field (*Angew. Chem. Int. Ed.*, 2024, 63, e202403187; *J. Am. Chem. Soc.*, 2024, 146(24), 16601-16608; *Adv. Funct. Mater.*, 2025, 35, 2422081; *Adv. Mater.*, 2024, 36, 2312246). As a result, the influence of BSSE on the adsorption energies reported in this study is expected to be negligible compared with calculations based on atom-centered basis sets.

Q6. *"In Figure 5e, the Gibbs free-energy profiles for the CNF system are missing. The authors should clarify why CNF was not included in this comparison."*

Reply to the Reviewer:

We have conducted and now supplemented the Gibbs free energy curves for the CNF-based system into updated Fig. 5h. It is found that complementary Gibbs free energy calculations of the I_2 reduction pathway demonstrated that while the conversion of I_2 to I^- ($\Delta G < 0$) is thermodynamically favorable in all three systems, ONF further reduced the overall reaction free energy, suggesting that it facilitates faster reaction kinetics by lowering the activation barriers associated with polyiodide redox transitions.

Revised:

(Page 16, lines 319-320)

Complementary Gibbs free energy calculations of the I_2 reduction pathway (Fig. 5h) demonstrated that while the conversion of I_2 to I^- ($\Delta G < 0$) is thermodynamically favorable in all three systems.

(Page 15, line 307)

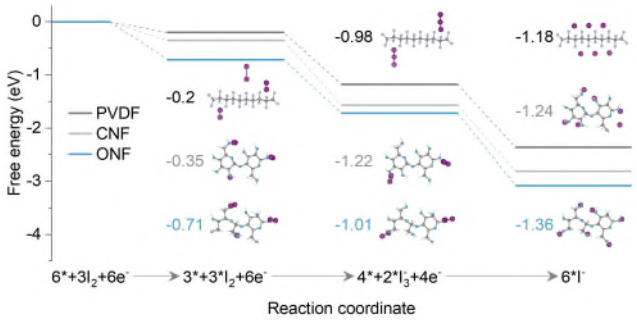

Fig. 5 | h, Gibbs free energy profiles for iodine species reactions under PVDF, CNF and ONF influence.

Q7. *"In the DRT analysis shown in Figure 5g, peaks P3 and P5 are attributed to Zn^{2+} transport resistance. Given the aqueous environment, why would Zn^{2+} transport dominate over H^+ movement? Furthermore, are these resistive features related to the conversion of polyiodide species? The authors should provide a more robust justification."*

Reply to the Reviewer:

We sincerely thank you for this insightful comment, which allows us to clarify the physical meaning of the DRT features and their relevance to the iodine redox process. In this work, a 2 M $ZnSO_4$ aqueous electrolyte (pH = 4~5) was employed. Under these conditions, the concentration of free protons (H^+) does not exceed ~10^{-4} M, which is several orders of magnitude lower than that of Zn^{2+} (2 M). Although H^+ ions possess higher intrinsic mobility, their lower concentration means that their contribution to the overall ionic flux and impedance response can be negligible compared with that of Zn^{2+}, which is the dominant charge carrier in the electrolyte. Therefore, the resistive features observed in the DRT spectra primarily reflect Zn^{2+} transport-related processes rather than proton migration.

It should be clarified that the Zn^{2+} transport impedance reflected in the DRT is indirectly related, rather than directly corresponding, to the conversion process of iodine species. Specifically, the redox reaction at the iodine cathode in Zn-I_2 batteries involves the interconversion of iodine species. For instance, during discharge, I_2 combines with I^- to form I_3^-, which is subsequently reduced to I^- via electron transfer, the reverse process occurs during charging to regenerate I_2. This process not only relies on the migration of iodine species but also requires the participation of Zn^{2+} for interfacial charge balance and mass transport. Zn^{2+} can form charged complexes with polyiodide ions (such as $[Zn{\cdot}I{\cdot}5H_2O]^+$, *Energy Environ. Sci.*, 2025,18, 3160-3168. $[Zn{\cdot}I_3{\cdot}5H_2O]^+$, *Nat. Commun.*, 2015, 6, 6303), thereby influencing the migration of iodine species and the charge matching at reaction sites.

Following hydroxyl chemistry regulation, the ONF binder constructs continuous ion-transport pathways via a dense hydrogen-bond network, which significantly reduces Zn^{2+} migration resistance on the cathode side, as reflected by the suppressed P3 and P5 peaks in the DRT analysis. This improved Zn^{2+} transport enables rapid replenishment of the reaction interface, mitigates ion concentration gradients, and accelerates the electron-transfer kinetics of iodine species. As a result, polyiodide conversion proceeds in a more continuous, uniform, and reversible manner, consistent with the reduced polarization and enhanced rate capability observed experimentally.

Q8. *"The manuscript lacks validation using ampere-hour-level pouch cells, which would be essential for demonstrating the practical applicability of the proposed binder system. The authors are encouraged to include large-format cell data."*

Reply to the Reviewer:

Thank you very much for your suggestion. By preparing thicker iodine cathodes and integrating multiple cathodes onto a single current collector, we successfully fabricated a larger-format soft-pouch battery, achieving capacity delivery at a capacity of 0.17 Ah.

Revised:

(Page 17, lines 370-373)

Using this method, we fabricated a four-layer ONF-based cathode with an active mass loading of 16 mg cm^{-2} (Fig. 6g and Supplementary Fig. 46), which exhibited stable cycling performance over 500 cycles at 1 A g^{-1}. Furthermore, a self-supporting iodine cathode (400 μm) was also fabricated via a one-step vacuum filtration process (Supplementary Fig. 47) [49,52]. By integrating multiple uniformly sized high loading iodine cathodes onto a single current collector, a larger-format pouch cell with a steady discharge capacity of 0.17 Ah was fabricated (Supplementary Fig. 48). These results demonstrate the scalability and practical utility of the ONF binder in constructing thick electrodes with high mechanical integrity and continuous ion/electron transport pathways across the thickness direction.

(Supplementary Page 30)

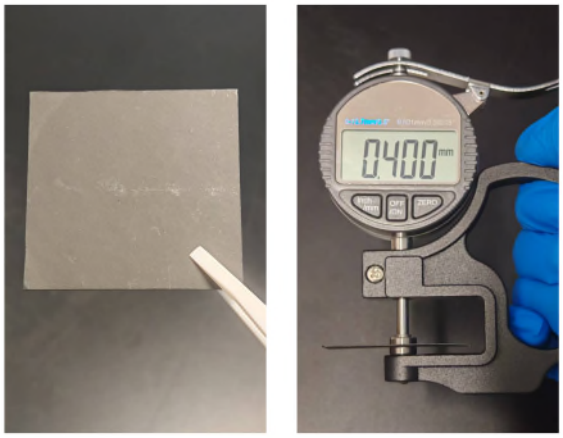

Supplementary Fig. 47. Optical photograph (left) and thickness (right) of ONF-based high-loading iodine cathodes prepared by the one-step method.

(Supplementary Page 30)

Supplementary Fig. 48. a, Schematic diagram, optical photograph, and corresponding **b,** electrochemical performance of the pouch cell with ONF-based high-loading iodine cathodes.

Q9. *"A substantial body of literature has already reported the use of cellulose and cellulose derivatives as binders for aqueous zinc-ion batteries. Consequently, the novelty of the present work is questionable. Relevant examples include: Advanced Materials (2025, 37, 2412908), Nano Energy (2024, 120, 109094), and Nano Energy (2025, 133, 110519). The authors should clearly articulate how their approach differs from, and advances beyond, these prior reports."*

Reply to the Reviewer:

We sincerely thank you for the careful assessment and for raising the important question regarding the novelty of this work. The cited studies indeed represent valuable and influential advances in the application of cellulose and cellulose derivatives in aqueous zinc-based batteries. We have carefully analyzed these reports in detail. While we fully acknowledge that cellulose-based binders constitute an active and rapidly developing research area, we believe that **the present work differs fundamentally from, and advances beyond, these prior studies in material design philosophy, mechanistic depth, and performance level**, as briefly outlined below.

Ref. 1: Adv. Mater., 2025, 37, 2412908. (Review on the applications of bacterial cellulose in electrochemical energy storage devices)

Abstract

Bacterial cellulose (BC) is produced via the fermentation of various microorganisms. It has an interconnected 3D porous network structure, strong water-locking ability, high mechanical strength, chemical stability, anti-shrinkage properties, renewability, biodegradability, and a low cost. BC-based materials and their derivatives have been utilized to fabricate advanced functional materials for electrochemical energy storage devices and flexible electronics. This review summarizes recent progress in the development of BC-related functional materials for electrochemical energy storage devices. The origin, components, and microstructure of BC are discussed, followed by the advantages of using BC in energy storage applications. Then, BC-related material design strategies in terms of solid electrolytes, binders, and separators, as well as BC-derived carbon nanofibers for electroactive materials are discussed. Finally, a short conclusion and outlook regarding current challenges and future research opportunities related to BC-based advanced functional materials for next-generation energy storage devices suggestions are proposed.

[Figure Redacted]

Adapted Fig. 1. a, Schematic illustrations depicting the preparation of BC with hierarchical cellulose structure from microorganisms. **b,** Application of BC related materials toward electrolyte, binder, separator, and BC-derived electrode host.

This study (Ref. 1) demonstrates that bacterial cellulose (BC) can serve as a high-performance, biodegradable, green binder owing to its flexibility, abundant hydroxyl groups, and three-dimensional network structure. It enables the construction of high-loading flexible electrodes, enhances electrode integrity through hydrogen-bond interactions, and facilitates ion transport. Compared to traditional PVDF binders, BC offers superior environmental compatibility and structural adaptability. However, **current research still exhibits notable shortcomings: the working mechanisms and structure-property relationships of BC are insufficiently understood**; conventional chemical modification approaches are polluting and difficult to scale, necessitating the development of green functionalization strategies such as in-situ microbial fermentation; **precise control over the microstructure and surface groups of BC remains challenging**, with uniformity control being a bottleneck; its insulating nature restricts electron conduction, requiring conductive integration strategies; furthermore, interfacial side reactions between BC and metal electrodes, along with performance optimization of electrolytes (e.g., wide-temperature operation, flame retardancy), represent critical issues that need to be addressed.

Ref. 2: Nano Energy, 2024, 120, 109094. (Aqueous $ZnSO_4$ electrolyte additive)

Abstract

The development of aqueous zinc-ion batteries (ZIBs) as attractive candidates is largely limited by the unstable anode/electrolyte interface (AEI), which causes dendrite formation and by-products. Here, an inexpensive ionic cellulose adhesive, carboxymethylcellulose sodium (CMC), is utilized as an interface stabilizer to controllably manipulate the AEI for reversible Zn plating/stripping behaviors. The CMC derived anions have a propensity to initially gather on the Zn surface, forming a unique H_2O-poor and CMC-rich electrical double layer (EDL) for relieving the water-induced side reactions and promoting fast Zn^{2+} transport kinetics. Meanwhile, an adaptive solid electrolyte interphase (SEI) can be triggered during cycling to further tune interfacial Zn^{2+} deposition behaviors. Such a combination enables exposure of (002) facets with dendrite-free and compact Zn deposition on Zn metal. Accordingly, the Zn//Zn symmetric cells

with CMC-based electrolyte achieve outstanding lifespan with a 26-fold enhancement for 3125 h at 1 mA cm^{-2} and 1 mAh cm^{-2}. Also, the Zn anode is promoted to run over 4000 cycles with high Zn reversibility of 99.7%. When paired with $NaV_3O_8 \cdot 1.5\ H_2O$ (NVO) cathode, the full cell with CMC achieves a prominent stability for 2500 cycles at 3 A g^{-1}, much better than that in pure $ZnSO_4$ electrolyte.

[Figure Redacted]

Adapted Fig. 2. Schematic illustrations showing mechanism of Zn deposition.

This study (Ref. 2) does not employ cellulose-based materials as binders, but rather uses carboxymethyl cellulose sodium (CMC) **as an additive in aqueous $ZnSO_4$ electrolyte** to stabilize the zinc-metal anode interface and suppress dendrite growth. The core mechanism lies in the preferential adsorption of CMC anions onto the zinc anode surface, forming an electric double-layer structure characterized by "water-lean, CMC-rich" properties. This effectively displaces interfacial water molecules, thereby significantly suppressing side reactions such as corrosion and hydrogen evolution, while promoting Zn^{2+} desolvation and fast transport. During cycling, a portion of the adsorbed CMC anions undergo reductive decomposition, forming an in situ solid electrolyte interphase composed of organic-inorganic components. This stable SEI further regulates Zn^{2+} deposition behavior, guiding dense and uniform zinc plating along the (002) crystal plane, thereby fundamentally preventing dendrite formation. **Consequently, aside from the use of cellulose-derived species, this work is fundamentally distinct from the present study in terms of material role, target interface, and mechanistic focus**.

Ref. 3: Nano Energy, 2025, 133, 110519. (Iodine cathode binder)

Abstract

Designing functional binders is demonstrated an effective solution to address the serious issues of active iodine dissolution and polyiodide shuttle faced by aqueous zinc-iodine batteries (AZIBs). Herein, a series of linear-chain polysaccharides are systematically investigated as the potential water-soluble binders for iodine-loading cathode of AZIBs. According to the results of spectral characterizations and theoretical calculations, SA binder, as the representative of polysaccharides, is verified with strong chemisorption capability and high binding energy for the iodine intermediates owing to the existence of active ether and carboxyl groups, which contributes to suppress the polyiodide shuttle and active iodine dissolution. Meanwhile, the lower Gibbs free energy values indicate the introduction of SA binder is conducive to boost the iodine redox reaction kinetics of iodine-loading cathode. Benefitting from these merits, the Zn//CAC@I_2 batteries with SA biner delivers superior self-discharge resistance capability, excellent rate

performance, and ultra-durable cycling stability with high reversible capacity of 105.2 mAh g^{-1} after 8000 cycles at 1 A g^{-1} and 86.3 mAh g^{-1} after 40,000 cycles at 5 A g^{-1}, respectively. This work will enlighten the research and development of binder materials for advanced iodine-based energy storage devices, and facilitate the practical application of both polysaccharide binders and AZIBs.

[Figure Redacted]

Adapted Fig. 3. Schematic illustration of action mechanism of **a,** SA and **b,** PTFE binders on the iodine-loading cathode and zinc metal anode of AZIBs.

This work (Ref. 3) addresses the challenges of active iodine dissolution and polyiodide shuttling in aqueous zinc-iodine batteries by proposing linear-chain polysaccharide binders (exemplified by sodium alginate, SA) as a solution. The mechanism is primarily based on chemical adsorption of iodine species by ether and carboxyl functional groups on the polysaccharide chains. This adsorption suppresses polyiodide migration and lowers the Gibbs free energy barrier for iodine redox reactions, leading to improved cycling stability and rate performance. Nevertheless, the mechanism in Ref. 3 is mainly **limited to** functional-group-based chemical adsorption, **without establishing a molecular-structure-to-electrode-architecture relationship or demonstrating how conformational regulation of biopolymer chains governs** polyiodide confinement, charge transport, and long-term electrode stability.

Our work (Hydroxyl Chemistry Regulation of Cellulose Biopolymers for Aqueous Battery Binders)

Abstract

Aqueous batteries offer inherent safety and low cost, but the inherently fixed physicochemical functionality and poor interfacial compatibility of existing binders limit their ability to boost cathode performance. Here we present a hydroxyl-chemistry regulation strategy that transforms cellulose, the most abundant biopolymer on Earth, into a high-affinity, interracially compatible binder that stabilizes high-capacity, shuttling-prone cathodes. By selectively opening the rigid cellulose ring structure within its molecular chains, we enhance dipole polarity, chain flexibility, and intermolecular hydrogen-bond density, thereby increasing functional-group accessibility and interfacial adhesion. These molecular-level modifications drive the formation of a dense nanofibrous network that conformally encapsulates active particles and strongly anchors polyiodides, accelerating redox kinetics and reinforcing electrode stability. Iodine cathodes incorporating the engineered binder deliver a reversible capacity of 150.9 mAh g^{-1} at 20 A g^{-1},

with pouch cells retaining 98.07% capacity after 3000 h. The binder also enables layer-by-layer fabrication of high mass loading electrodes, and benefits other dissolution-prone cathodes such as V_2O_5. Overall, this work establishes a general and sustainable route for the molecular engineering of biopolymer binders, expanding their role in the design of advanced aqueous batteries.

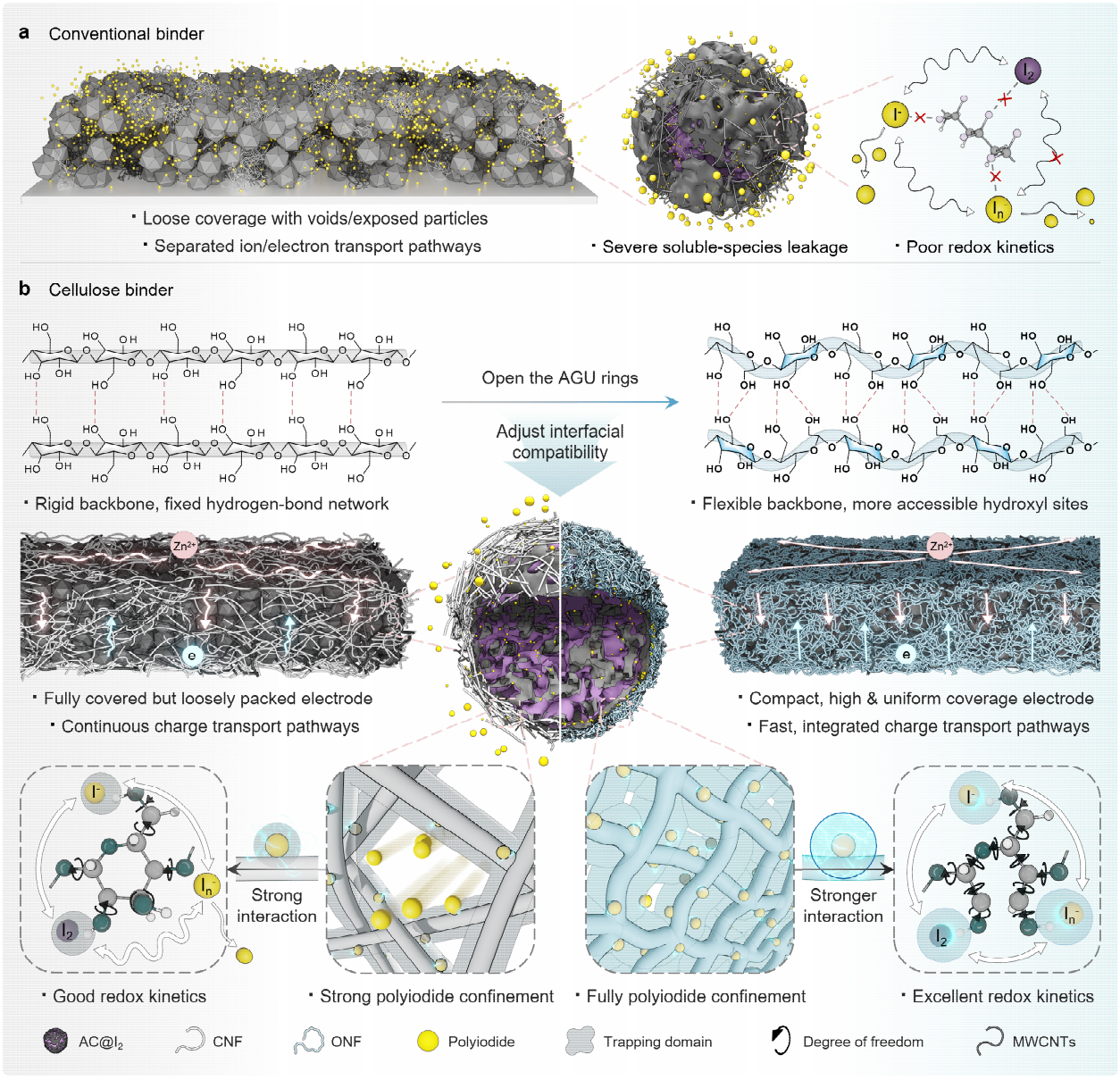

Fig. 1. Schematic comparison of binder performance in aqueous batteries (exemplified by the iodine cathode). **a,** Conventional binder. **b,** Cellulose binder before (left) and after (right) hydroxyl chemistry regulation.

In our work, we propose **a universal strategy based on "hydroxyl chemistry" regulation to address the failure of electrochemical energy storage devices caused by uncontrolled migration of dissolved active species**, such as iodine shuttle and vanadium dissolution. Through precise molecular engineering— C2-C3 bond cleavage of cellulose—we trigger a cascade of optimizations spanning molecular structure, interchain interactions, and macroscopic assembly morphology, with **the core achievement being the construction of a reinforced hydrogen-bond network**. This

network ultimately manifests as a unique, high-strength, dense coating structure, enabling a synergistic “physical-chemical” mechanism that simultaneously accomplishes: effective anchoring of active species, strong suppression of detrimental shuttling, optimization of charge transport, and long-term stabilization of the electrode architecture. The clear “structure-property-performance” relationship chain presented in this work not only fundamentally explains why ONF functions as a super-binder to deliver outstanding electrochemical performance, but also provides solid theoretical and practical foundations for the rational design of next-generation high-performance battery interface materials through deliberate regulation of hydrogen-bond chemistry.

To illustrate the originality of our current work, we summarize the major differences between our work and the works (Adv. Mater., 2025, 37, 2412908; Nano Energy, 2024, 120, 109094; Nano Energy, 2025, 133, 110519.) cited by the reviewer, as shown below.

1. **Precisely chemically engineered binders at the molecular structure level (Our work) *vs.* Screening and utilizing commercially available or naturally occurring polysaccharide materials (Adv. Mater., 2025, 37, 2412908; Nano Energy, 2024, 120, 109094; Nano Energy, 2025, 133, 110519).** The existing literature primarily focuses on exploring and validating the functionalities of commercially available or naturally existing polysaccharide materials (such as sodium alginate (SA), carboxymethyl cellulose (CMC), and bacterial cellulose (BC)) within battery systems (e.g., SA for adsorbing polyiodides, CMC for regulating the zinc anode interface). These can be categorized as experimental applications of existing materials. In contrast, the central contribution of this work lies in molecular-level structural engineering. By subjecting cellulose nanofibers to a controlled periodate-borohydride treatment, we selectively cleave C2-C3 bonds within the anhydroglucose units, yielding an oxidized nanofiber with deliberately reconstructed intermolecular interactions, surface potential, and dispersion behavior. This represents a chemistry-driven redesign of the cellulose framework, rather than functional deployment of a native polysaccharide.

2. **Elucidating the cascade effects from molecular structure, interchain interactions, to macroscopic assembly morphology (Our work) *vs.* Focusing on the influence of molecular functional groups (Adv. Mater., 2025, 37, 2412908; Nano Energy, 2025, 133, 110519).** In terms of the mechanism of action, unlike the cited literature (Nano Energy 2025, 133, 110519) which primarily focuses on the chemical adsorption of polyiodides by oxygen-containing functional groups, our study directly addresses the mechanistic gaps explicitly highlighted in the *Perspective and Outlook* section of the review article (Advanced Materials 2025, 37, 2412908) cited by the reviewer, which notes that a deep understanding of structure-performance relationships in cellulose-based energy materials remains lacking. Through a combination of spectroscopic, structural, mechanical, electrochemical, and theoretical analyses, we demonstrate how tailored regulation of ONF’s functional groups, molecular conformation, interchain hydrogen bonding, and electrode architecture collectively governs electrochemical behavior. Importantly, the function of ONF extends well beyond simple adsorption. ONF provides (i) spatial confinement of polyiodides through its optimized fibrous conformation, (ii) reinforced and thermally stable hydrogen-bonding networks that promote ion transport, and (iii) the ability

to form a thin yet dense and mechanically robust coating on active particles, which facilitates charge transfer and preserves electrode integrity during prolonged cycling. Together, these features enable a synergistic "confinement-anchoring-conversion" mechanism, effectively suppressing polyiodide dissolution while accelerating redox kinetics.

3. **Exceptional and comprehensive electrochemical performance (Our work) *vs.* Moderate electrochemical performance (Nano Energy, 2025, 133, 110519).** Attributable to the aforementioned unique cascade reinforcement mechanism based on hydroxyl chemistry, aqueous zinc-iodine batteries employing the ONF binder exhibit significantly improved electrochemical performance. This performance not only substantially surpasses that reported in the references cited (Table R2) by the reviewer, but also exceeds most current studies on binder, iodine host, separator, electrolyte, and zinc-anode modifications for zinc-iodine batteries (Supplementary Table 4).

4. **Applicability to multiple electrochemical systems (Our work) *vs.* Demonstration limited to a single electrochemical system (Nano Energy, 2025, 133, 110519).** The ONF binder we developed exhibits excellent interfacial compatibility and dense, stable coating of active materials, leading to significant performance improvements in systems such as Zn-I_2 and Zn-V_2O_5 batteries. This highlights the great potential of ONF as a universal binder for aqueous zinc batteries. Unfortunately, the cited reference only investigates the binder in the zinc-iodine system, failing to demonstrate its broader applicability.

These major differences between our work and previous works are further listed in the following Table R1 for a clear and detailed comparison.

Table R1. Comprehensive comparison between this work and the literature cited by the reviewer.

Product (study object)	Design concept	Origin of materials	Mechanism
ONF binder (Our work)	Design and synthesize cellulose derivatives based on molecular structure to develop binders with integrated performance surpassing that of existing materials	Obtained through molecular structural modification of cellulose (cleavage of the C2-C3 bond)	Simultaneously achieve strong adsorption sites, confined molecular conformation, dense hydrogen-bonding network, and a stable, rapid mass-transport electrode structure, leveraging the synergistic mechanism of chemical adsorption, physical confinement, and catalytic conversion to suppress active-material dissolution
Sodium alginate (SA) binder (Nano energy 2025, 133, 110519)	Screen and validate the performance of a series of existing natural/commercial linear polysaccharides as binders	SA, commercially available	The oxygen-containing functional groups on the SA chains chemically adsorb polyiodide ions and suppress the shuttle effect

Carboxymethyl cellulose (CMC) electrolyte additive (Nano Energy 2024, 120, 109094)	Discover and utilize the functionality of CMC as an electrolyte additive	CMC, commercially available	CMC forms a water-lean double-layer on the zinc anode surface, participates in SEI construction, suppresses side reactions, and induces uniform zinc deposition
Bacterial cellulose (BC) derived binder (Advanced Materials 2025, 37, 2412908)	Employing BC as a cathode binder to provide a three-dimensional ion transport network within the electrode.	BC, obtained through microbial fermentation	Owing to its flexibility, hydroxyl groups, biodegradability, and three dimensional network structure, BC can be used as a binder; however, it is recommended to functionalize BC or combine it with other materials to construct multifunctional integrated electrodes

Note: Advanced Materials 2025, 37, 2412908 is a review article.

In summary, while previous studies have opened important avenues for employing polysaccharide materials in zinc-based batteries, the present work introduces a chemically redesigned cellulose material, provides deeper mechanistic insight, and achieves substantially improved electrochemical performance beyond conventional adsorption-based approaches. We believe these advances constitute a meaningful and original contribution to the field.

Moreover, to give a clearer picture of our innovative work according to the comments of Referee #4, **we summarize the novelty of our work as follows:**

1. **First Molecular Backbone Re-Engineering Strategy for Enhanced Binding Functionality:** Conventional binders including PVDF and functional polymers retain rigid backbone conformations that limit the accessibility and reactivity of their functional groups, restricting interfacial interactions with active species. In contrast, by unlocking the rigid anhydroglucose unit ring through targeted molecular cleavage, we enhance dipole polarity, chain flexibility, and intermolecular hydrogen-bond density. This molecular reconfiguration significantly increases binding-site availability, enabling strong, selective interactions with soluble redox species and improving electrode cohesion.
2. **First Demonstration of a High- and Uniform-Coverage Electrode**: Existing binders form discontinuous coatings with interfacial voids and incomplete encapsulation of active particles, due to poor interfacial compatibility and low functional-group density, which disrupt the conduction network and permit leakage of soluble species. By comparison, open-ring cellulose self-assembles into a dense, flexible nanofibrous network with excellent interfacial compatibility, delivering uniform particle coverage, spatially homogeneous charge transfer, and robust mechanical integrity during long-term cycling, effectively eliminating the leakage channels and transport bottlenecks inherent to existing binders.

3. **Record-Setting Rate Capability and Cycling Stability in Aqueous Cathodes**: Existing aqueous iodine cathodes, even when combined with advanced hosts, electrolyte additives, ion-selective separators, or functional binders, rarely achieve both ultrahigh rate capability and long-term stability. Leveraging the above chemical and structural advantages, our binder enables shuttle-free iodine cathodes with the highest reported capacity of 150.9 mAh g^{-1} at 20 A g^{-1} and the lowest capacity decay of 0.00048% per cycle over 10000 cycles at 10 A g^{-1}, surpassing the performance of any reported system based on these individual or combined strategies.
4. **First Binder Strategy Linking Chemistry, Architecture, and Redox Behavior Across Different Cathodes:** Unlike prior binder designs optimized for a single electrode system, our strategy links binder chemistry, electrode architecture, and redox behavior in a unified design framework. It further enables, for the first time, scalable fabrication of thick, high-mass-loading electrodes through a simple, water-mediated layer-by-layer stacking process, achieving robust mechanical cohesion and integrated ion/electron conduction pathways. Beyond iodine cathodes, the binder maintains interfacial stability and suppresses active-species migration in dissolution-prone systems such as V_2O_5.

In addition, we appreciate Referee #4's constructive suggestions and comments regarding the current manuscript. At the same time, we are aware that the academic quality of our manuscript should be further improved to dispel these doubts, and that is what we've been working on in the past few months. While addressing all the comments, we have further improved this work given more comprehensive experiments and simulations (Fig. R3). **The highlights of our revisions added in the Revised Manuscript are summarized below:**

I. Systematically correlate the relationships between ring-opening degree, fiber yield, and electrochemical performance to identify the optimal synthesis conditions

We introduced the extracyclic hydroxyl content as a quantitative indicator to characterize the AGU ring-opening degree. As sodium periodate ($NaIO_4$) selectively cleaves the C2-C3 bond of the anhydroglucose unit to generate aldehyde groups, followed by sodium borohydride ($NaBH_4$) reduction to form extracyclic hydroxyl groups, the resulting extracyclic hydroxyl content directly reflects the extent of ring opening. By tuning the molar ratio of $NaIO_4$ to AGU, we prepared a series of cellulose samples with different degrees of ring opening. The extracyclic hydroxyl content, product yields, and corresponding electrochemical performance when used as binders for iodine cathodes were systematically evaluated.

II. Analyze the hydrogen-bond energy distribution within cellulose clusters and the spatial conformation of cellulose through simulation calculations

We conducted molecular dynamics simulation studies to directly assess the number, distribution, and thermal stability of hydrogen bonds within different cellulose clusters. The results indicate that, compared to CNF, ONF possesses a stronger, denser, and more thermally stable intermolecular hydrogen-bonding network. Additionally, conformational analysis of CNF and ONF molecular chains with identical degrees of polymerization reveals that ONF adopts a more compact and conformationally ordered helical structure, with its hydroxyl groups preferentially oriented toward the outer surface. This structural reorganization enhances the spatial cooperativity among hydroxyl groups and facilitates the formation of a dense and continuous hydrogen-bonding network.

III. Deepened characterization of physical properties of membrane materials, iodine hosts, and cathodes

We have eliminated interference from potential residual elements introduced during cellulose processing and conducted specific surface area analysis on the iodine carriers. Furthermore, the superior wet-state mechanical properties and anti-swelling performance of cathodes prepared with ONF have been supplemented. The feasibility of one-step electrode fabrication has also been demonstrated.

IV. Systematic demonstration of iodine interaction

We have supplemented in situ Raman tests under the influence of CNF, as well as calculations of the adsorption energy of iodine species on CNF and the Gibbs free energy for iodine species conversion in the presence of CNF. Although the interaction between CNF and iodine species is less pronounced compared to ONF, the inclusion of these results provides a more systematic comparison among different binders.

V. Outstanding electrochemical performance of ONF binder applied in different systems

We have supplemented the long-cycle data of PVDF cathodes with active material loading comparable to that of the cellulose-based systems, the cycling performance of all iodine cathodes at low current densities, the self-discharge behavior of both Zn-I_2 and Zn-V_2O_5 systems at 24/48/96 h resting, and the testing results of ampere-hour-level pouch cells. The cathodes prepared with the ONF binder consistently exhibit the most outstanding electrochemical performance across all tested conditions/environments.

VI. Validation of electrode structure and binder stability

We have enhanced the comprehensive analysis of electrode structural stability before and after cycling, including supplementing micro-morphological images of cathodes at different magnifications and XRD/FTIR characterization of binder fiber degradation. The results demonstrate that the ONF binder exhibits excellent stability, and the dense coating structure it forms on the cathode remains intact throughout electrochemical operation, ensuring stable performance of the electrochemical device.

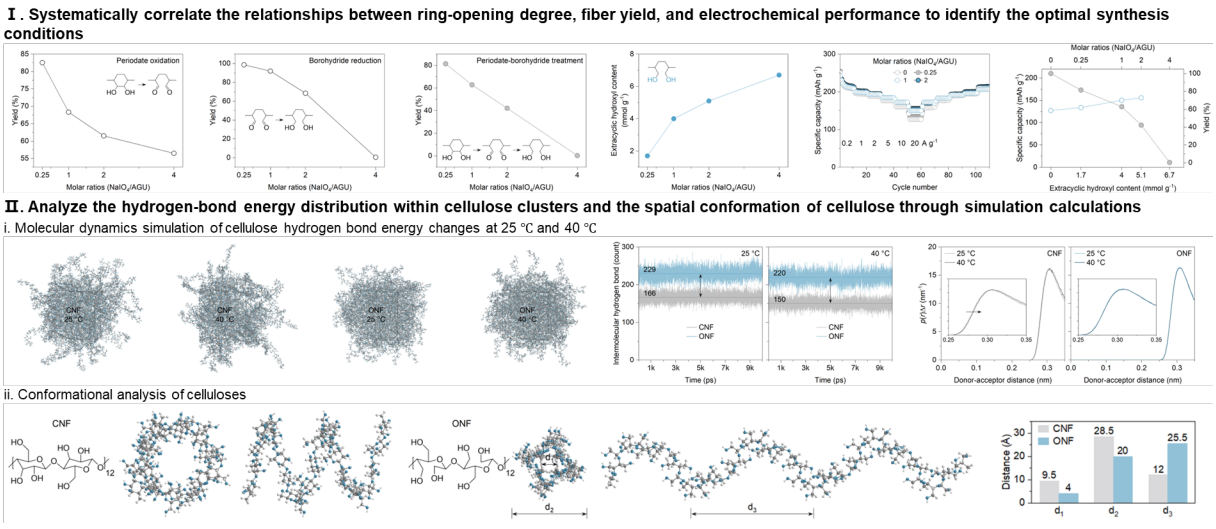

Ⅲ. Deepened characterization of physical properties of membrane materials, iodine hosts, and cathodes

i. Binder residual iodine source detection

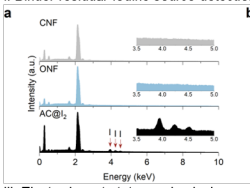

ii. Iodine host specific surface area analysis

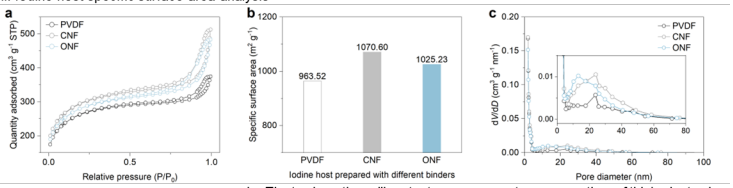

iii. Electrode wet-state mechanical properties

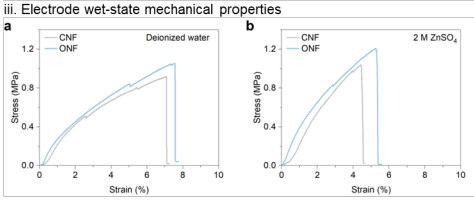

iv. Electrode anti-swelling test

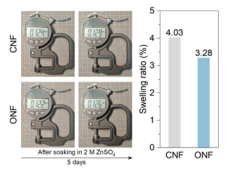

v. one-step preparation of thick electrodes

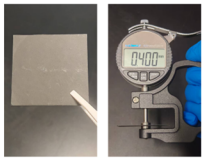

Ⅳ. Systematic demonstration of iodine interaction

i. In situ Raman spectroscopy

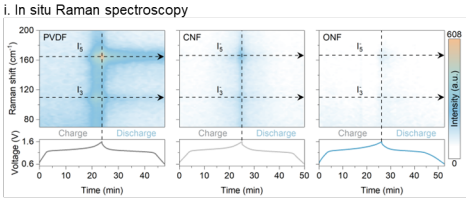

ii. Binding energy

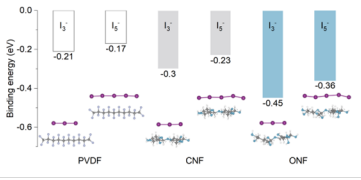

iii. Gibbs free energy for iodine species conversion

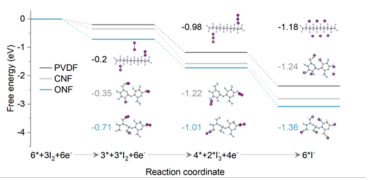

Ⅴ. Outstanding electrochemical performance of ONF binder applied in different systems

i. High-rate long-term cycling performance

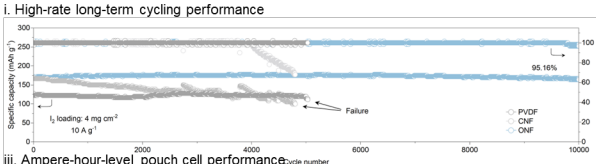

ii. Low-current cycling performance

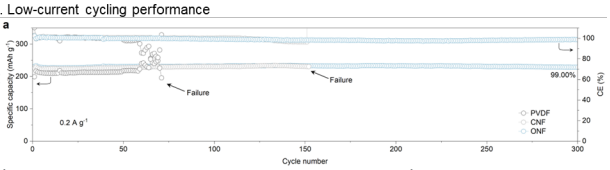

iii. Ampere-hour-level pouch cell performance

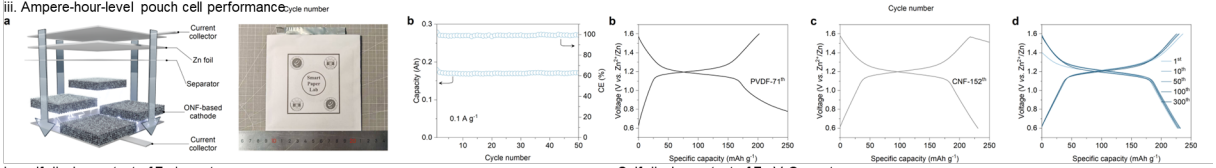

iv. self-discharge test of Zn-I_2 system

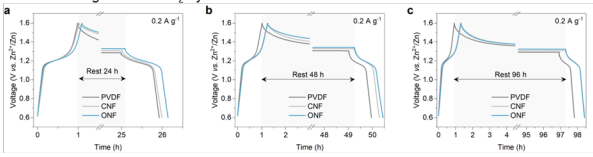

v. Self-discharge test of Zn-V_2O_5 system

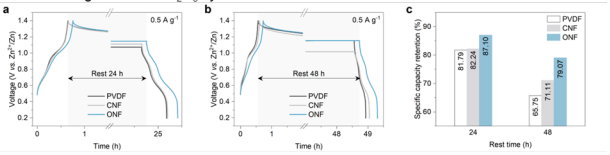

Ⅵ. Validation of electrode structure and binder stability

i. Surface morphology of iodine cathodes

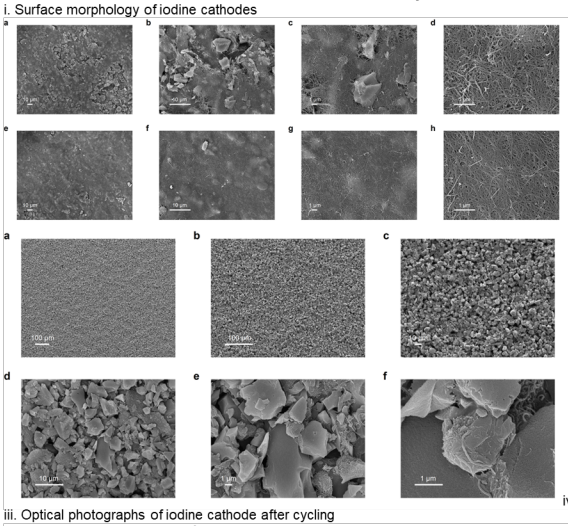

ii. Structural stability characterization of cellulose before/after cycling

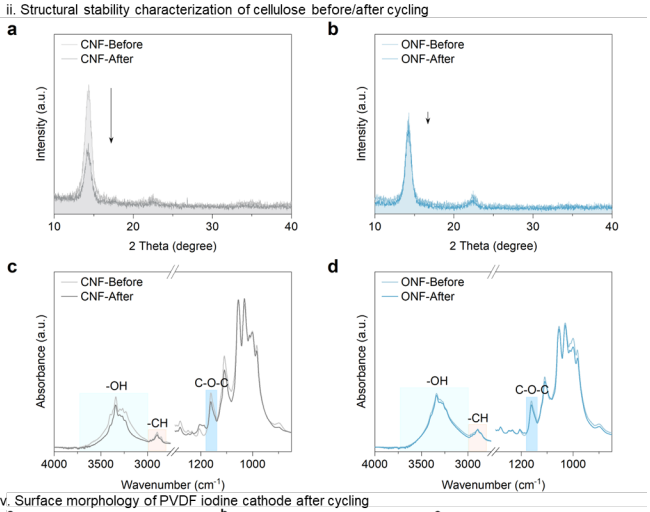

iii. Optical photographs of iodine cathode after cycling

iv. Surface morphology of PVDF iodine cathode after cycling

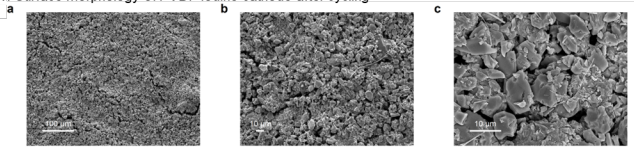

Fig. R3. A summary of our experimental and simulation efforts over the past few weeks, aimed at providing more robust evidence for the superiority and universality of the developed binder, and offering deeper insights into its structure-property-performance relationship.

Table R2. Comparison of zinc-iodine battery performance between this work and the literature cited by the reviewer.

Samples	Iodine loading	Rate performance	Cycling stability
ONF binder	4 mg cm^{-2}	212.7 mA h g^{-1} (0.2 A g^{-1}) 199.1 mA h g^{-1} (1 A g^{-1}) 194.2 mA h g^{-1} (2 A g^{-1}) 185.5 mA h g^{-1} (5 A g^{-1}) 173.1 mA h g^{-1} (10 A g^{-1}) 150.9 mA h g^{-1} (20 A g^{-1})	163.9 mAh g^{-1} at 10 A g^{-1} after 10000 cycles (95.16% capacity retention)
SA binder	1.2 mg cm^{-2}	155.9 mA h g^{-1} (0.1 A g^{-1}) 142.4 mA h g^{-1} (0.2 A g^{-1}) 136.1 mA h g^{-1} (0.4 A g^{-1}) 125.8 mA h g^{-1} (1 A g^{-1}) 114.7 mA h g^{-1} (2 A g^{-1}) 102.5 mA h g^{-1} (4 A g^{-1})	86.3 mAh g^{-1} at 5 A g^{-1} after 40000 cycles (80% capacity retention)

Note: Among the literature cited by the reviewer, only one pertains to zinc-iodine battery research.

Supplementary Table 4. Comparative of electrochemical performance in aqueous Zn-I_2 battery.

Samples		Iodine loading	Rate performance	Cycling stability
Binder	Ref. 1	1-2 mg cm^{-2}	179.8 mAh g^{-1} (0.2697 mAh cm^{-2}) at 0.2 A g^{-1} 123.2 mAh g^{-1} (0.1848 mAh cm^{-2}) at 2 A g^{-1}	142.5 mAh g^{-1} (0.2138 mAh cm^{-2}) at 0.2 A g^{-1} after 1500 cycles
	Ref. 2	2.69 mg cm^{-2}	213.8 mAh g^{-1} (0.5751 mAh cm^{-2}) at 0.2 A g^{-1} 83.0 mAh g^{-1} (0.2233 mAh cm^{-2}) at 5 A g^{-1}	129.4 mAh g^{-1} (0.3750 mAh cm^{-2}) at 2 A g^{-1} after 2700 cycles
	Ref. 3	4.7 mg cm^{-2}	207.2 mAh g^{-1} (0.9738 mAh cm^{-2}) at 0.2 A g^{-1} 156.6 mAh g^{-1} (0.7360 mAh cm^{-2}) at 3 A g^{-1}	151.1 mAh g^{-1} (0.7102 mAh cm^{-2}) at 3 A g^{-1} after 9000 cycles

	Ref. 4	2.3 mg cm^{-2}	219.0 mAh g^{-1} (0.5037 mAh cm^{-2}) at 0.1 A g^{-1} 141.5 mAh g^{-1} (0.3254 mAh cm^{-2}) at 2 A g^{-1}	157.7 mAh g^{-1} (0.3627 mAh cm^{-2}) at 2 A g^{-1} after 48000 cycles
	Ref.5	-	185.5 mAh g^{-1} at 0.1 A g^{-1} 121.8 mAh g^{-1} at 2 A g^{-1}	88.2 mAh g^{-1} at 4 A g^{-1} after 15000 cycles
Iodine host	Ref. 6	3 mg cm^{-2}	176.5 mAh g^{-1} (0.5295 mAh cm^{-2}) at 0.2 A g^{-1} 66.3 mAh g^{-1} (0.1989 mAh cm^{-2}) at 10 A g^{-1}	88.2 mAh g^{-1} (0.0246 mAh cm^{-2}) at 10 A g^{-1} after 10000 cycles
	Ref. 7	1.7 mg cm^{-2}	164.8 mAh g^{-1} (0.2802 mAh cm^{-2}) at 0.1 A g^{-1} 72.3 mAh g^{-1} (0.1229 mAh cm^{-2}) at 1 A g^{-1}	116.6 mAh g^{-1} (0.1982 mAh cm^{-2}) at 0.8 A g^{-1} after 1000 cycles
	Ref. 8	0.8-1.2 mg cm^{-2}	195.1 mAh g^{-1} (0.1951 mAh cm^{-2}) at 0.1 A g^{-1} 93.5 mAh g^{-1} (0.0935 mAh cm^{-2}) at 10 A g^{-1}	113.1 mAh g^{-1} (0.1131 mAh cm^{-2}) at 1 A g^{-1} after 1000 cycles
	Ref. 9	2-2.5 mg cm^{-2}	255.4 mAh g^{-1} (0.5746 mAh cm^{-2}) at 0.1 A g^{-1} 152.3 mAh g^{-1} (0.3427 mAh cm^{-2}) at 3 A g^{-1}	124.0 mAh g^{-1} (0.2790 mAh cm^{-2}) at 3 A g^{-1} after 5900 cycles
	Ref. 10	2 mg cm^{-2}	212 mAh g^{-1} (0.4240 mAh cm^{-2}) at 0.2 A g^{-1} 92 mAh g^{-1} (0.184 mAh cm^{-2}) at 8 A g^{-1}	111.9 mAh g^{-1} (0.2238 mAh cm^{-2}) at 5 A g^{-1} after 5000 cycles
	Ref. 11	0.8-1.2 mg cm^{-2}	241.5 mAh g^{-1} (0.2415 mAh cm^{-2}) at 0.2 A g^{-1} 161.8 mAh g^{-1} (0.1618 mAh cm^{-2}) at 2 A g^{-1}	92.6 mAh g^{-1} (0.0926 mAh cm^{-2}) at 5 A g^{-1} after 20000 cycles
	Ref. 12	3.3 mg cm^{-2}	162.4 mAh g^{-1} (0.5359 mAh cm^{-2}) at 0.2 A g^{-1} 100.8 mAh g^{-1} (0.3326 mAh cm^{-2}) at 2 A g^{-1}	83.6 mAh g^{-1} (0.0119 mAh cm^{-2}) at 2 A g^{-1} after 1000 cycles

Separator	Ref. 13	2 mg cm^{-2}	236.7 mAh g^{-1} (0.4734 mAh cm^{-2}) at 0.2 A g^{-1} 144.9 mAh g^{-1} (0.2898 mAh cm^{-2}) at 5 A g^{-1}	158.3 mAh g^{-1} (0.3166 mAh cm^{-2}) at 2 A g^{-1} after 20000 cycles
	Ref. 14	1.5 mg cm^{-2}	208 mAh g^{-1} (0.3120 mAh cm^{-2}) at 0.1 A g^{-1} 114 mAh g^{-1} (0.1710 mAh cm^{-2}) at 2 A g^{-1}	146.1 mAh g^{-1} (0.2374 mAh cm^{-2}) at 0.2 A g^{-1} after 3600 cycles
Electrolyte	Ref. 15	-	176.8 mAh g^{-1} (0.1 A g^{-1}) 151.6 m mAh g^{-1} (2 A g^{-1})	166.7 mAh g^{-1} at 2 A g^{-1} after 15000 cycles
	Ref. 16	1 mg cm^{-2}	212.3 mAh g^{-1} (0.2123 mAh cm^{-2}) at 0.2 A g^{-1} 192.3 mAh g^{-1} (0.1923 mAh cm^{-2}) at 4 A g^{-1}	185.2 mAh g^{-1} (0.1852 mAh cm^{-2}) at 1 A g^{-1} after 2000 cycles
	Ref. 17	5 mg cm^{-2}	134.4 mAh g^{-1} (0.6720 mAh cm^{-2}) at 0.5 A g^{-1} 79.2 mAh g^{-1} (0.3960 mAh cm^{-2}) at 10 A g^{-1}	99.6 mAh g^{-1} (0.4980 mAh cm^{-2}) at 2 A g^{-1} after 50000 cycles
	Ref. 18	0.8-1.0 mg cm^{-2}	138.4 mAh g^{-1} (0.1246 mAh cm^{-2}) at 0.5 A g^{-1} 81.6 mAh g^{-1} (0.0734 mAh cm^{-2}) at 10 A g^{-1}	98.1 mAh g^{-1} (0.0882 mAh cm^{-2}) at 1 A g^{-1} after 8000 cycles
Zinc anode	Ref. 19	5.4 mg cm^{-2}	168.8 mAh g^{-1} (0.9115 mAh cm^{-2}) at 0.1 A g^{-1} 118.8 mAh g^{-1} (0.6415 mAh cm^{-2}) at 6 A g^{-1}	105.8 mAh g^{-1} (0.5713 mAh cm^{-2}) at 2 A g^{-1} after 65000 cycles
	Ref. 20	6 mg cm^{-2}	214.0 mAh g^{-1} (1.2840 mAh cm^{-2}) at 0.1 A g^{-1} 130.6 mAh g^{-1} (0.7836 mAh cm^{-2}) at 2 A g^{-1}	124.0 mAh g^{-1} (0.7440 mAh cm^{-2}) at 1 A g^{-1} after 2400 cycles
	Ref. 21	1.3 mg cm^{-2}	169.3 mAh g^{-1} (0.2201 mAh cm^{-2}) at 0.2 A g^{-1} 98.8 mAh g^{-1} (0.1284 mAh cm^{-2}) at 5 A g^{-1}	97.0 mAh g^{-1} (0.1261 mAh cm^{-2}) at 2 A g^{-1} after 20000 cycles

	Ref. 22	1-1.5 mg cm^{-2}	174.0 mAh g^{-1} (0.2175 mAh cm^{-2}) at 0.2 A g^{-1} 125.0 mAh g^{-1} (0.1562 mAh cm^{-2}) at 10 A g^{-1}	124.2 mAh g^{-1} (0.1552 mAh cm^{-2}) at 5 A g^{-1} after 60000 cycles
	Ref. 23	-	195.9 mAh g^{-1} (0.1 A g^{-1}) 124.5 mAh g^{-1} (5 A g^{-1})	141.8 mAh g^{-1} at 2 A g^{-1} after 5600 cycles
This work	ONF binder	4 mg cm^{-2}	212.7 mAh g^{-1} (0.8508 mAh cm^{-2}, 2.5611 mWh cm^{-3}) at 0.2 A g^{-1} 173.1 mAh g^{-1} (0.6924 mAh cm^{-2}, 1.9888 mWh cm^{-3}) at 10 A g^{-1} 150.9 mAh g^{-1} (0.6036 mAh cm^{-2}, 1.6121 mWh cm^{-3}) at 20 A g^{-1}	163.9 mAh g^{-1} (0.6556 mAh cm^{-2}, 1.5528 mWh cm^{-3}) at 10A g^{-1} after 10000 cycles

Note: Areal capacity (mAh cm^{-2}) = Specific capacity (mAh g^{-1}) × Iodine loading (g cm^{-2}), Volumetric energy density (mWh cm^{-3}) = (Areal capacity (mAh cm^{-2}) × Average voltage (V)) / Cathode thickness (cm).

We would like to thank the reviewers again for your constructive comments and criticisms, which have guided us to strengthen our manuscript substantially in the past few months. With all these revisions made, we sincerely hope the reviewers find our revised manuscript meet the high standard of Nature Communications.

Version 2

Point-by-Point Response to Referees' Comments
(*Blue italic: Reviewer's remarks*; Black type: Our response)

Reviewer #1:
"Authors have well revised the manuscript that becomes acceptable now."
Reply to the Reviewer:
We sincerely thank you for your positive assessment and for your previous constructive comments that helped improve the manuscript.

Reviewer #3:
"The author has adequately addressed the reviewers' concerns. Recommend to publish this paper as current form."
Reply to the Reviewer:
We appreciate your acknowledgement that our revisions have adequately addressed all concerns, and thank you for your recommendation to publish.

Reviewer #4:
"Happy with the revision, the paper can be accepted as it is."
Reply to the Reviewer:
Thank you for your encouraging feedback and for confirming that the paper can be accepted as it is.